AD NUMBER

AD392113

CLASSIFICATION CHANGES

TO: unclassified

FROM: confidential

LIMITATION CHANGES

TO:

Approved for public release, distribution unlimited

FROM:

Distribution authorized to U.S. Gov't. agencies only; Specific Authority; May 1968. Other requests shall be referred to Director, Naval Research Lab, Washington, DC 20390.

AUTHORITY

May 1980 per DoDD 5200.10 document marking; AFADTC ltr dtd 28 Jan 1981

CONFIDENTIAL

NRL Report 6743
AFATL-TR-68-59

Final Report

Hypervelocity Impact of Rods on Finite Targets

[Unclassified Title]

M. ROSENBLATT, K. N. KREYENHAGEN, AND R. L. BJORK

Shock Hydrodynamics, Inc.
(A Subsidiary of Whittaker Corporation)
Sherman Oaks, California

Sponsored by
Air Force Armament Laboratory
Eglin AFB, Florida

May 1968

NAVAL RESEARCH LABORATORY
Washington, D.C.

CONFIDENTIAL

SECURITY

This document contains information affecting the national defense of the United States within the meaning of the Espionage Laws, Title 18, U.S.C., Sections 793 and 794. The transmission or revelation of its contents in any manner to an unauthorized person is prohibited by law.

In addition to security requirements which must be met, this document is subject to special export controls and each transmittal to foreign governments or foreign nationals may be made only with prior approval of the Air Force Armament Laboratory (AFATL), Eglin AFB, Florida 32542.

This report is unclassified except for those sections and figures relating to experimental results. They are Sections 2.3.2, 2.4, and 3.4 and Figures 2-9 through 2-14 and Figure 3-8 which are all Confidential.

CONTENTS

CONTENTS (Continued)

ABSTRACT
[Unclassified]

An analytical study is described of the phenomena leading to rod loss in the perforation of finite targets by hypervelocity impact of end-oriented rods. The investigation is based upon two-dimensional hydrodynamic PIC (particle-in-cell) code solutions of sixteen impact cases. These impact cases include solid and hollow rods, normal and oblique incidence, and aluminum and iron rods impacting aluminum plates of varying thicknesses at velocities of 4.6 and 6.1 km/sec (15,000 and 20,000 ft/sec). For oblique incidence, the planar approximation is used to reduce the problems to two space dimensions.

Results of the initial portion of the investigation have been previously described in NRL Report 6310 (April 1965). The present report deals primarily with impacts on relatively thick targets, and with oblique incidence and hollow rod impacts.

From the numerical solutions, detailed plots of the shock systems and flow fields occurring during perforation are obtained. From the flow fields for impacts where the ratio of target thickness to rod diameter is two or greater, it is found that the processes causing rod loss can be divided into three phases; (1) the initial transient phase during which the intense shock system caused by impact is attenuated by rarefactions from free surfaces, (2) the quasi-steady state phase, during which the flow field remains essentially unchanged relative to a stagnation point near the tip of the advancing rod shaft, and (3) the breakthrough phase, during which the rod moves through the remaining shattered target material. Most of the rod loss occurs during the steady state phase.

Quantitative information from the flow fields is used to derive relationships for predicting rod loss as a function of velocity, target thickness, projectile and target materials, and impact obliquity. Comparison of these relationships with experimental data obtained by NRL provides verification of their validity.

PROBLEM STATUS

This is a final report.

AUTHORIZATION

NRL Problem F04-16
Project MIPR PG-3-15
Office of Naval Research Contract NONR 4221(00)(X)
Air Force Project 9850

Report prepared by Shock Hydrodynamics, Inc., for the Naval Research Laboratory, the project being sponsored by the Air Force Armament Laboratory, AFATL, Eglin AFB, Florida.

Final composition, printing, and distribution of this report have been carried out by the Naval Research Laboratory.

Manuscript submitted May 6, 1968.

NOTATION

A, B	constants in Eq. (2-21) and Table 2-1
C	local sound speed
D	rod diameter (where projectile is a rod) or plate thickness (where projectile is a plate)
e	specific internal energy
e_T	specific internal energy in target material
e_P	specific internal energy in projectile material
ID	inside diameter of hollow rod
ΔL	rod length lost during perforation
OD	outside diameter of hollow rod
P	pressure
S	shock speed in undisturbed material corresponding to impact velocity V .
t	time
t_f	time required for Y_P to equal T
T	target thickness
u	particle velocity
V	impact velocity
V_∞	stagnation point velocity
Y_P	penetration (or open hole) depth
Y_S	depth of stagnation point
θ	angle of impact incidence (measured between impact velocity and surface normal)
ρ	density
ρ_T	target density
ρ_P	projectile density

τ	time characteristic of initial transient phase (in axisymmetric impact)
τ_o	time at which initial one-dimensional nature of shock system is completely destroyed by lateral rarefactions
τ_{PL}	time characteristic of initial transient phase in planar impact
τ_{3-D}	time characteristic of initial transient phase in oblique impact of rod

FINAL REPORT

HYPERVELOCITY IMPACT OF RODS ON FINITE TARGETS

1. INTRODUCTION

This is the final report of an analytical research investigation of impacts of end-oriented rods into finite targets. The study, based upon two-dimensional hydrodynamic PIC (Particle-in-Cell) code solutions of selected impact cases, was aimed at providing (a) increased understanding of the physical processes operating in such impacts, and (b) techniques for predicting impact effects for different materials under various conditions of impacting velocities and obliquities. The research was started in 1964. A related experimental investigation has been conducted during the same period by the Naval Research Laboratory.

In the initial phase of the study, emphasis was given to impacts against relatively thin targets. A previously-issued report[1] describes results of the initial phase, and only those data which are necessary to provide continuity will be repeated in this final report.

In the final phase, which is described in detail in this report, thicker targets were considered, along with hollow rods and also oblique impacts.

1.1 APPROACH

The approach taken was to use hydrodynamic solutions to obtain detailed data regarding mass positions, pressures, and particle velocities as functions of time. These data were analyzed and compared, and from them, relationships for rod loss as a function of impact velocity and projectile target materials were developed.

1.2 IMPACT CASES CONSIDERED

In the overall program, sixteen specific impact cases were examined in detail. These are summarized in Figures 1-1 and 1-2. Eight of these were considered in the initial phase of the study, and are reported upon in reference 1.

Solution plots for some of the problems were prepared in the form of movies which have been delivered to the Naval Research Laboratory.

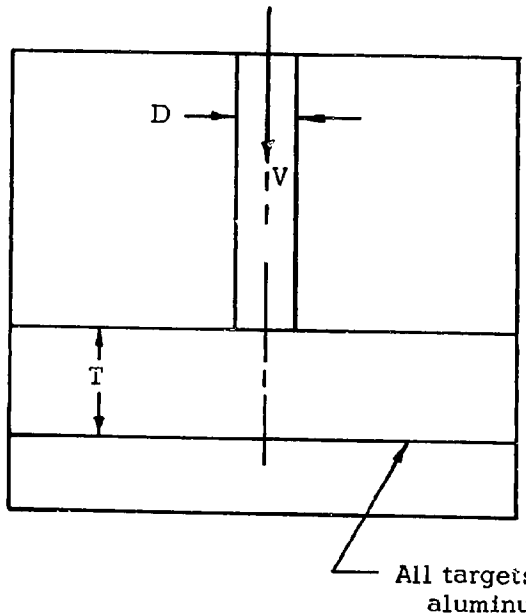

Rod Material	Impact Velocity (V) (km/sec)	Target Thickness/Rod Diameter (T/D					
		$\frac{1}{4}$	$\frac{1}{2}$	1	2	3	5
Al	4.6	Case 1*	Case 2*	Case 3*	Case 4*	Case 11	Case 12
Al	6.1	Case 7*	Case 8*	-	-	-	-
Fe	4.6	-	Case 5**	Case 6*	-	-	-

* Cases considered in earlier part of investigation (Ref. 1)

** Sequences of plots from this solution were made into movies.

Figure 1-1 Conditions For General Solid Rod Impact Cases

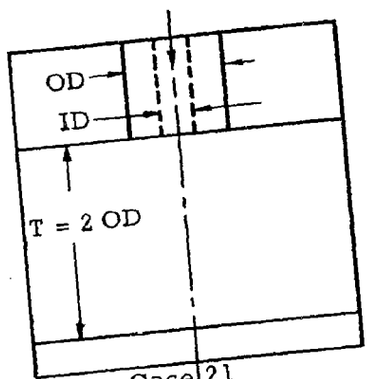

Case 21
Hollow Al Rod vs Al Plate
@ 4.6 km/sec, (ID/OD = $\frac{1}{3}$),
T/OD = 2

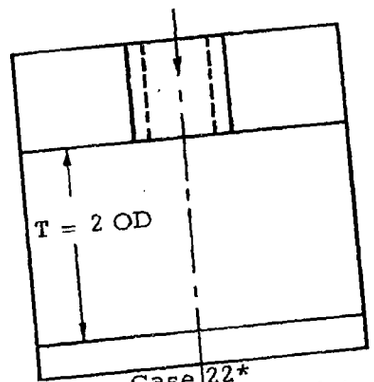

Case 22*
Hollow Al Rod vs Al Plate
@ 4.6 km/sec, (ID/OD = $\frac{2}{3}$),
T/OD = 2

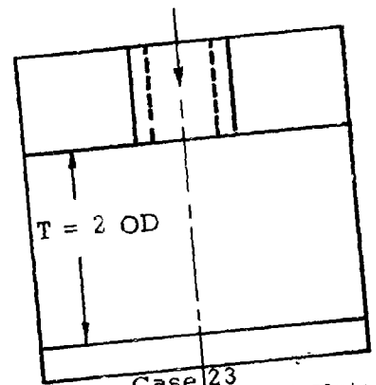

Case 23
Hollow Fe Rod vs Al Plate
@ 4.6 km/sec, (ID/OD = $\frac{2}{3}$),
T/OD = 2

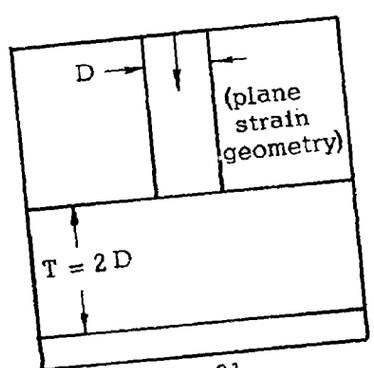

Case 31
Al Rod vs Al Plate At
4.6 km/sec, T/D = 2
$\theta = 0^{\circ}$

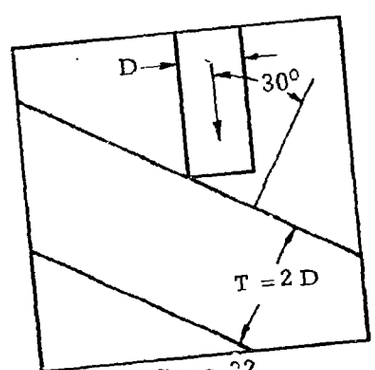

Case 32
Al Rod vs Al Plate At
4.6 km/sec, T/D = 2
$\theta = 30^{\circ}$

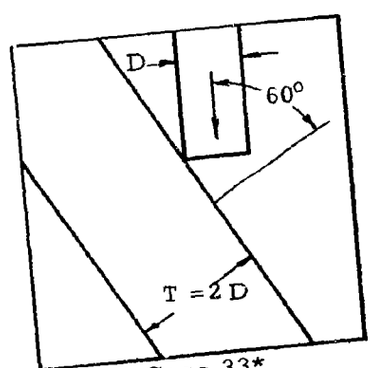

Case 33*
Al Rod vs Al Plate At
4.6 km/sec, T/D = 2
$\theta = 60^{\circ}$

*sequences of plots from these solutions were made into movies.

Figure 1-2 Conditions for Special Rod Impact Cases

1.3 HYDRODYNAMIC MODEL

All of the analyses performed during this study assumed that the projectile and target material properties could be described using a hydrodynamic model. For the velocities which were considered, this assumption is valid for describing the early-stage effects and subsequent steady state phenomena in thicker plate impacts. Later response, including establishment of hole size and the rod loss, clearly involves material strength effects. At the time the study was undertaken, analytical techniques incorporating elastic-plastic properties were not yet available. It was therefore necessary to extract criteria for rod loss from comparison with experiments and by simplified analytical means.

It is clear, however, that an elastic-plastic model is needed to rigorously describe the final states of response. Under other contracts, comprehensive hydrodynamic-elastic-plastic numerical methods have been developed and future studies of rod impact could employ such techniques.[2,3]

2. SOLID ROD IMPACTS

In this section, mechanisms causing projectile rod loss in the normal impact of solid rods are examined and illustrated by means of plots from the numerical solutions. A relationship is then derived for predicting rod loss for various impacts. This relationship is compared with both numerical and experimental results.

2.1 MECHANISMS IN SOLID ROD IMPACTS ON FINITE TARGETS

In high velocity impacts, extreme pressures are created in the projectile and in the impacted region of the target, and these high pressure regimes spread as shocks which propagate outward to engulf adjacent material. The response of the projectile and target materials to this high dynamic pressure field can be divided into three phases, which we will refer to as the initial transient phase, steady state phase, and breakthrough phase.

2.1.1 Initial Transient Phase

Immediately upon impact, shock waves propagate from the interface into both the projectile and the target. Where the projectile face is flat, the region between the diverging shocks is, for a short time, at a constant, high pressure state, in which all motions are one-dimensional (parallel with the impact velocity). This constant one-dimensional state persists until rarefactions from free surfaces arrive to relieve the pressure. Sources for such rarefactions are the front and back surfaces of the target plate, and the sides of the projectile. (For long rod projectiles, the trailing surface of the rod is too remote to be a source of rarefactions during the initial transient phase.)

Where the target is thin relative to the projectile diameter, the back surface of the target will be directly accelerated by the one-dimensional shock, and one-dimensional pressure relief, which we term the frontal rarefaction, will propagate back into the target. The effect of this frontal rarefaction on rod loss is important in impacts on very thin targets, as is discussed in detail in reference 1. As target thickness increases, however, lateral rarefactions emanating from the sides of the rod projectile and from the unshocked adjacent target material become the initial and primary mode of pressure relief in the shocked region. These rarefactions converge towards the axis of the problem, and also overtake the shocks moving into the target and projectile.

Figure 2-1 illustrates these shock systems using spatial plots obtained from numerical solutions in this program. These plots show pressure contours (isobars) at selected intervals. The left boundary is an axis of symmetry, and corresponds to the center line of the rod projectile.

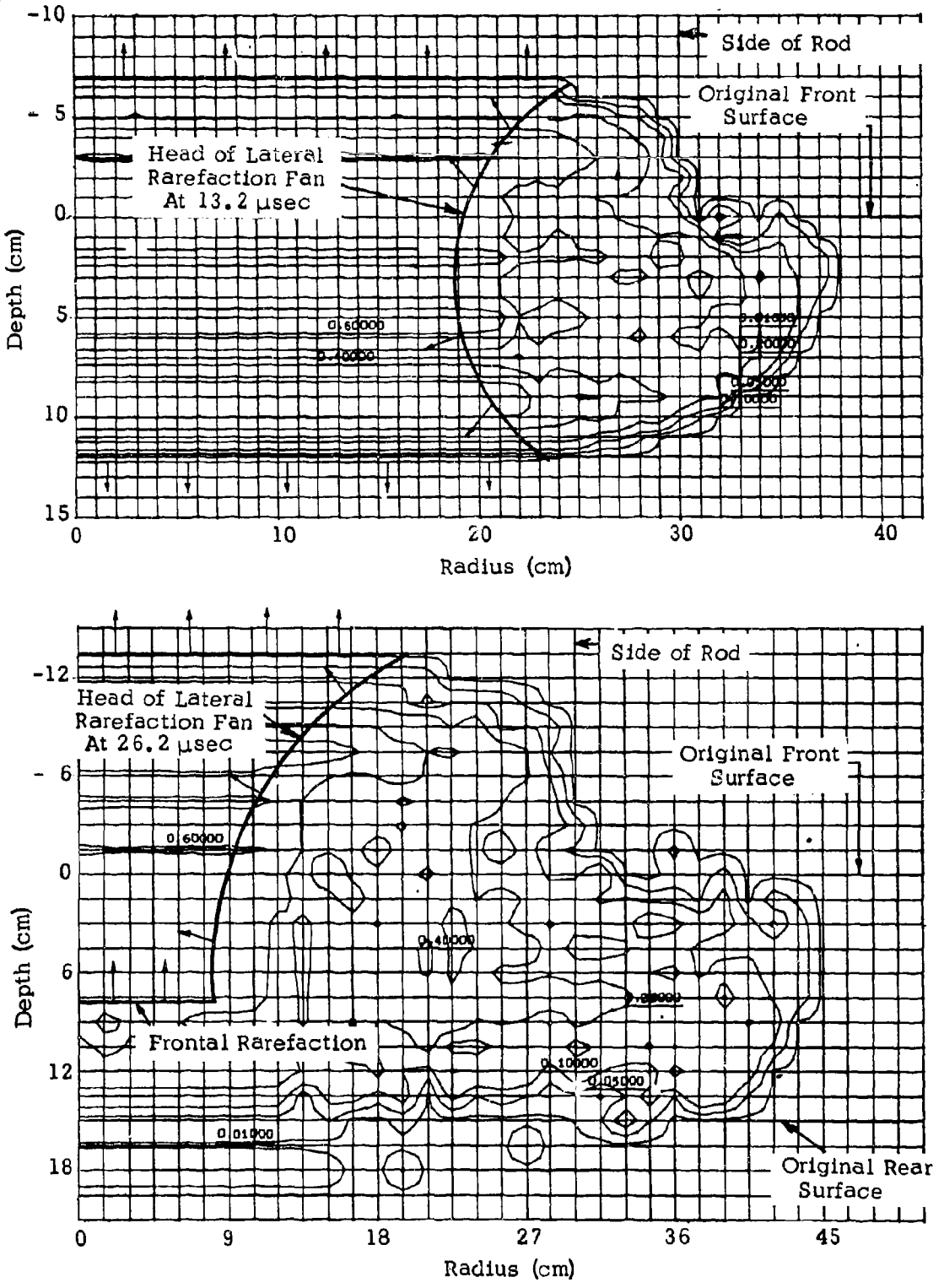

Figure 2-1 Development of Shock and Rarefaction Systems In Thin Plate Impacts

(A more thorough description of the numerical technique and the plotting formats is given in Appendix A.)

In Figure 2-1a, diverging shocks are propagating up into the projectile and also down into the target. The head of a rarefaction fan is propagating in from the side. At the somewhat later time represented in Figure 2-1b, the shock propagating into the projectile remains, but the shock in the target has already reached the rear surface, and a frontal rarefaction is propagating back into the target. The lateral rarefaction is converging into the remaining high pressure region, and will soon thereafter reach the axis. Subsequently, the lateral rarefaction will also overtake the upper shock in the target, thus terminating the initial one-dimensional flow.

In the example shown in Figure 2-1, the one-dimensional shock in the target reached the rear surface prior to being overtaken by the lateral rarefaction. The resulting frontal rarefaction was therefore also one-dimensional. This will always be the case for very thin plate impacts. (i.e., $T/D < \sim 1/2$ for Al-Al impacts at 5-10 km/sec.) For thicker targets, however, lateral rarefactions will overtake the target shock before it reaches the rear surface.

Termination of the one-dimensional high pressure flow by encroachment of the head of the lateral rarefactions constitutes, of course, only the start of the pressure relaxation process which continues in the rarefaction fan until equilibrium is reached. For thin targets, the equilibrium state is at zero pressure, and this is reached directly from the actions of the frontal and lateral rarefactions. In thicker targets, the pressure cannot drop to zero, but rather it drops to a condition established by material flow near the tip of the projectile as it continues to advance into the target.

In summary, an initial transient stage occurs upon impact during which a very intense shock system is established. Free surface rarefactions subsequently attenuate the shock system and return the system to equilibrium, thereby completing the transient phase. In thin targets, this transient stage encompasses virtually all of the significant response phenomena, and it therefore completes the impact process. In thick targets, the transient stage leads into the quasi-steady state phase described in the following section.

2.1.2 Steady State Phase

In thick finite targets (or in semi-infinite targets) the transient phase gives way to a steady state phase during which a deep hole is being formed in the target by the advancing tip of the relatively narrow rod. The rod tip is continually receding (or being worn away) during this process, leading to rod loss. Impacts into thicker targets constituted a major area of study during the portion of the program covered by this report. Hence, the identification and understanding of the steady state processes are emphasized.

Figure 2-2 illustrates some aspects of the steady state phase. (Again, this is a mass position plot from one of the numerical solutions.) The undamaged shaft of the rod continues to travel into the plate at essentially the impact velocity (4.6 km/sec in this case) throughout the penetration process. At the rod-target interface, material is being diverted, first in the radial direction, and then upward, resulting in the formation of an open hole or crater. The rear surface of the target plate has been accelerated by arrival of the initial impact shock, and a bulge is forming on that surface. The velocity imparted to this material, however, is smaller than the impact velocity. The advancing rod is therefore impinging into slower moving target material.

Note in Figure 2-2 that we define the depth of the open hole below the original target surface as the penetration depth Y_P. Evidence that an essentially steady state condition is reached during penetration of a thick, albeit finite target is seen in the plot in Figure 2-3 of Y_P vs time. The values of Y_P in this plot were obtained directly from the numerical solution of the T/D = 3, Al-Al impact at 4.6 km/sec. Following the initial transient stage, it is seen that the rate at which the depth increases, dY_P/dt, remains constant.

In steady state flow, we would also expect to find a stagnation point on the axis just below the bottom of the open hole. We will define the depth of this point below the original surface as Y_S. The velocity of the stagnation point can be evaluated by Bernouli's equation for compressible flow, i.e.

$$\frac{P}{\rho} + \frac{1}{2} u^2 + e = \text{constant on a steady state streamline (particle path)} \qquad (2\text{-}1)$$

where

P = pressure

ρ = density

u = particle velocity

e = specific internal energy

In a frame of reference which moves at the stagnation point velocity, V_∞, consider the motions of as-yet undisturbed particles A and B as they approach the stagnation point.

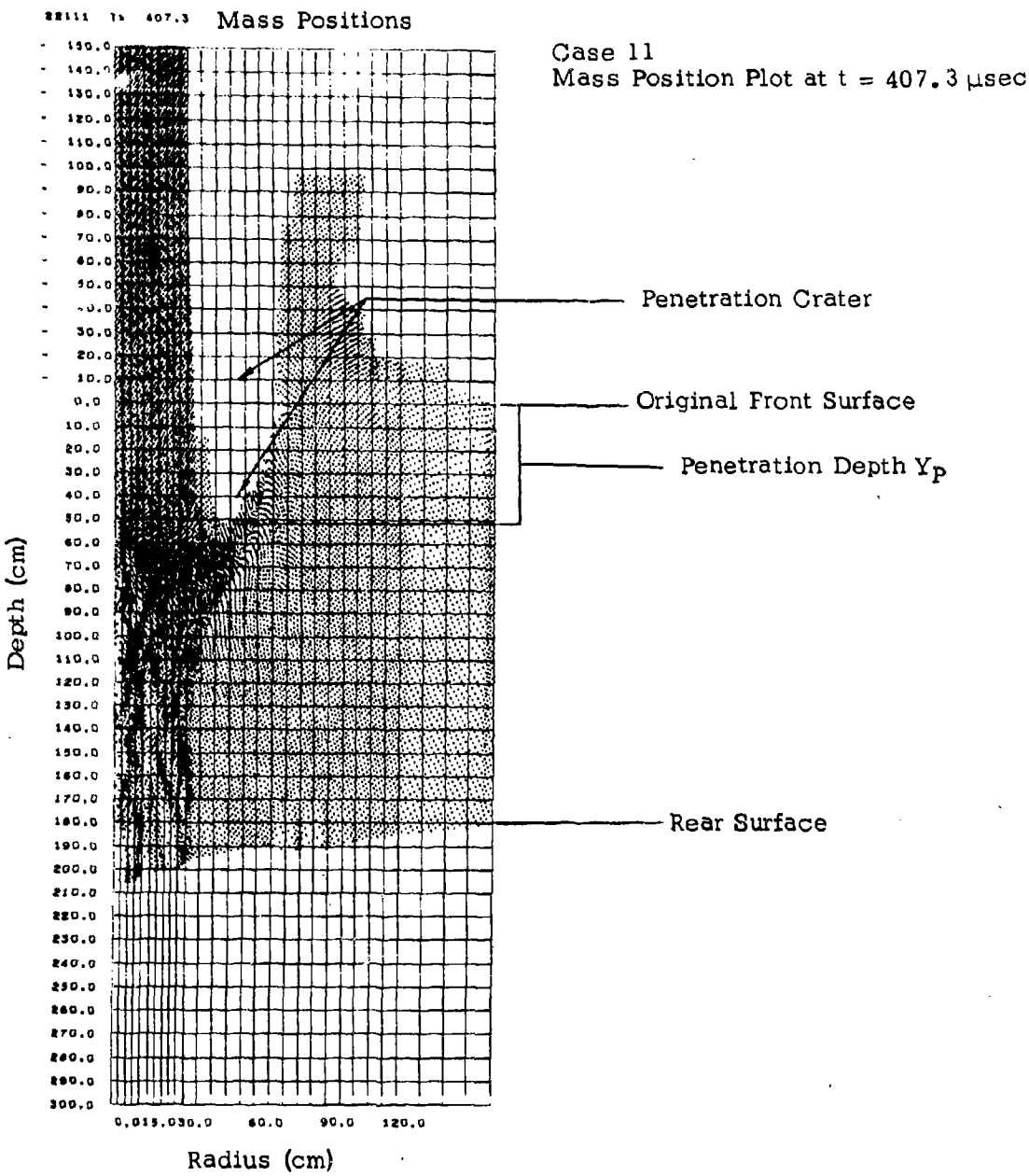

Figure 2-2 Definition of Penetration Crater and Penetration Depth

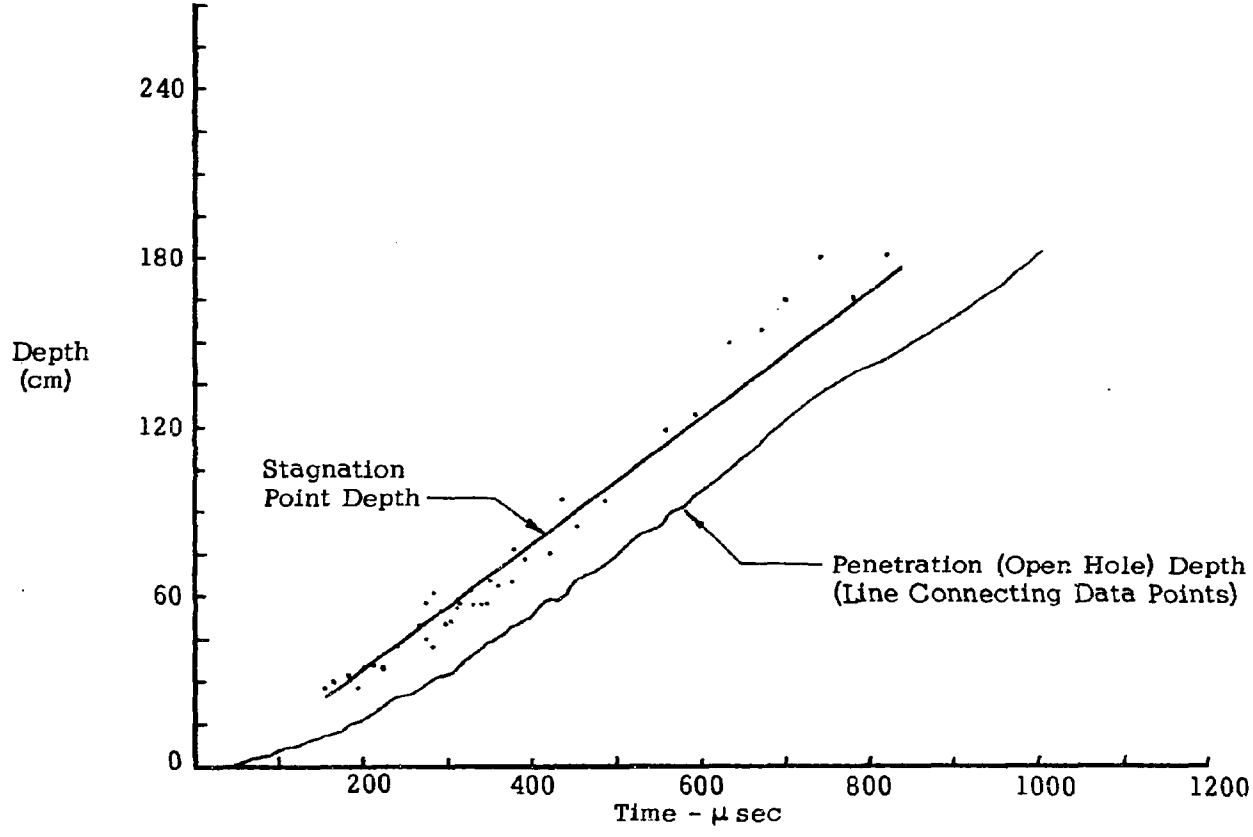

Figure 2-3 Depth of Stagnation Point and Open Hole vs Time for Al-Al Impact at 4.6 km/sec (Case 11)

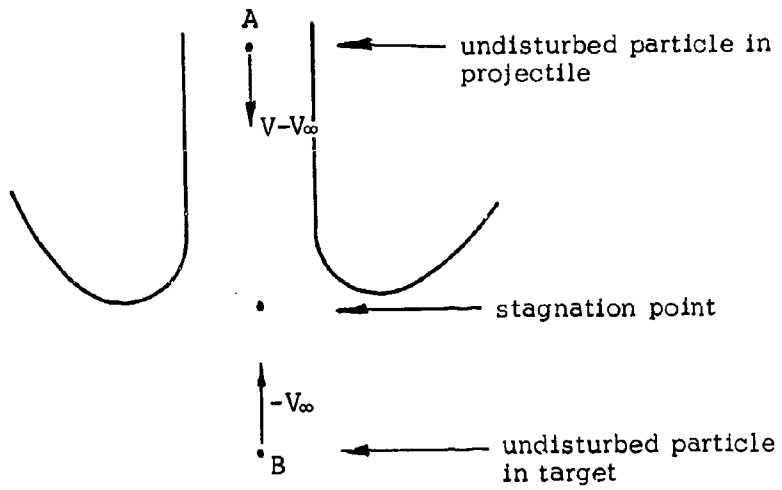

At point A, P, $e_P = 0$ and $u = V - V_\infty$. Hence, eqn. (2-1) has a constant value of $1/2\ (V - V_\infty)^2$ on a steady state streamline in the projectile. (V is the impact velocity, and the subscripts P and T refer to projectile and target conditions.)

At point B, P, $e_T = 0$ and $u = -V_\infty$. On a streamline in the target, eqn. (2-1) therefore has a constant value of $1/2\ V_\infty^2$.

Evaluation of eqn. (2-1) at the stagnation point leads to:

(in projectile)

$$\frac{P}{\rho_P} + e_P = \frac{1}{2}(V - V_\infty)^2 \tag{2-2}$$

(in target)

$$\frac{P}{\rho_T} + e_T = \frac{1}{2} V_\infty^2 \tag{2-3}$$

Eliminating P gives:

$$(V - V_\infty)^2 \rho_P - V_\infty^2 \rho_T = 2(e_P\rho_P - e_T\rho_T) \tag{2-4}$$

For similar material impacts, $\rho_P = \rho_T$ and $e_P = e_T$. In such impacts, we thus obtain

$$V_\infty = \frac{V}{2} \tag{2-5}$$

Under conditions approaching incompressible flow, the right hand side of eqn. (2-4) becomes small compared to either of the terms on the left side, and vanishes in the limit. This permits us to evaluate the stagnation point velocity for dissimilar material impacts, i.e.

$$(V - V_\infty)^2 \rho_P = V_\infty^2 \rho_T$$

$$\frac{V}{V_\infty} - 1 = \sqrt{\frac{\rho_T}{\rho_P}}$$

or $$V_\infty = \frac{V}{1 + \sqrt{\frac{\rho_T}{\rho_P}}} \qquad (2-6)$$

In Figure 2-3, we have also plotted the depth of the stagnation point, Y_S, vs time. The position of the stagnation point is not readily apparent from plots of numerical solutions where the laboratory frame of reference is used. To locate the point, we therefore used the numerical solutions to determine velocity vs depth at various times along the axis, and find the depth at which the velocity drops to half the impact velocity, i.e.

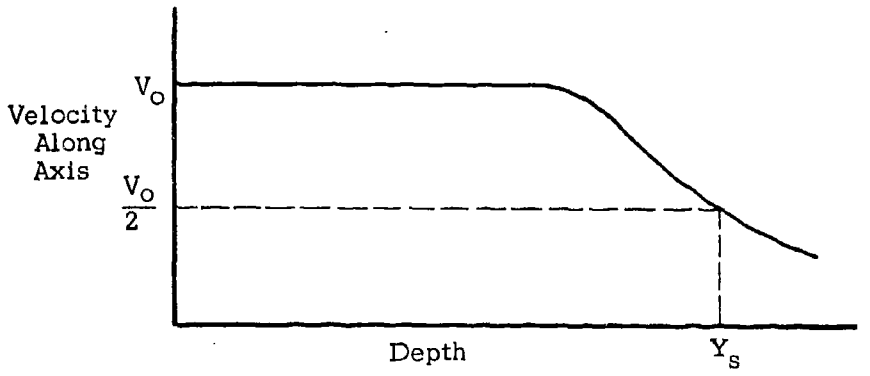

The Y_S vs t points in Figure 2-3 can be reasonably well fit by a straight line, the slope of which is 2.3, or V/2. Such a fit is parallel to the Y_P vs t data, and is offset by about D/2. Thus $Y_S \cong Y_P + D/2$.

The conclusion of the steady state phase is brought about by the interactions with the rear free surface. The presence of this free surface is felt, of course, at an early time in the solution, as soon as the initial shock first reaches that surface. To the extent that this shock is one-dimensional, the free surface immediately achieves a velocity nearly equal

to the impact velocity. For the thicker targets which we have been considering, however, lateral rarefactions so reduce the strength of the impulse delivered to the rear surface that its initial velocity is a fraction of the impact velocity. For the T/D = 2 and T/D = 3 targets, for example, the initial velocity of the rear surface is less than half the impact velocity. The intermediate material between the rear surface and the stagnation point is at an even lower velocity. As the stagnation point moves further into the target and becomes correspondingly closer to the rear free surface, the elevated pressures will provide additional accelerating force to the intervening material. Eventually all that material will be moving at the stagnation point velocity or higher, a condition which we find to exist by the time $Y_p = T$. The steady state condition is assumed to be concluded at that point.

2.1.3 Breakthrough Phase

There follows the final, or breakthrough phase of the impact response, during which the rod interaction with the target is complete and the residual length passes through an open hole. It is not practical to analyze this phase in detail by means of numerical hydrodynamic solutions. We believe, however, that breakthrough constitutes a relatively unimportant phase in the overall rod loss process.

During the breakthrough phase, the rod must clear its way through the remaining rear surface debris. For $Y_p \geq T$, it is seen in the numerical solutions that the average density of such debris is low, indicating a shattered state. The total mass ahead of the projectile is therefore small. Furthermore, although the magnitude of the debris velocity is less than that of the residual rods, some of the debris is diverging, so that much of the shattered mass will move radially out of the path of the residual rod. We conclude that the extent of rod loss caused by further interactions between debris and rod will be small by comparison with the rod loss due to the initial transient and to steady state flow.

2.2 DEVELOPMENT OF EQUATIONS FOR PREDICTING ROD LOSS

Further analysis of the above-described mechanisms of the transient and steady state portions of the penetration process permits the derivation of a relationship for rod loss in terms of impact velocity, rod diameter and material, and plate thickness and material. In this derivation, it is hypothesized that no significant rod loss occurs after the open hole depth reaches the original rear surface of the target, i.e., when $Y_p = T$. The validity of this hypothesis is examined further in Section 2.3.2, wherein the rod loss equation is compared with experimental observations.

2.2.1 Basic Rod Loss Equation

As noted in Section 2.1.2, at the stagnation point near the bottom of the hole, rod material is diverted radially. Pressures above the stagnation point drop rapidly, so it is reasonable to consider that the residual tip of the intact rod is always located at the bottom of the hole. Thus, if rod loss is completed when $Y_p = T$, the final tip of the rod will be located at the position of the original rear surface of the plate, as indicated in Figure 2-4b. At the time of impact this final rod tip is located, as shown in Figure 2-4a, at a point ΔL ahead of the target front surface, where ΔL is the length of rod loss.

Defining t_f as the time required for the open hole depth, Y_p, to equal the plate thickness, T, it is seen that

$$Vt_f = \Delta L + T \tag{2-7}$$

Now consider the manner in which the penetration depth Y_P varies with time. As was seen in Section 2.1.2, the steady state penetration rate for similar material impacts is V/2. In Figure 2-3, the plot of Y_P vs t approaches V/2 asymtotically. This suggests an exponential fit of the form

$$Y_P = \frac{V}{2} \{ t - \tau (1-e^{-t/\tau}) \} \tag{2-8}$$

in which τ is the time characteristic of the transient phase. For the general case of non-similar impacts, V_∞ would be substituted for V/2, giving

$$Y_P = V_\infty \{ t - \tau (1-e^{-t/\tau}) \} \tag{2-9}$$

Since we assume that rod loss stops when $Y_P = T$ at time t_f, eqn. (2-8) becomes

$$T = \frac{V}{2} \{ t_f - \tau (1-e^{-t_f/\tau}) \} \tag{2-10}$$

or alternatively

$$\frac{T}{D} = \frac{V\tau}{2D} \{ \frac{t_f}{\tau} - 1 + e^{-t_f/\tau} \} \tag{2-11}$$

Substituting t_f from eqn. (2-7),

$$\frac{\Delta L}{D} = \frac{V\tau}{D} + \frac{T}{D} - \frac{V\tau}{D} e^{-(\frac{\Delta L + T}{V\tau})} \tag{2-12}$$

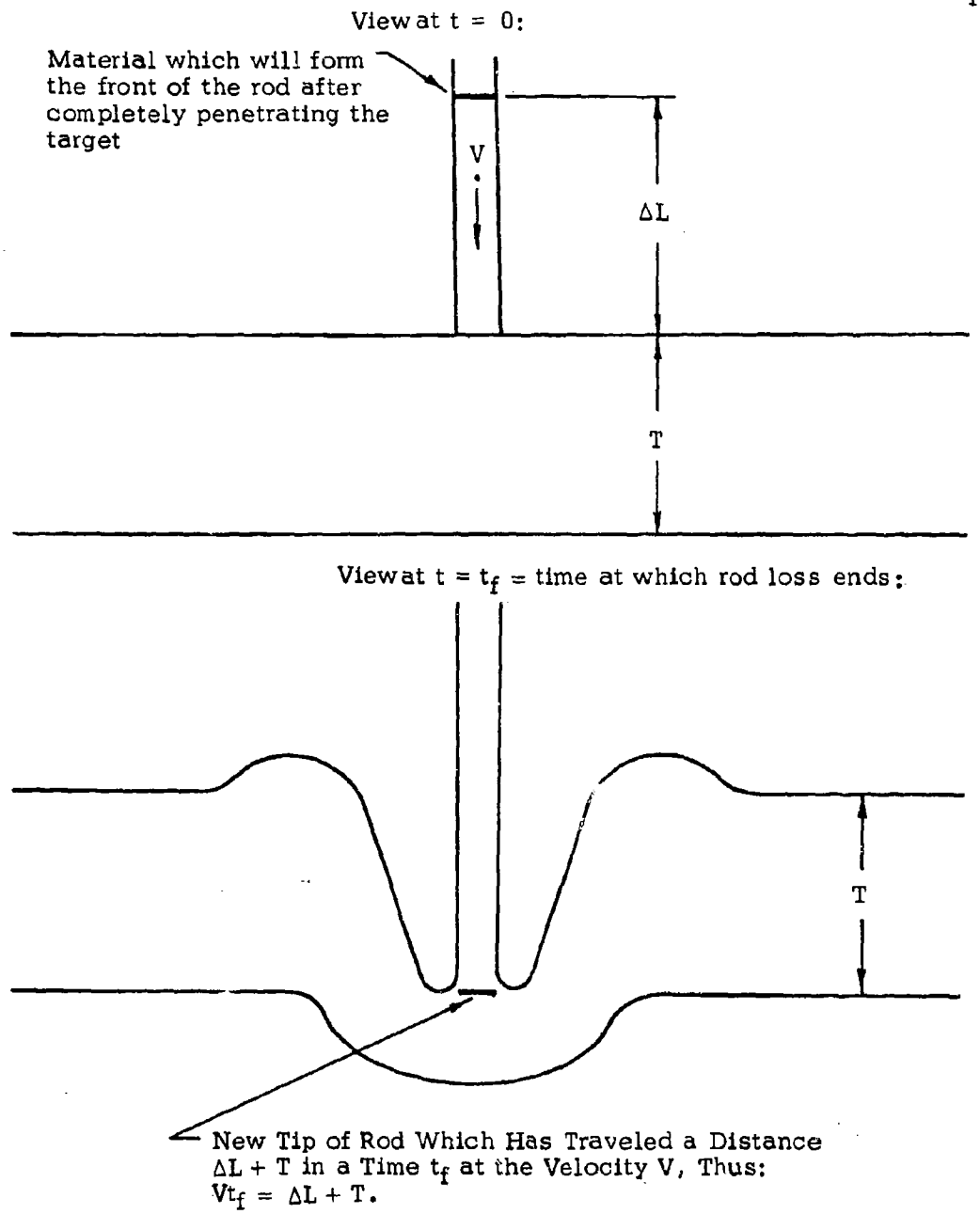

Figure 2-4 Definition of Terms Used in Rod Loss Derivation

Our assumption that rod loss stops at $Y_p = T$ is limited to large values of T/D. For these cases, the exponential term in eqn. (2-12) becomes insignificant, and we obtain the basic relationship for rod loss in large T/D impact cases.

$$\frac{\Delta L}{D} = \frac{V\tau}{D} + \frac{T}{D} \tag{2-13}$$

2.2.2 Evaluation of $V\tau/D$ From Numerical Data

As $t \rightarrow \infty$, the exponential relationship for Y_p vs t in eqn. (2-8) becomes

$$Y_p = \frac{V}{2}\ (t - \tau) \tag{2-14}$$

which is the equation of the straight line to which eqn. (2-8) is asymptotic. Equations of this form can be nominally fit to Y_p vs t data obtained from numerical solutions to determine approximate values for time characteristics. This is done in Figure 2-5 for impact Case 11. The time intercept of the V/2 asymptote gives τ to be 200. Evidence that both this value and the hypothesized exponential relationship in eqn. (2-8) are valid is shown by the excellent fit of the numerical points in Figure 2-5.

For aluminum-aluminum impacts at 4.6 km/sec, the value of $V\tau/D$ in eqn. (2-13) is thus established as .5, and that relationship becomes

$$\frac{\Delta L}{D} = 1.5 + \frac{T}{D} \tag{2-15}$$

Note that although D = 60 cm was used in the numerical solutions (and in evaluating τ) $V\tau/D$ is dimensionless and can be applied to any scale impact.

2.2.3 $V\tau/D$ For Other Similar-Material Impacts and Velocities

τ is related to the time required for the one-dimensional nature of the initial shock systems to be destroyed by the lateral rarefaction waves, which we will call τ_o. The relationship between τ and τ_o is probably complex, but for the present purposes it is reasonable to assume that τ is proportional to τ_o, i.e.

$$\tau = a\tau_o \tag{2-16}$$

From this, it is possible to establish the value of $V\tau/D$ for other conditions of impacting materials and velocities.

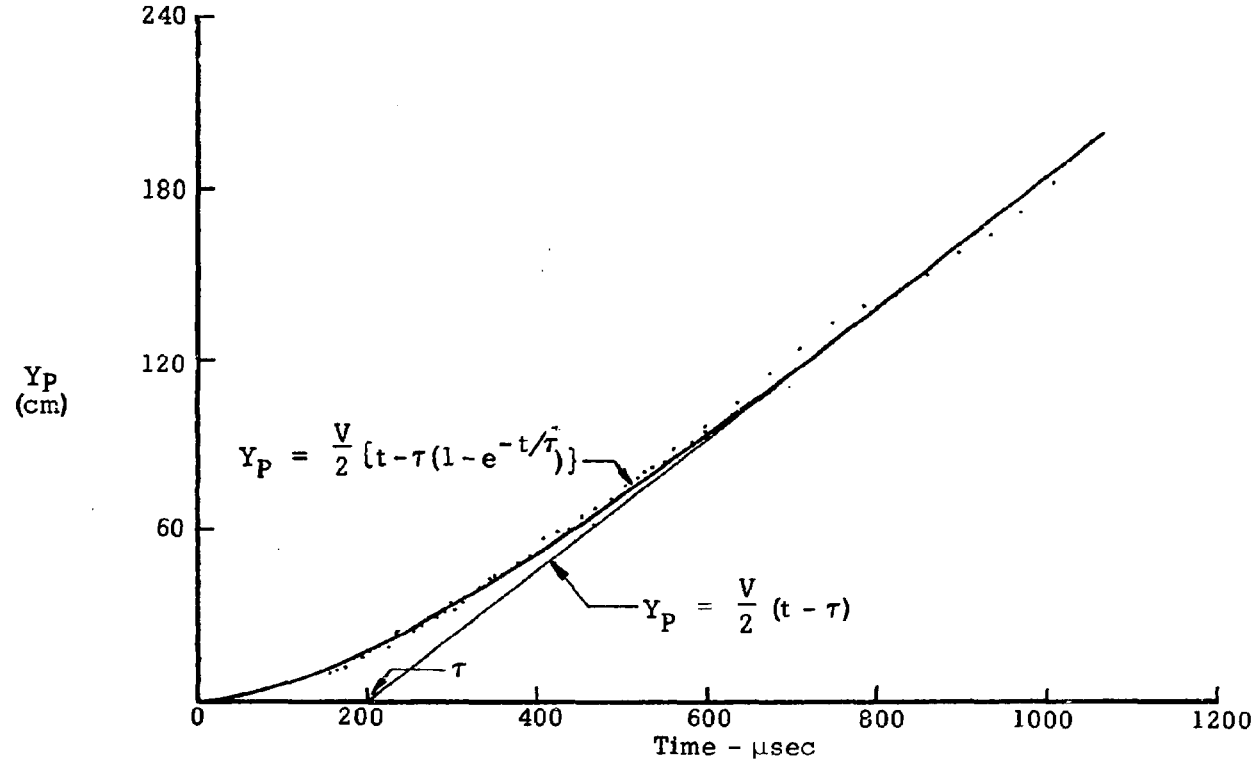

Figure 2-5 Evaluation of Characteristic Time τ Using Y_P vs t Data For Case 11 (Al → Al @ 4.6 km/sec)

The head of the lateral rarefaction fan propagates into the initial one-dimensional high pressure region with local sound speed C. Thus

$$\tau_o = \frac{D/2}{\sqrt{C^2 - (S - V/2)^2}} \tag{2-17}$$

where S is the shock speed corresponding to impact velocity V. C and S can be evaluated from an equation of state. Using the Los Alamos equation of state, τ_o for aluminum impacts at 4.6 km/μsec is 54.25. This leads to a proportionality constant in eqn. (2-16) of 3.69. Thus we arrive at the following general relationship for evaluating $V\tau/D$ in eqn. (2-13) for similar material impacts:

$$\frac{V\tau}{D} = \frac{1.84\,V}{\sqrt{C^2 - (S-V/2)^2}} \tag{2-18}$$

2.2.4 Simple Method for Estimating $V\tau/D$ Term

Where it is inconvenient to obtain the required one-dimensional shock information required for eqn. (2-18), (i.e. C and S as functions of V), a less accurate but simpler method can be used to obtain rod loss estimates for a given impact. This method is based upon the two assumptions

a) Shock velocity is linear with particle velocity, i.e.

$$S = A + Bu \tag{2-19}$$

b) Sound velocity is related to shock velocity by

$$C^2 = .49\,S^2 + (S - V/2)^2 \tag{2-20}$$

The relationship in eqn. (2-20) is suggested in reference 4.

Substituting eqn. (2-19) and (2-20) into (2-18), leads to the approximation

$$\frac{V\tau}{D} = \frac{2.63\,V}{A + \frac{BV}{2}} \tag{2-21}$$

which can be used in eqn. (2-13). Values of A and B in this approximation are given in Table 2-1, along with calculated values of $V\tau/D$ for impacts at 4.6 and 6.1 km/sec.

Table 2-1
Values of A, B, and $V\tau/D$ For
Similar-Material Impacts of Various Materials

Material	Density gm/cm^3	A km/sec	B	Reference	$V\tau/D$ V=4.6 km/sec	6.1 km/sec
Ag	10.49	3.215	1.643	5	1.7	2.0
Al	2.785	5.37	1.339	6	1.4	1.7
Au	19.24	3.059	1.608	5	1.8	2.0
Be	1.845	7.975	1.091	5	1.2	1.4
Cd	8.64	2.408	1.718	5	1.9	2.1
Co	8.82	4.652	1.506	5	1.5	1.7
Cr	7.13	5.176	1.537	5	1.4	1.6
Cu	8.9	3.972	1.478	5	1.6	1.9
Fe	7.85	3.8	1.580	6	1.6	1.9
In	7.27	2.370	1.608	5	2.0	2.2
Mg	1.735	4.493	1.266	5	1.6	1.9
Mo	10.2	5.173	1.204	5	1.5	1.8
Nb	8.604	4.447	1.212	5	1.7	2.0
Ni	8.86	4.667	1.410	5	1.5	1.8
Pb	11.34	2.066	1.517	5	2.2	2.4
Pd	11.95	3.793	1.922	5	1.5	1.7
Pt	21.37	3.671	1.405	5	1.8	2.0
Rh	12.42	4.68	1.645	5	1.4	1.7
Sn	7.28	2.668	1.428	5	2.0	2.3
Ta	16.46	3.374	1.155	5	2.0	2.3
Th	11.68	2.079	1.381	5	2.3	2.6
Ti	4.51	4.786	1.066	5	1.7	2.0
Tl	11.84	1.821	1.566	5	2.2	2.4
W	19.17	4.005	1.268	6	1.7	2.0
Zn	7.135	3.042	1.576	5	1.8	2.0
Zr	6.49	3.771	.933	5	2.0	2.4

Indications of the accuracy of this approximation are seen in Figures 2-6 and 2-7 for Al vs Al and Fe vs Fe impacts. These plots compare $V\tau/D$ as calculated by the more exact eqn. (2-18) with the approximation of eqn. (2-21). It is seen that eqn. (2-21) understates $V\tau/D$ for aluminum by approximately 0.1 - 0.2 diameters over a wide velocity range. In iron, eqn. (2-21) overstates $V\tau/D$ by up to 0.3 diameters at velocities above 0.2 cm/μsec. While these discrepancies are relatively small, some changes in the ordering of material effectiveness may occur when the different rod loss prediction equations are used.

2.2.5 Extension to Dissimilar-Material Impacts

An insufficient number of dissimilar-material cases were solved numerically to permit us to directly derive relationships for rod loss in such cases. However, we believe that adequate predictions can be made for dissimilar impacts by using incompressible jet theory to modify eqn. (2-13). Thus

$$\left(\frac{\Delta L}{D}\right)_{P \to T} = \sqrt{\frac{\rho_T}{\rho_P}} \left(\frac{\Delta L}{D}\right)_{T \to T} \qquad (2\text{-}22)$$

First calculate $\Delta L/D$ from eqn. (2-13) for an impact where the projectile is assumed to be of the same material as the actual target material. Then multiply this result by the square root of the ratio of the densities of the target material and the actual projectile material to obtain the predicted rod loss.

2.3 COMPARISON OF ROD LOSS EQUATION WITH NUMERICAL SOLUTIONS AND EXPERIMENTAL DATA

2.3.1 Numerical Solutions

The detailed results of the numerical solutions conducted during this investigation are given by spatial plots of mass positions, velocity fields, and pressure contours in reference 1 and in the Appendix to this report. From these solutions, penetration depths (or the depth of the open hole, Y_p) can be plotted as functions of time. To obtain the penetration depth from the numerical solutions, density contours near the bottom of the open hole were examined. The density in the hole is of course zero, but the walls and bottoms of the holes are seen as sharp density gradients in the numerical results, rather than as discontinuities. For consistency, we define the surface as the density contour where the compression is 0.5.

Plots of penetration depth vs time appear in Figure 2-8 for Al-Al impacts at 4.6 km/sec into targets having T/D values of 1/4, 1/2, 1, 2, 3 and 5. For the small T/D impacts, the penetration rates, dY_p/dt accelerate through the steady state velocity $V_\infty = V/2$ due to the early

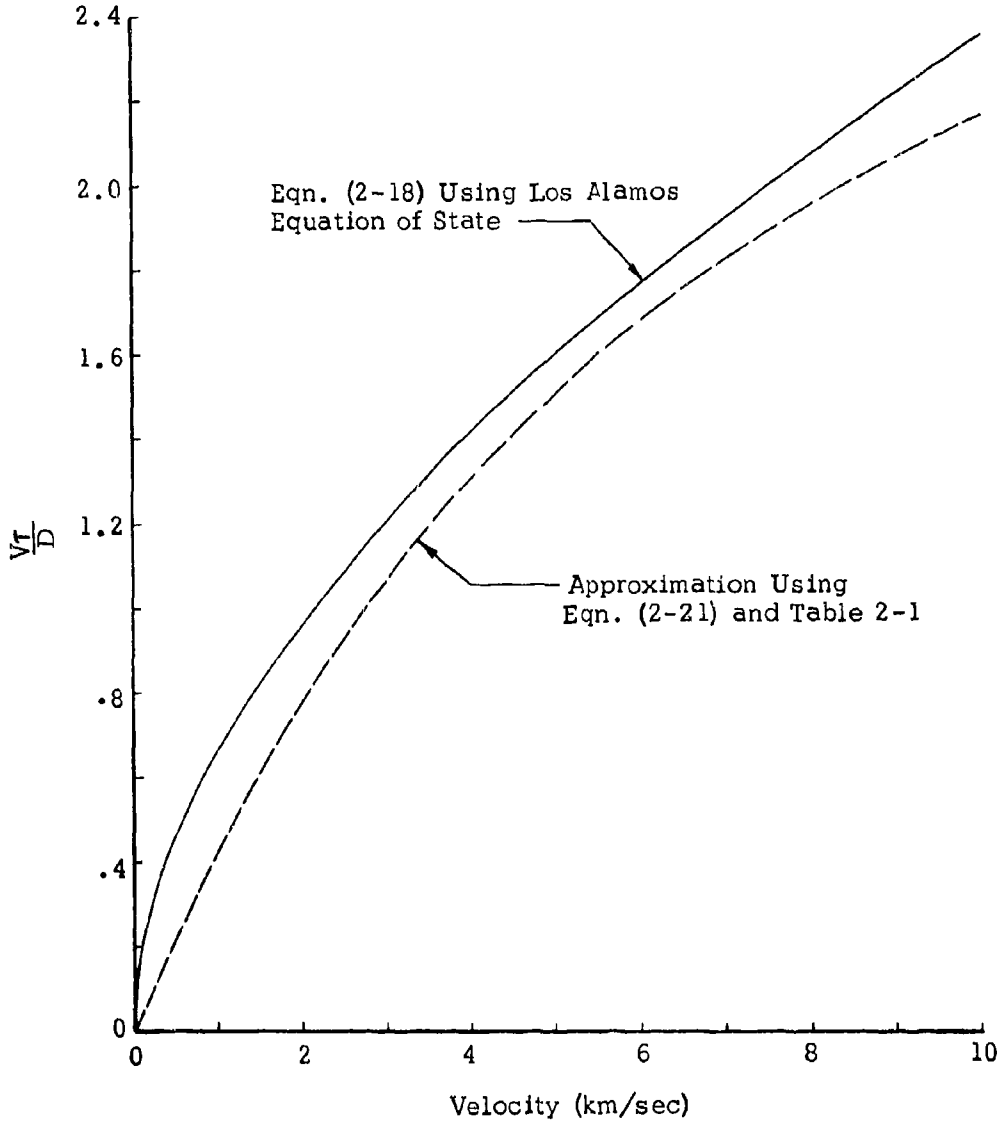

Figure 2-6 $V\tau/D$ vs Velocity For Aluminum-Aluminum Impacts

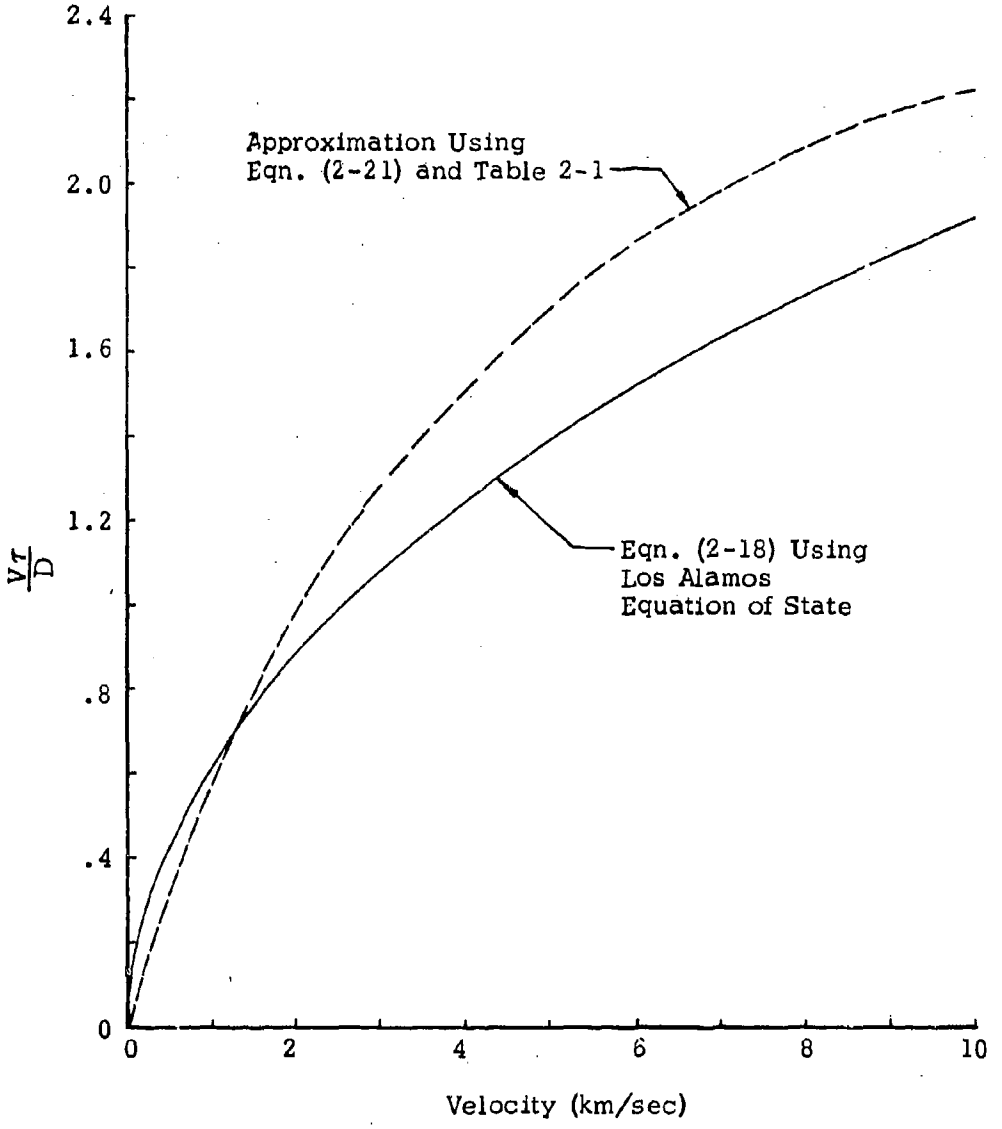

Figure 2-7 $V\tau/D$ vs Velocity For Iron-Iron Impacts

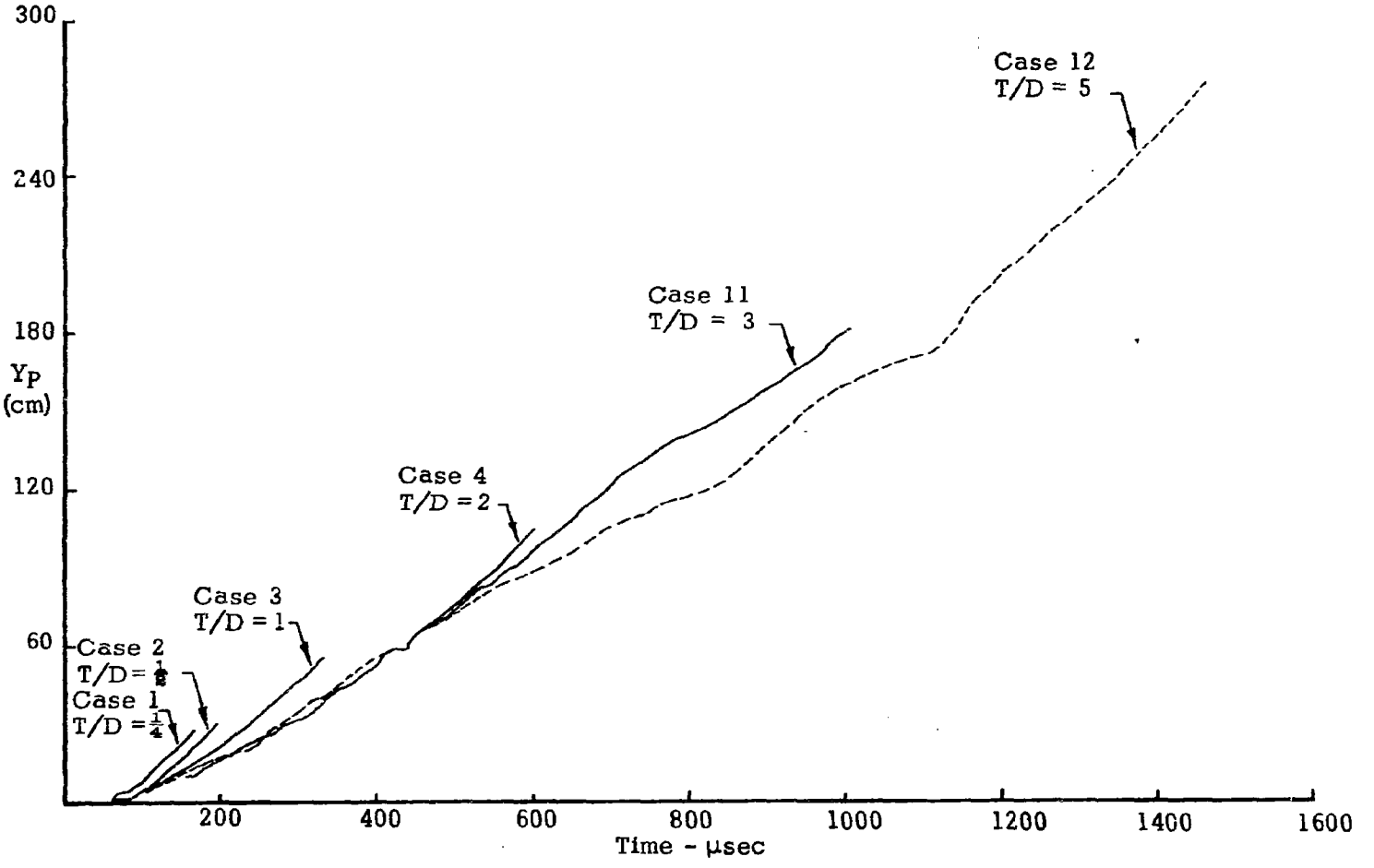

Figure 2-8 Penetration Depths vs Time for Aluminum - Aluminum Impacts at 4.6 km/sec

influence of the rear free surface. For the T/D = 2 and 3 cases, the penetration rates asymtotically approach V/2. (Case 12, T/D = 5, produced somewhat erratic Y_p vs t results due to the numerous grid changes necessitated by the long running time.)

2.3.2 Comparisons With Experimental Data (Confidential)

A series of tests have been performed by the Naval Research Laboratory in a parallel experimental investigation of rod impact phenomena. Primary observations in these experiments were the residual rod lengths after perforating plates of various thicknesses. From these observations the length of rod shattered as a function of plate thickness was determined.

2.3.2.1 Aluminum-Aluminum Targets (Confidential)

Figure 2-9 summarizes Al-Al impact data at 4.6 km/sec. NRL has fit these data by the straight dotted line. It is seen that the numerically-derived rod loss equation predicts the experimental data to within about 0.3 rod diameters. Although experimental scatter is evident, the under-prediction appears systematic. This suggests the magnitude of rod erosion which may be attributed to the breakthrough phase (which was neglected in the development of eqn. (2-13)). For a T/D = 3 impact, each phase would account for the following losses:

Initial Transient:	$(V\tau/D)$	1.5
Steady State:	T/D	3.
Breakthrough:	0.3	0.3

Thus a third term might appropriately be appended to eqn. (2-13) to account for the breakthrough phase, i.e.

$$\frac{\Delta L}{D} = \frac{V\tau}{D} + \frac{T}{D} + 0.3 \qquad (2\text{-}23)$$

Only very limited data are available regarding the effects of velocity upon rod loss for target thicknesses equal to or above the $T/D \geq 2$ condition. These are shown in Figure 2-10 and compared with the prediction of eqn. (2-23).

As previously emphasized, the rod loss equations have been derived for relatively thick targets (i.e. $T/D \geq 2$). When applied to thin targets, these relationships tend to overpredict the rod loss. To illustrate, T/D = 1 data are included in Figure 2-10, and eqn. (2-23) is shown by a dotted curve for comparison. The experimental data all fall somewhat below the theoretical curve.

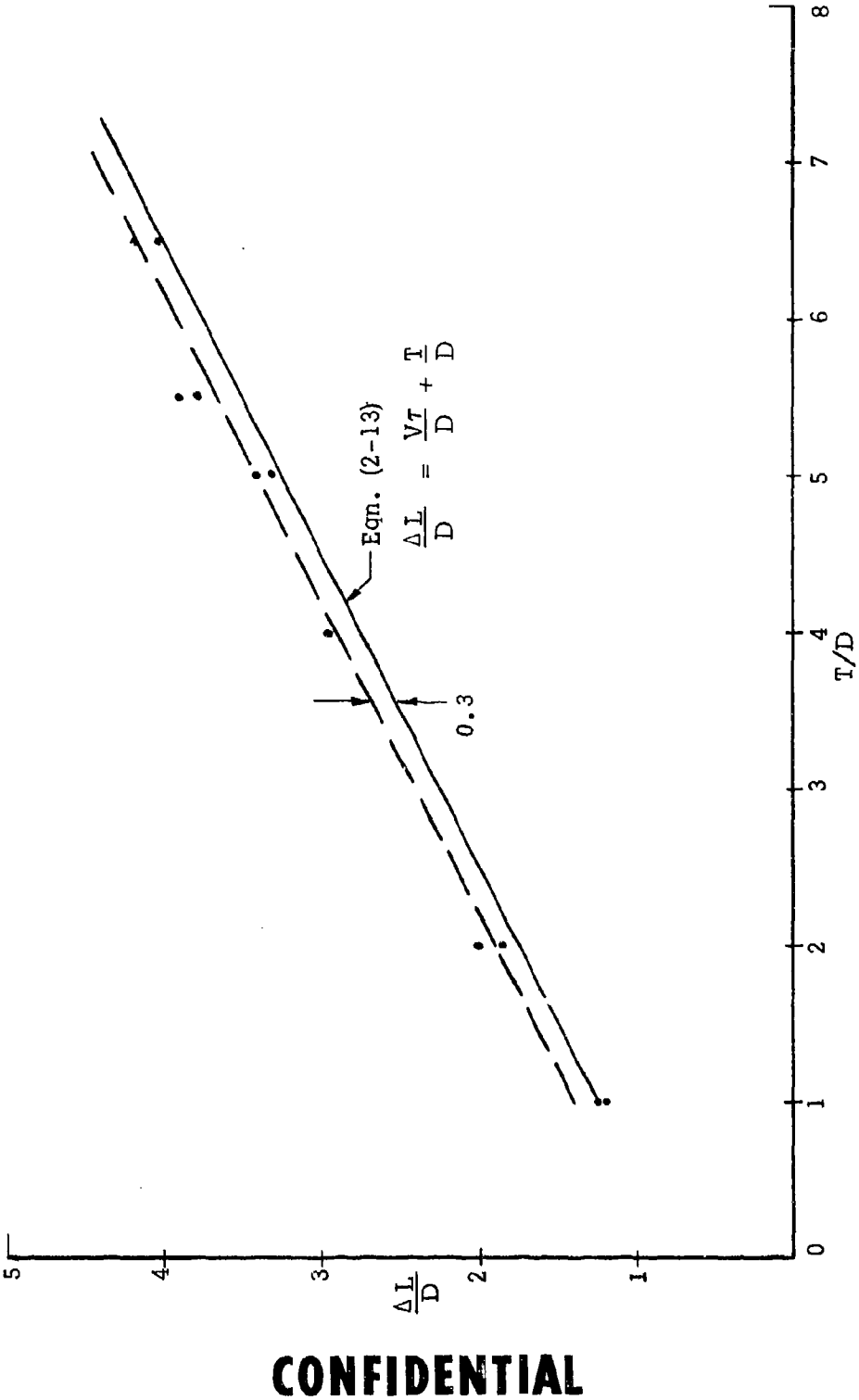

Figure 2-9 Comparison of Rod Loss Prediction Equation With Experimental Data for Aluminum - Aluminum Impacts at 4.6 Km/sec

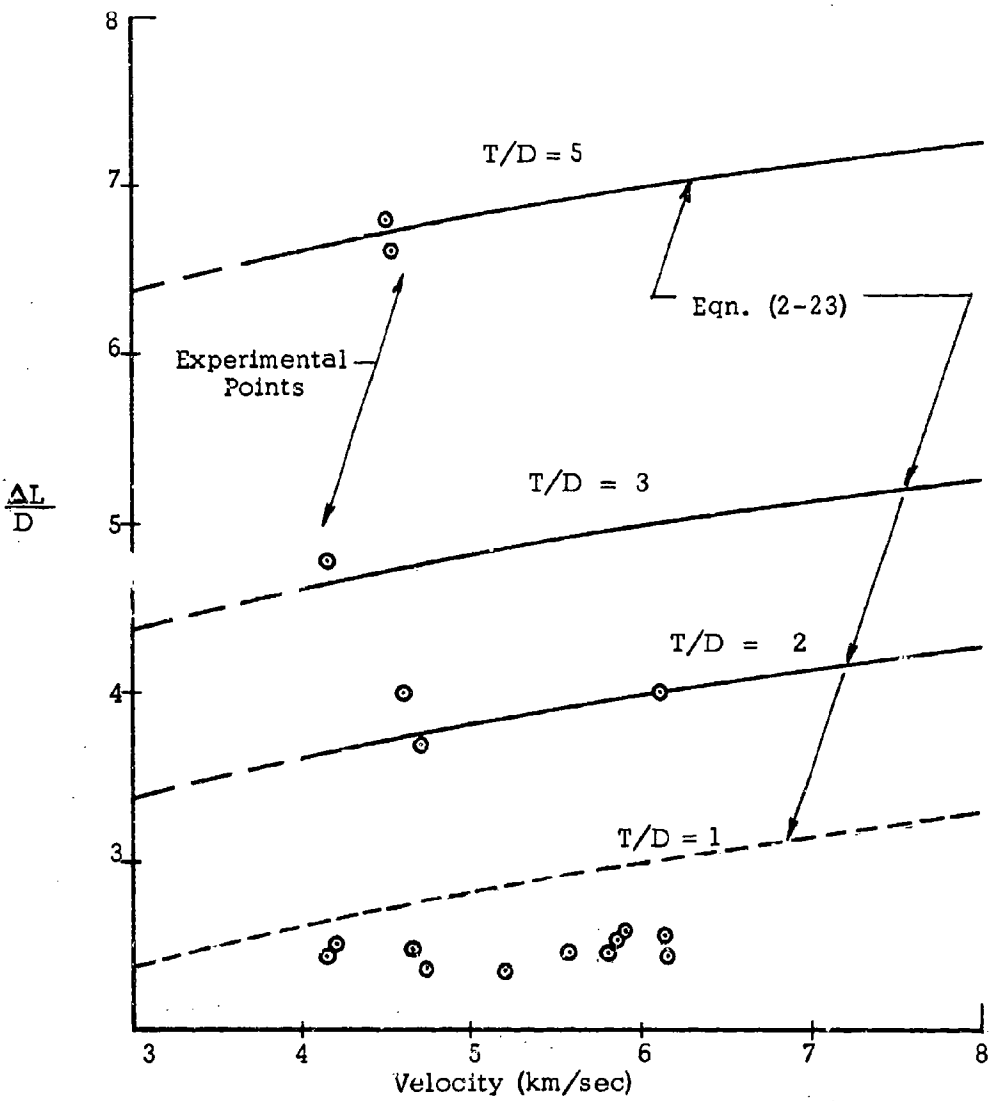

Figure 2-10 Comparison of Rod Loss Prediction Equation with Experimental Data for Aluminum-Aluminum Impacts Showing E[illegible] of Velocity

2.3.2.2 Dissimilar Targets (Confidential)

The NRL experiments also included a number of impacts of other dissimilar materials. Many of these impacts were against T/D = 1.0 targets, and are again below the thicknesses for which eqn. (2-13) and (2-22) were derived. Figure 2-11 shows the experimental points and the prediction curves for the materials and velocities involved as determined from the rod loss eqn. (2-23) as modified by eqn. (2-22) for dissimilar materials.

2.4 THIN PLATE IMPACTS (Confidential)

The rod loss equation developed in Section 2.2.1 applies to impacts where the target thickness is of the order of twice the rod diameter or greater ($T/D \geq 2$). For thinner targets, the penetration phenomena never approach the quasi-steady state conditions which eqn. (2-13) presumes.

During the initial part of this investigation reported in reference 1, a rod shattering criterion was hypothesized for application to thin plate impacts. This criterion used the peak pressure propagating up the rod axis to establish the length of rod shattered (i.e. shattering would stop when the peak dropped below a critical level.) By preliminary comparisons with experiments, this critical value was set at 100 kb for aluminum alloys. Application of this criterion to aluminum rod impacts into thin aluminum plates led to the conclusion that a plateau would exist in rod loss as the target thickness increased. Based on this study, the relationship of $\Delta L/D$ to T/D indicated by the heavy line in Figure 2-12 was suggested. Experimental data from NRL appears to confirm the existence of such a plateau, as is seen in Figure 2-13 (the heavy line is a fit by NRL).

Use of the peak pressure criterion, however, also led to the prediction in reference 1 that rod loss would sharply increase with impact velocity. Comparison of the experimental data for 4.6 and 6.1 km/sec impacts in Figure 2-13 shows this prediction to be incorrect. Thus while the peak pressure criterion indicates the existence of a rod shattering plateau which is apparently verified by experimental data, this simple criterion is inadequate to describe the several processes which are involved in thin plate rod loss. To correctly describe these processes almost certainly requires a comprehensive model which incorporates material strength effects as well as fracture criteria and the properties of the materials after failure.

In the absence of a rigorous analytical treatment of the very thin plate regime, it is of interest to note that the experimental data in this regime can be fit reasonably well by the exponential form given in eqn. (2-12). To this equation can be added the 0.3 offset term indicated by the experimental comparison in Section 2.3.2.1.

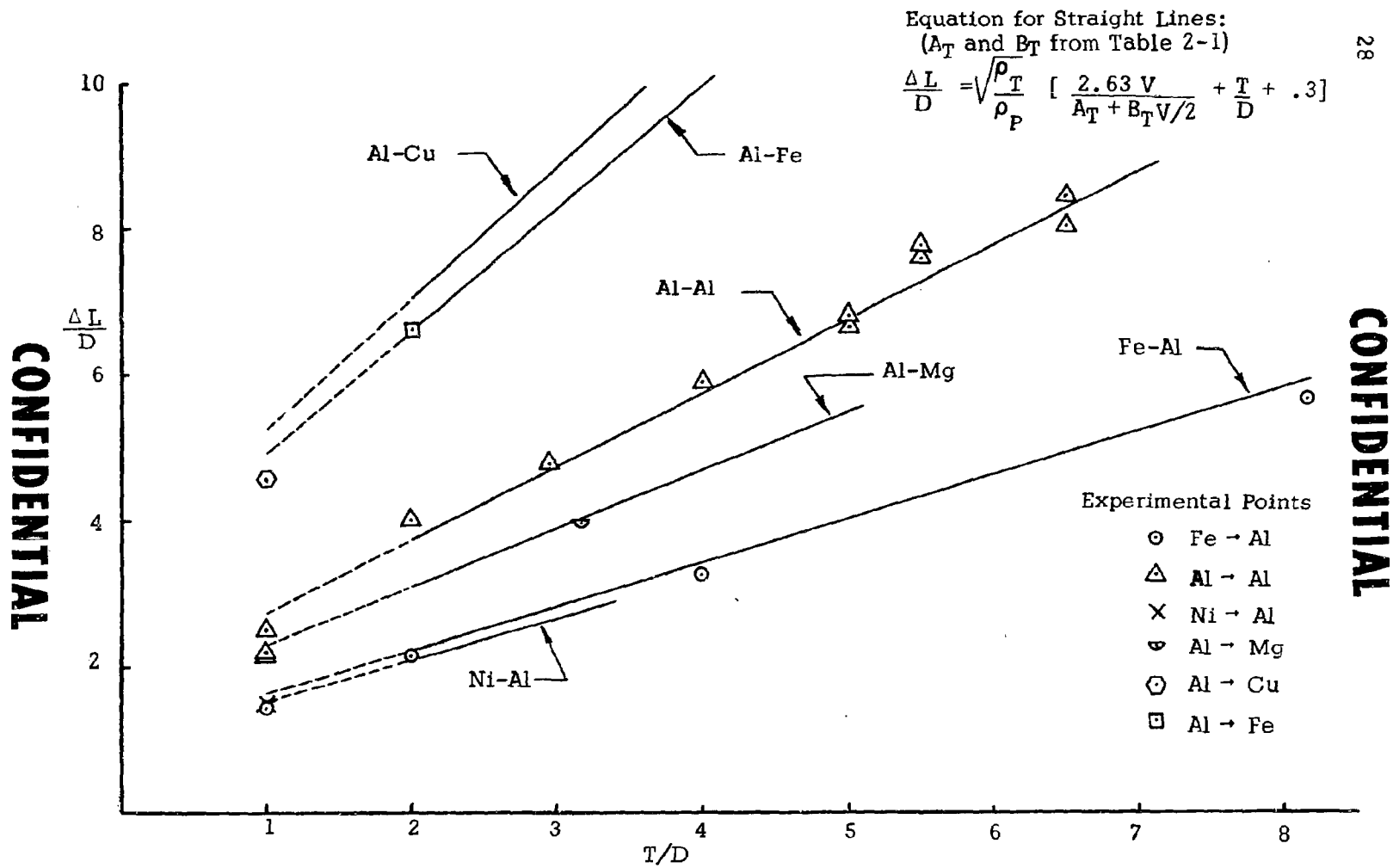

Figure 2-11 Comparison of Rod Loss Prediction Equation With Experimental Data for Dissimilar Material Impacts at 4.6 km/sec

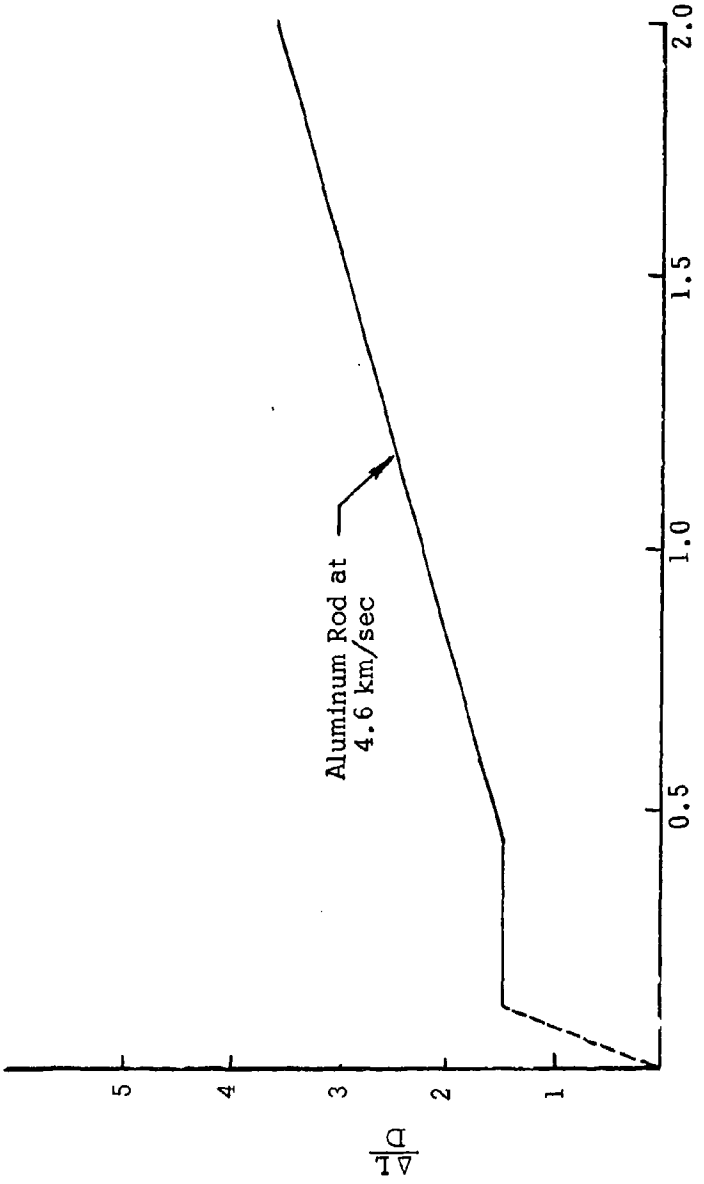

FIGURE 2-12 Rod Loss Relationship for Aluminum Impacts Suggested By Earlier Analytical Study (Ref. 1).

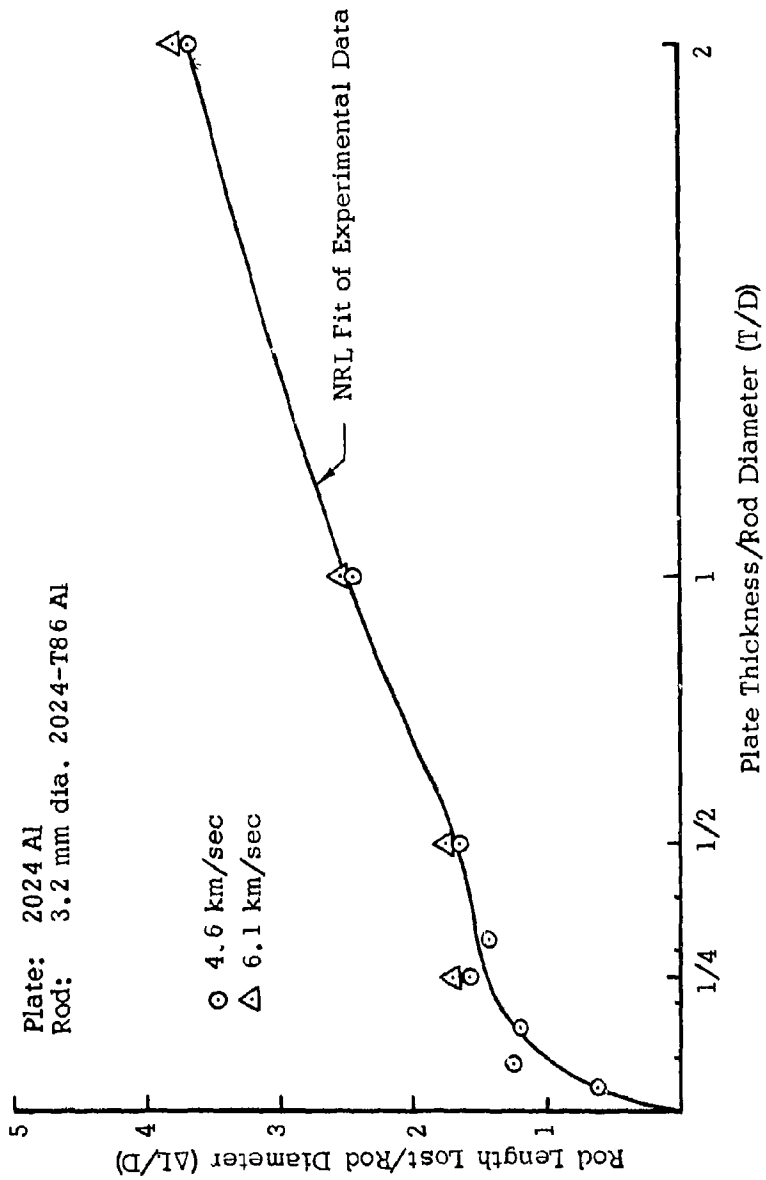

Figure 2-13: NRL Rod Loss Observations Suggesting Plateau for Aluminum - Aluminum Impacts

Figure 2-14 shows a comparison of this equation with experimental data over the entire T/D range of available data. We emphasize that while there is a physical basis for applying eqn. (2-12) to thick targets, it represents only a convenient empirical fit of experimental data for thin targets (T/D less than 1).

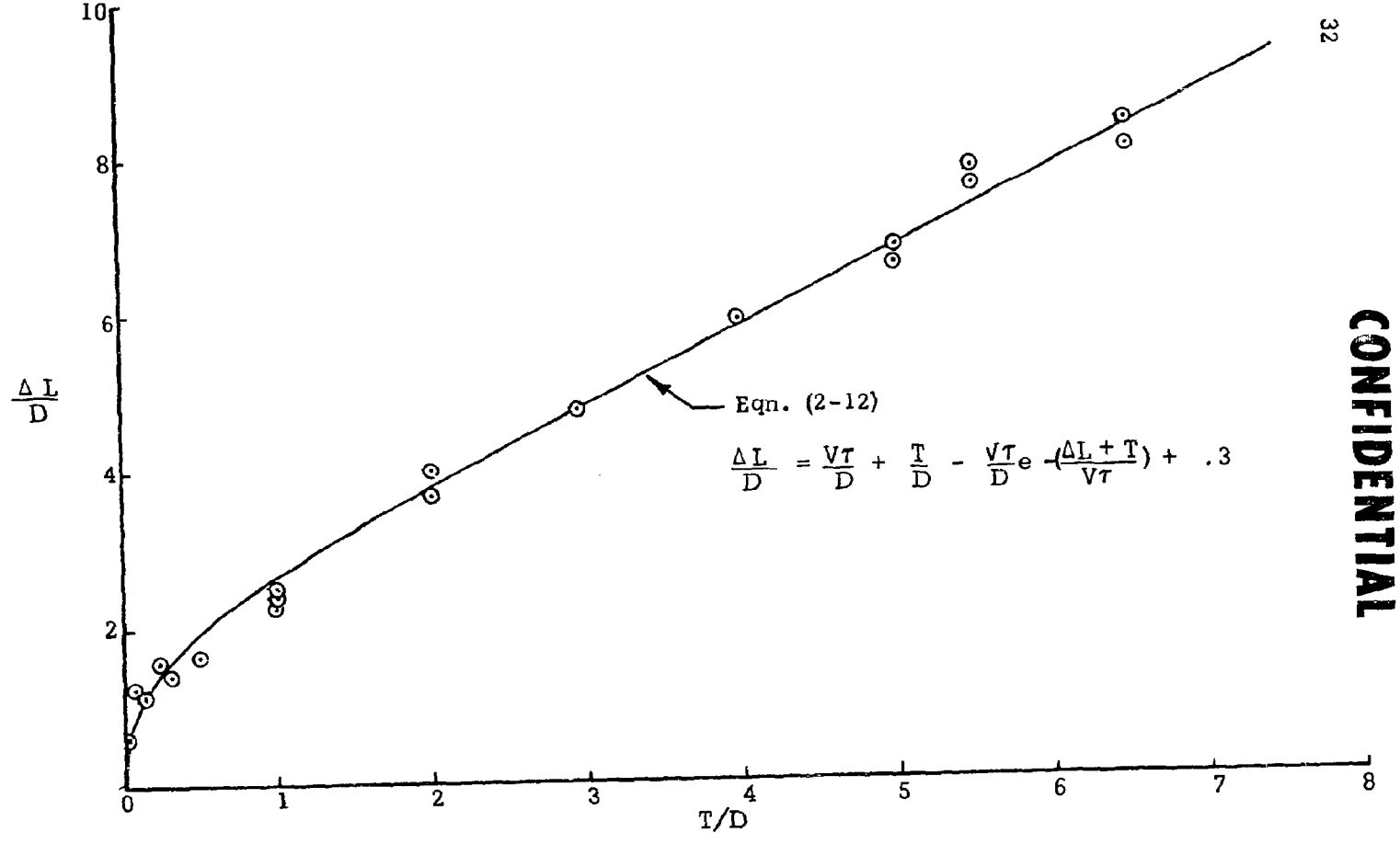

Figure 2-14 Comparison of Experimental Rod Loss Data With Exponential Equation for Aluminum-Aluminum Impacts at 4.6 km/sec

3. OBLIQUE IMPACTS

3.1 PLANAR APPROXIMATION

Three space dimensions are required to properly define oblique impact geometries. At the time the solutions in this study were performed, no suitable three-dimensional numerical technique was available. Invoking certain approximations, however, it is possible to analyze oblique impacts in two space dimensions, and from such solutions to obtain semi-quantitative information about such impacts.

For these analyses, end-oriented rods impacting at oblique incidence are approximated by the two-dimensional geometry of an infinitely wide plate impacting on its edge against an infinitely wide target, as illustrated in Figure 3-1. A plane erected normal to the target and to the projectile plate produces a two-dimensional cross section of the problem. We will refer to the numerical analyses of such plane strain cases as planar solutions.

The assumption of plane strain to describe oblique incidence precludes any action in the direction normal to the plane of the solution (z-direction). Thus, geometric divergence of the shock wave in the z-direction is ignored. Conversely, free surfaces do not exist in the z-direction; hence convergence of rarefactions from that direction is ignored. Certain qualitative observations can therefore be made regarding differences between true three-dimensional geometries and planar approximations:

a. At a given depth in the target, the planar solutions will predict a higher peak shock pressure, energy, and momentum density than exists in the real three-dimensional case.

b. The initial transient stage will be prolonged in the planar solution (as compared to the three-dimensional case).

It is important to note, however, that the steady state characteristics (stagnation pressure, velocity, etc.) are the same for both the planar and three-dimensional cases. Thus, after the initial transient has passed, the rate of rod loss and of hole growth will be the same for both cases.

3.2 NUMERICAL SOLUTIONS

Planar solutions were obtained for 30° and 60° incidence impacts. A normal incidence case was also included in order to provide a direct comparison between an approximated (planar) solution and a correct axisymmetric solution of the same impact. From this comparison, a method was devised for converting certain data obtained from planar solutions to three-dimensional impact problems.

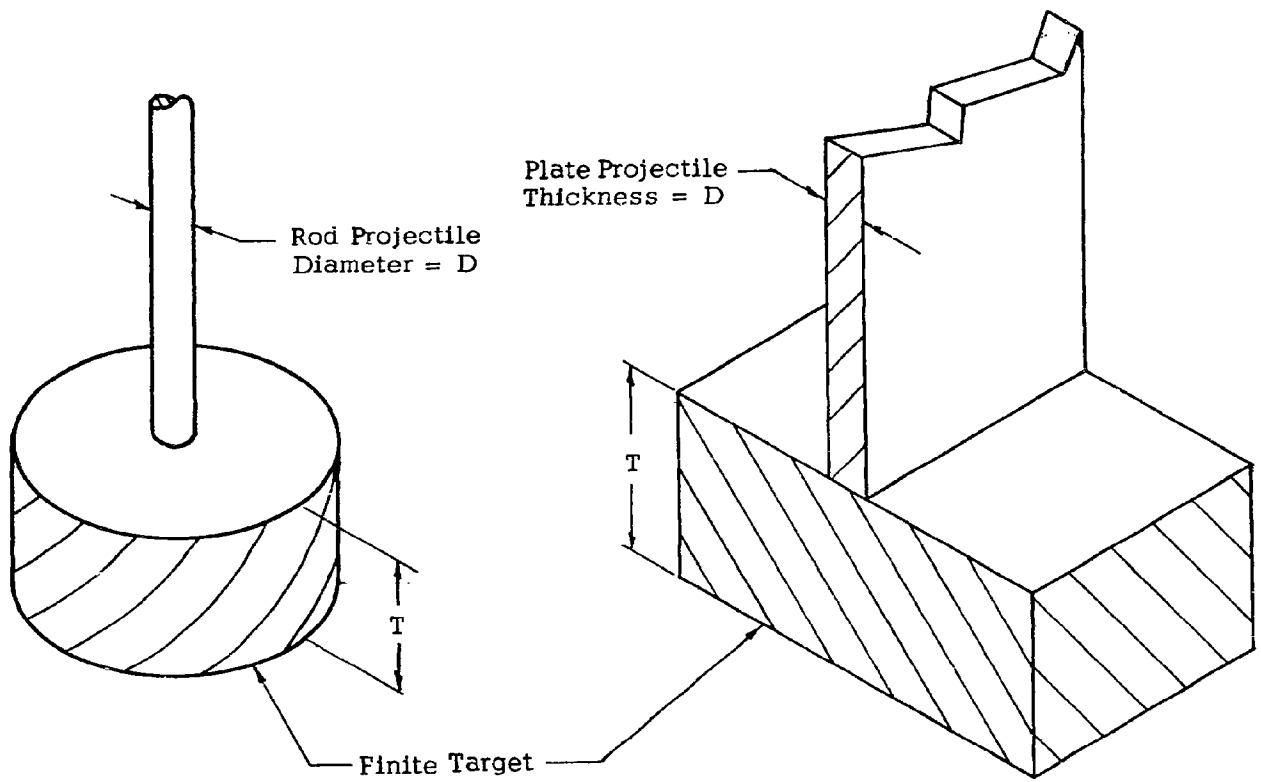

Figure 3-1 Axisymmetric vs Planar Solutions

3.2.1 Planar vs Axisymmetric Solutions

The impact case chosen for this comparison was for aluminum vs aluminum at 4.6 km/sec, where the target thickness is twice the projectile diameter or thickness (i.e., T/D = 2.) This impact geometry was analyzed as an axisymmetric problem in Case 4 in reference 1.

At early stages, the plotted solutions are nearly identical. In Figure 3-2, the positions of the heads of the rarefaction fans are compared 12 - 14 μsec after impact. In both cases, the fans emanate from the original corner made by the side of the projectile and the target face, and the head of the wave propagates into the high pressure state at the same velocity. Behind the front, however, the relaxation of pressure occurs more rapidly in the axisymmetric case, due to the diverging geometry.

Figures 3-3 and 3-4 compare the mass and velocity plots at about 122 μsec, by which time significant differences are appearing. In Figure 3-3, the depth of the open hole is seen to be appreciably greater in the axisymmetric case. Conversely, in the velocity plot in Figure 3-4, a somewhat larger region is seen to be engulfed by the shock in the planar case.

The depth of the open hole continues to be greater in the axisymmetric case throughout the solution. This is seen in Figure 3-5, in which Y_p vs t data are plotted for both cases. These curves are seen to be nominally parallel and separated by approximately 75 μsec. (It takes the planar solution 75 μsec longer than the axisymmetric solutions to open the same hole depth.) This difference arises entirely in the initial transient stage, which persists for a longer time in the planar case due to the slower relaxation by lateral rarefactions. Thus, the time characteristic τ_{PL} for the initial transient in the planar solution is 275 μsec, as compared with τ = 200 μsec for the axisymmetric solution, or

$$\tau_{3\text{-}D} = \tau_{PL} \left(\frac{200}{275}\right) = .73\, \tau_{PL} \qquad (3\text{-}1)$$

Once the steady state is reached, hole growth proceeds at the same rate for both cases. Insofar as open hole growth curves are concerned, the planar solutions can be converted to an equivalent three-dimensional solution by transposing the curve in accordance with eqn. (3-1).

The fact that τ is significantly larger in planar cases has another effect on these solutions. As is evident in Figure 2-5, steady state conditions are not achieved until two or three time characteristics, τ, have elapsed. For the impact treated in Case 31, this would mean that 500 - 700 μsec will elapse before the steady state is reached. By this time, however, the open hole is approaching the rear target surface, and no steady state is possible. This situation is analogous to small T/D cases in axisymmetric geometry. Thus the effective T/D for a planar solution is smaller than indicated by the dimensions of the problem.

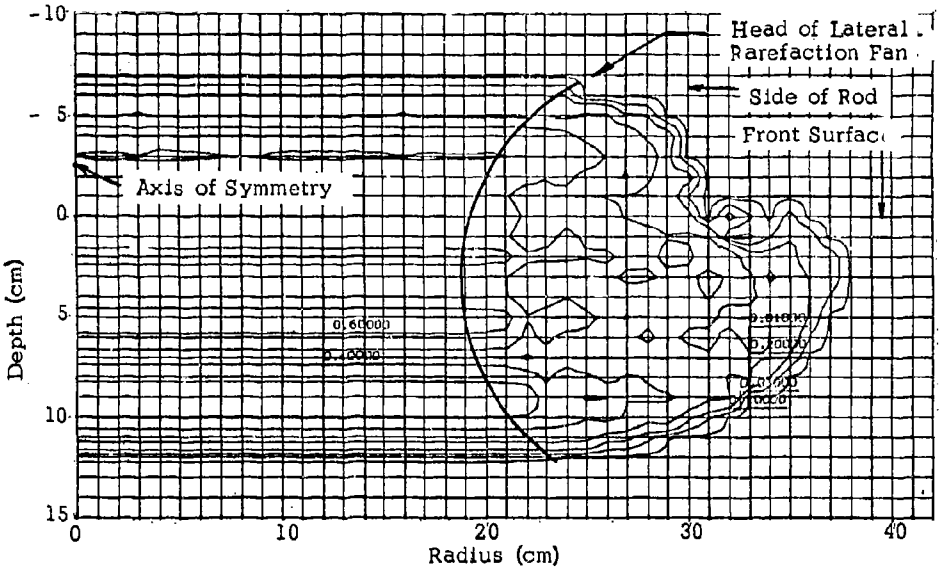

AXISYMMETRIC IMPACT AT 13.2μsec

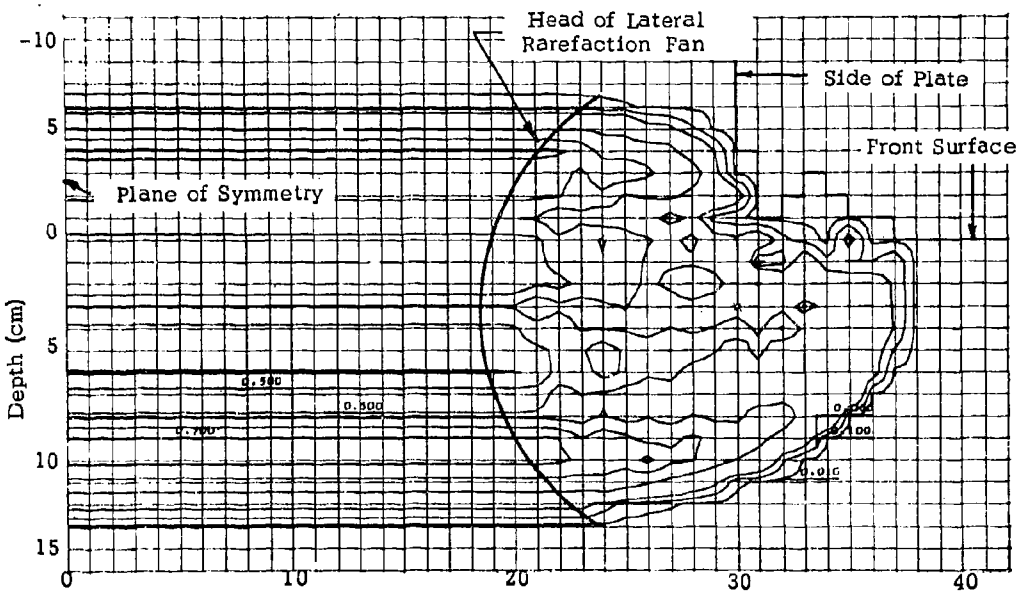

PLANAR IMPACT AT 13.9 μsec

Figure 3-2 Comparison of Shock and Rarefaction Systems in Axisymmetric and Planar Solutions (Al vs Al at 4.6 km/sec)

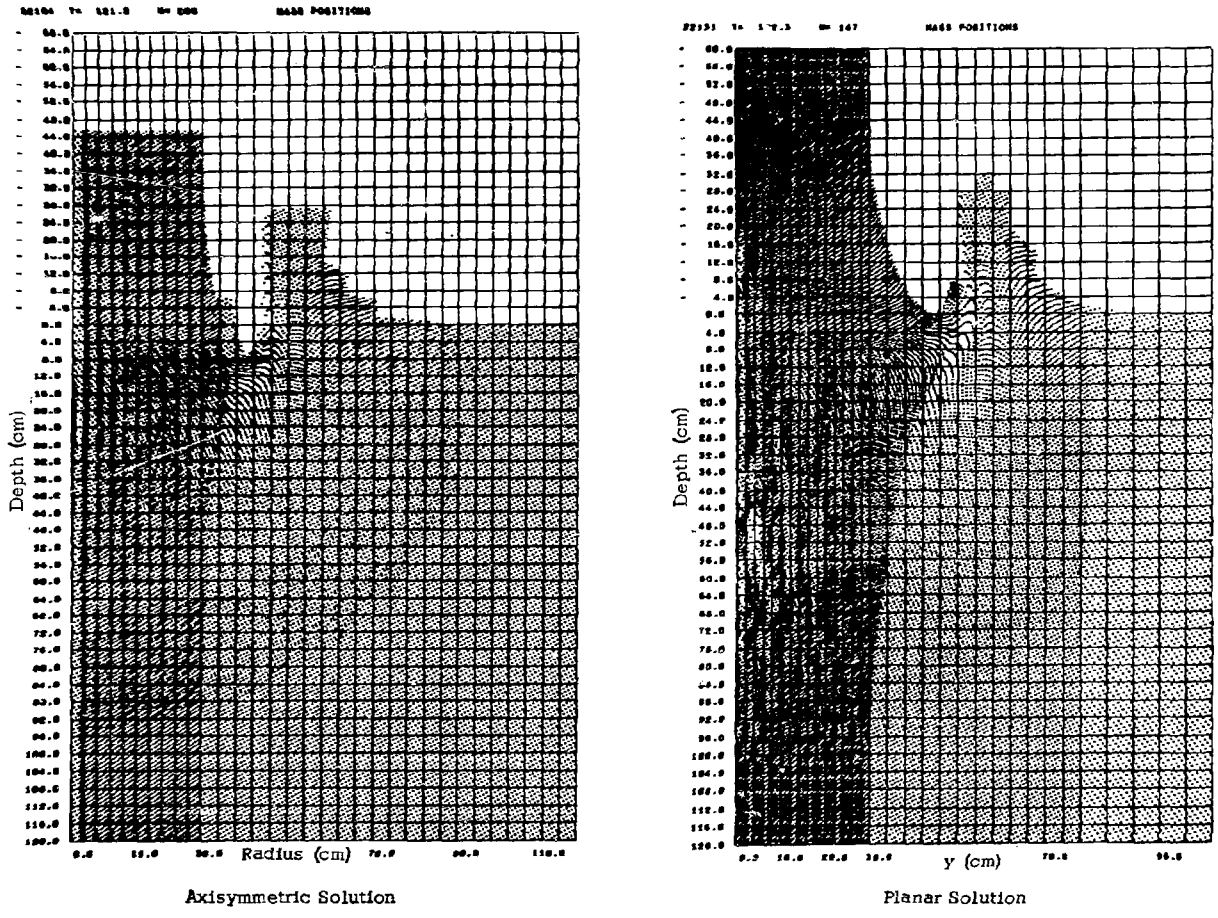

Figure 3-3 Comparison of Mass Positions at 122 μsec for Axisymmetric and Planar Solutions of Normal Impact of Aluminum on Aluminum at 4.6 km/sec

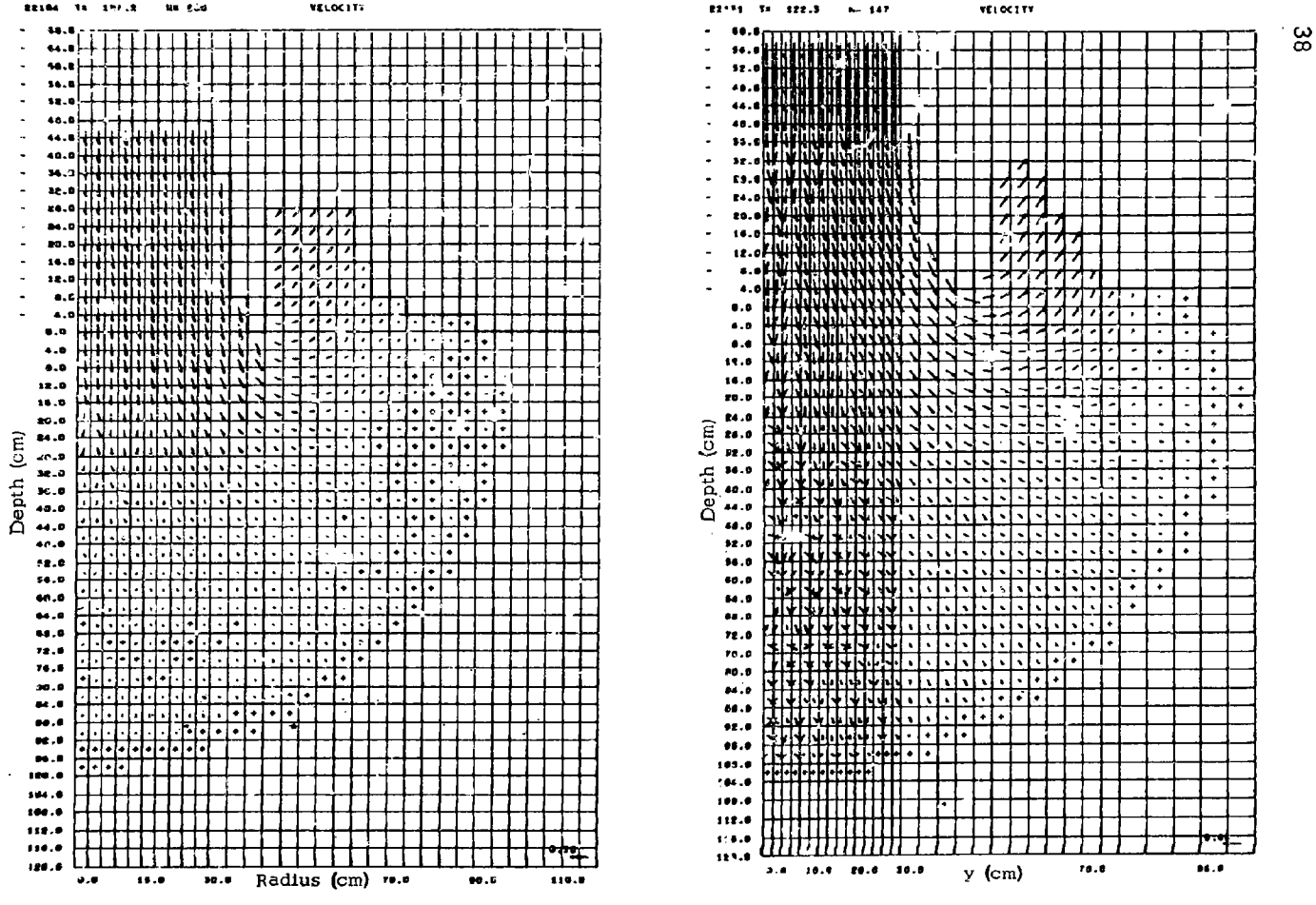

Axisymmetric Solution

Planar Solution

Figure 3-4 Comparison of Velocity Fields at 122 μsec for Axisymmetric and Planar Solutions of Normal Impact of Aluminum on Aluminum at 4.6 km/sec

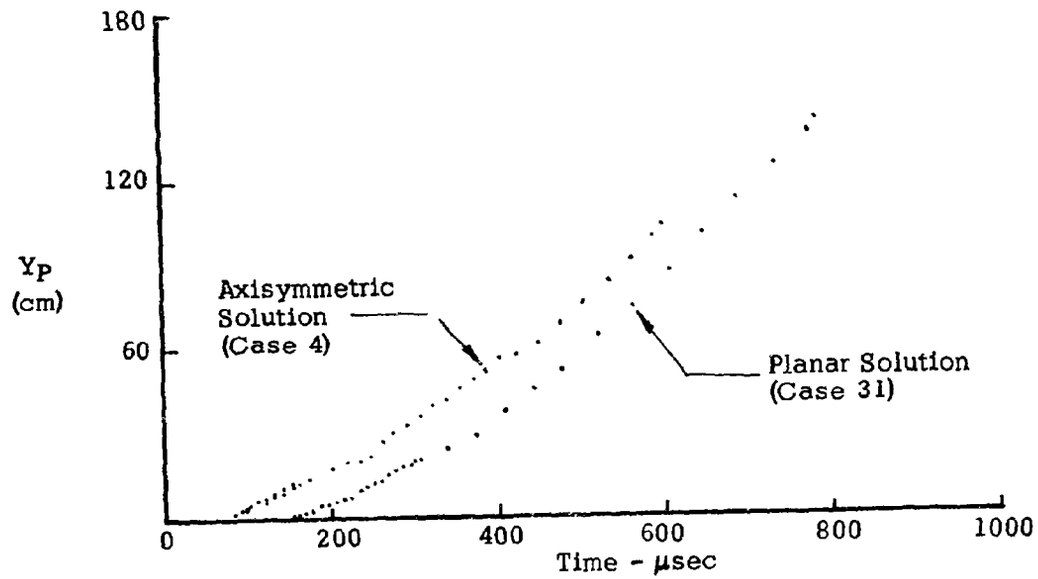

Figure 3-5 Comparison of Penetration Depth vs Time for Axisymmetric and Planar Solutions of Normal Impact at 4.6 km/sec of Aluminum into Aluminum

A second important quantitative comparison between axisymmetric and planar representation is the peak pressure on the axis. Figure 3-6 shows these data. Large differences are seen, with the plane strain case retaining a given pressure level to greater depths than the axisymmetric case. Again, this is due to the absence of lateral rarefactions in the planar case.

In summary, it is seen that the planar representation of three-dimensional geometries has two important effects on penetration and projectile shattering.

1. Because the transient phase is prolonged in planar geometry, the length of rod lost during this relatively inefficient period is greater than in the case in the axial symmetry. Hence, a planar analysis will tend to overestimate the actual projectile loss.

2. Because the peak pressure reaching the rear surface is greater in the planar case (and also because the initial transient lasts longer) a planar solution for a given T/D corresponds to a smaller T/D for an axisymmetric solution.

3.2.2 30° and 60° Impacts

Spatial plots and descriptions of the planar solutions of 30° and 60° impacts are given in the Appendix. Figure 3-7, showing plots of the penetration (open hole) depth Y_p vs time obtained from the solutions, provides the basis for modifying the rod loss eqns. (2-12) and (2-13) for oblique impacts. Figure 3-7 compares Y_p vs t for the 30° and 60° cases with the data from the planar solution of a normal incidence case. It is seen that the angle of obliquity does not significantly affect either the duration of the initial transient stage, or the steady state perforation rate.

3.3 MODIFICATION OF ROD LOSS EQUATION FOR OBLIQUE IMPACTS

Equation (2-13) gives the rod loss relationship for normal incidence, i.e.

$$\frac{\Delta L}{D} = \frac{V\tau}{D} + \frac{T}{D} \qquad (2\text{-}13)$$

The transient and steady state terms of this equation can be appropriately modified for oblique impacts by reference to the numerical solutions and to the oblique geometry.

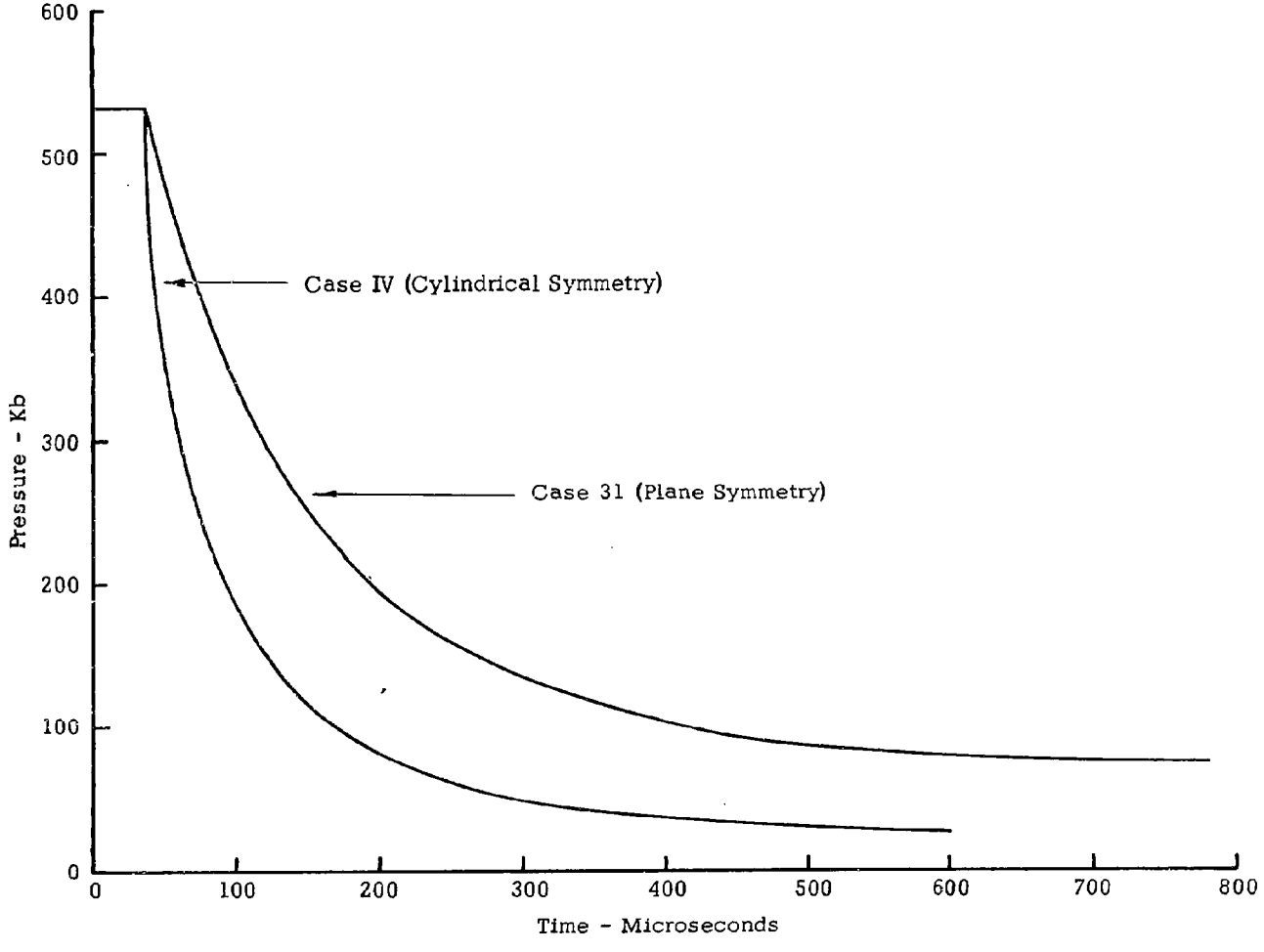

Figure 3-6 Maximum Pressure vs Time on the Axis

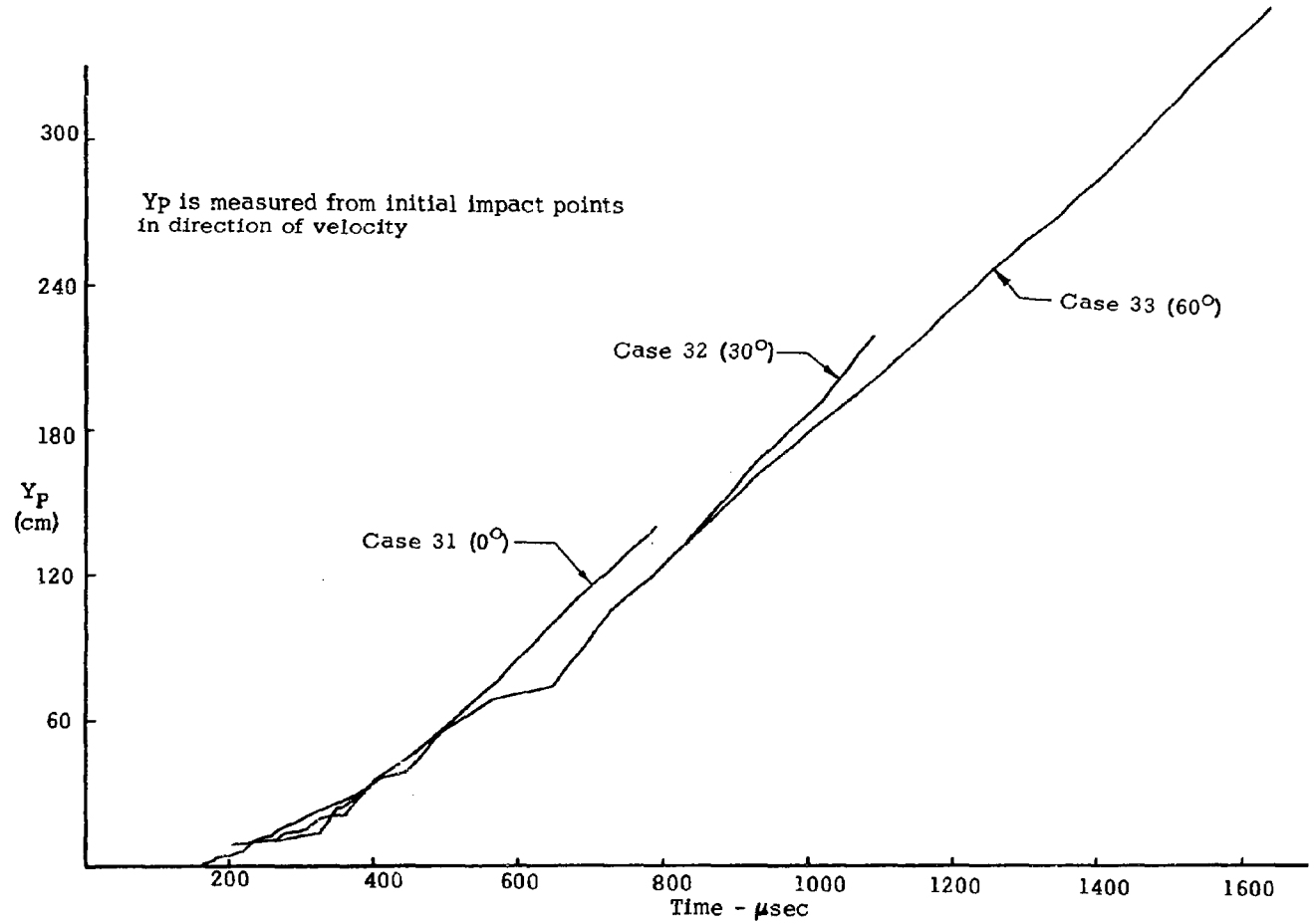

Figure 3-7 Penetration Depth vs Time from Planar Solutions of Normal, 30°, and 60° Rod Impacts (Cases 31, 32, and 33) at 4.6 km/sec

3.3.1 Transient Term

As seen in Figure 3-7, impact obliquity does not significantly affect the duration of the transient stage in planar solutions. Thus for 30°, 60°, and normal incidence, τ_{PL} = 275 μsec, and, using eqn. (3-1), τ_{3D} = 200 μsec. We conclude that the transient term $V\tau/D$ in eqn. (2-13) is independent of obliquity angle, at least for values up to 60°.

3.3.2 Steady State Term

Figure 3-7 also shows that the steady state rate of hole growth is independent of obliquity. However, in oblique impacts, the effective thickness of the target is increased as depicted in the following sketch.

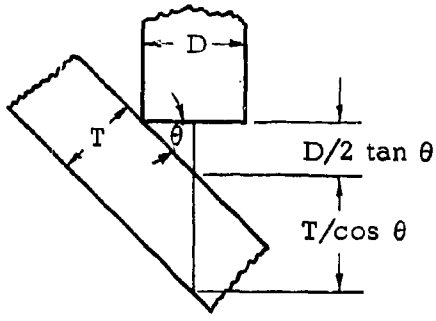

This effective thickness should therefore be substituted in eqn. (2-13). Thus

$$\frac{\Delta L}{D} = \frac{T/D}{\cos\theta} + \frac{1}{2}\tan\theta + \frac{V\tau}{D} \qquad (3\text{-}2)$$

3.4 EXPERIMENTAL COMPARISON (Confidential)

Only a very small amount of experimental data exist for 30° and 60° obliquity impacts for cases where the T/D ratio is two or greater. Two such points are shown in Figure 3-8, along with straight lines representing eqn. (3-2).

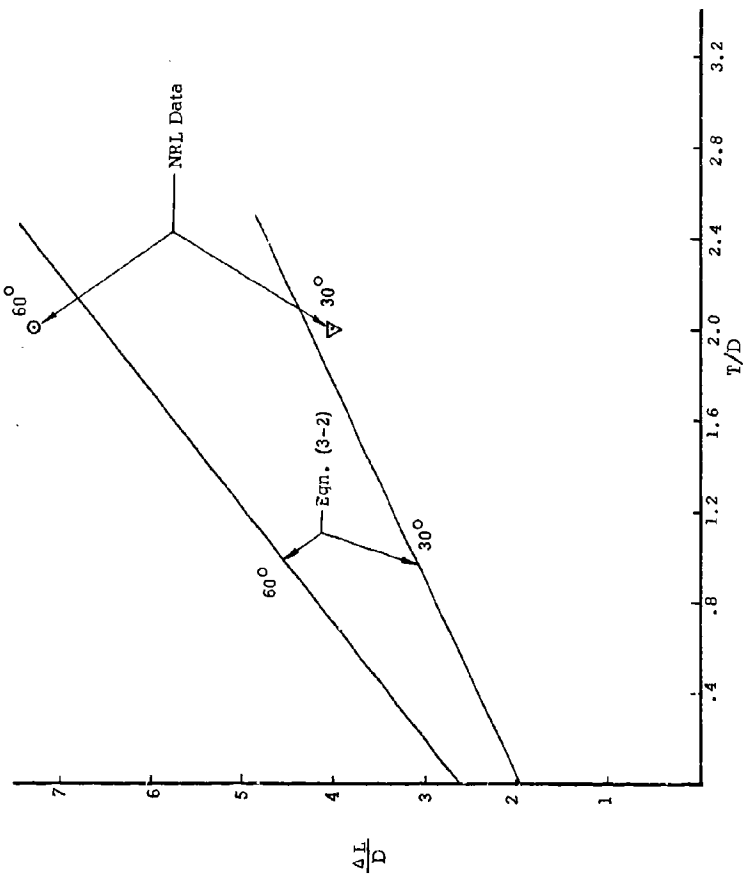

Figure 3-8 Comparison of Rod Loss Equation with Experimental Data for Oblique Incidence of Aluminum Impacts into Aluminum at 4.6 km/sec

4. HOLLOW ROD IMPACTS

The same mechanisms which have been described for solid rod impacts occur in hollow rod cases, and the same three phases of impact are present. The hollow geometry modifies the relative importance of these mechanisms and the duration of the phases, and also introduces at least one new mechanism. These differences are outlined in the following section, and their effects are incorporated into the rod loss relationship.

4.1 COMPARISON OF MECHANISMS

In the end-on impact of either a solid or hollow rod into a finite target, the pressures produced at the solid-solid interfaces are as predicted by the usual Hugoniot jump conditions. Where the impacting surfaces are flat, the initial shock systems in either case are one-dimensional until the effects of lateral free surfaces are felt. With a solid rod, the active free surfaces are the adjacent front of the target, and the sides of the rod projectile. With hollow rods, the inner surface of the projectile, as well as the target surface in the center of the impacting hollow rod, are also sources of pressure relief. By comparison with solid rods of the same diameter or mass per unit length, the distances which rarefaction waves must travel to engulf the 1-d region are always shorter in hollow rods. As a consequence, the duration of the initial transient stage is of shorter duration.

Initially the shock system and mass flow resulting from the impact of the wall of a hollow rod are essentially identical to those which are produced by edge-on impact of a flat plate. This is seen in Figure 4-1. The left axis is the axis of symmetry of the hollow rod. Hence the projectile is represented as the cross-section of one side of the wall. At this early stage, the mass positions in the impact region are similar on both the inside and outside of the wall. Subsequently, however, the shocks and mass flow on the inner side of the rod wall converge towards the axis. The results of this convergence begin to become evident in Figure 4-2. The converging ejecta is moving upward in the hollow of the rod at a considerably higher velocity than is the case for the diverging ejecta outside. Shock pressures along the axis are in excess of 700 kb (approximately as high as the original impact pressure).

This extreme pressure is relieved by rarefactions from the free surface at the axis, causing upward acceleration of target material along the axis. This counterflowing mass has relatively low density, but its velocity is of the same magnitude as the impact speed.

Once the elevated pressures reach the rear free surface, that surface is of course also accelerated. Along the axis, mass is thus flowing both upward and downward. At early times, we therefore find that densities are low along the axis.

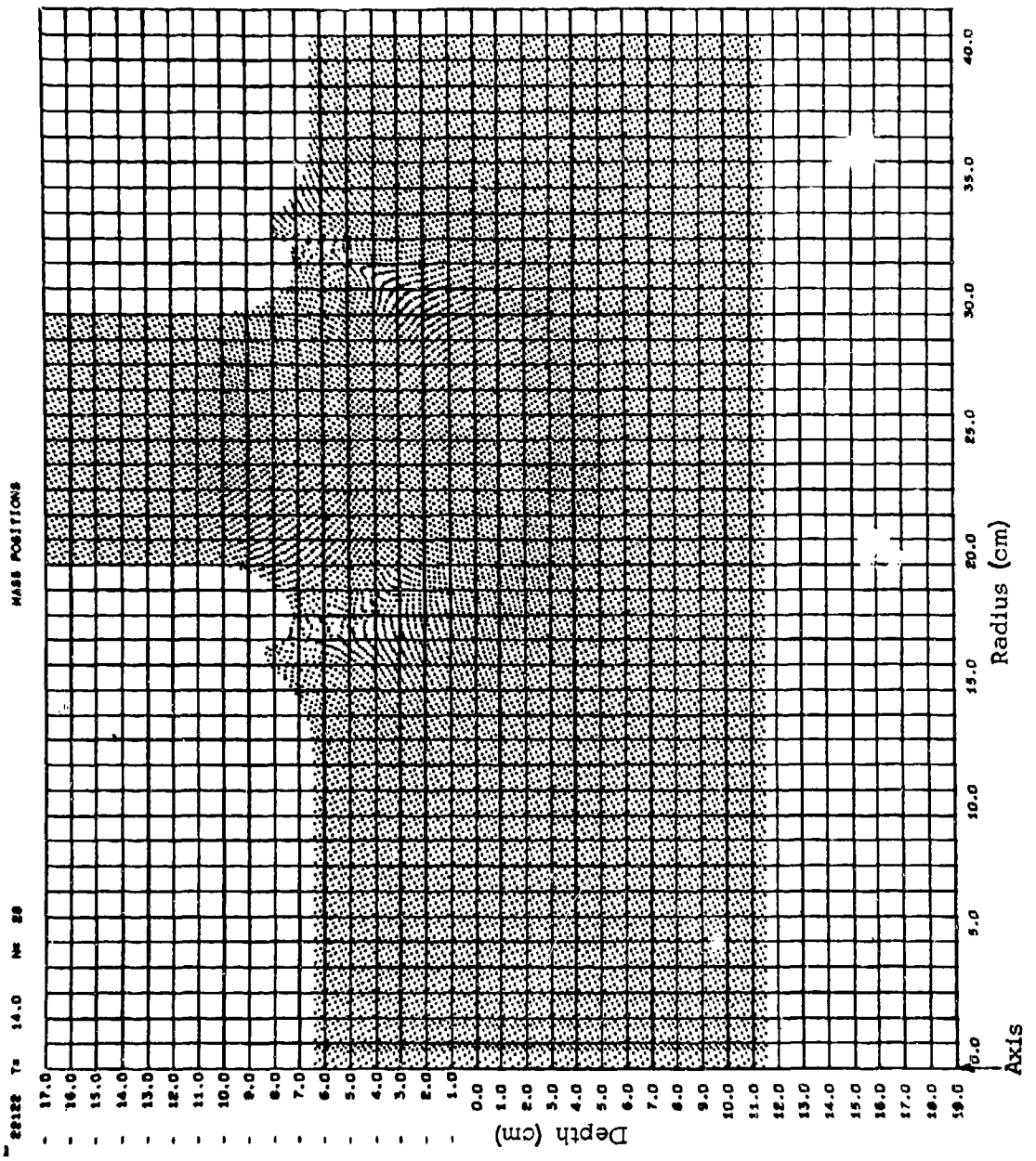

Figure 4-1 Hollow Aluminum Rod Impact
At 4.6 km/sec into Aluminum
At t = 14.0 μsec

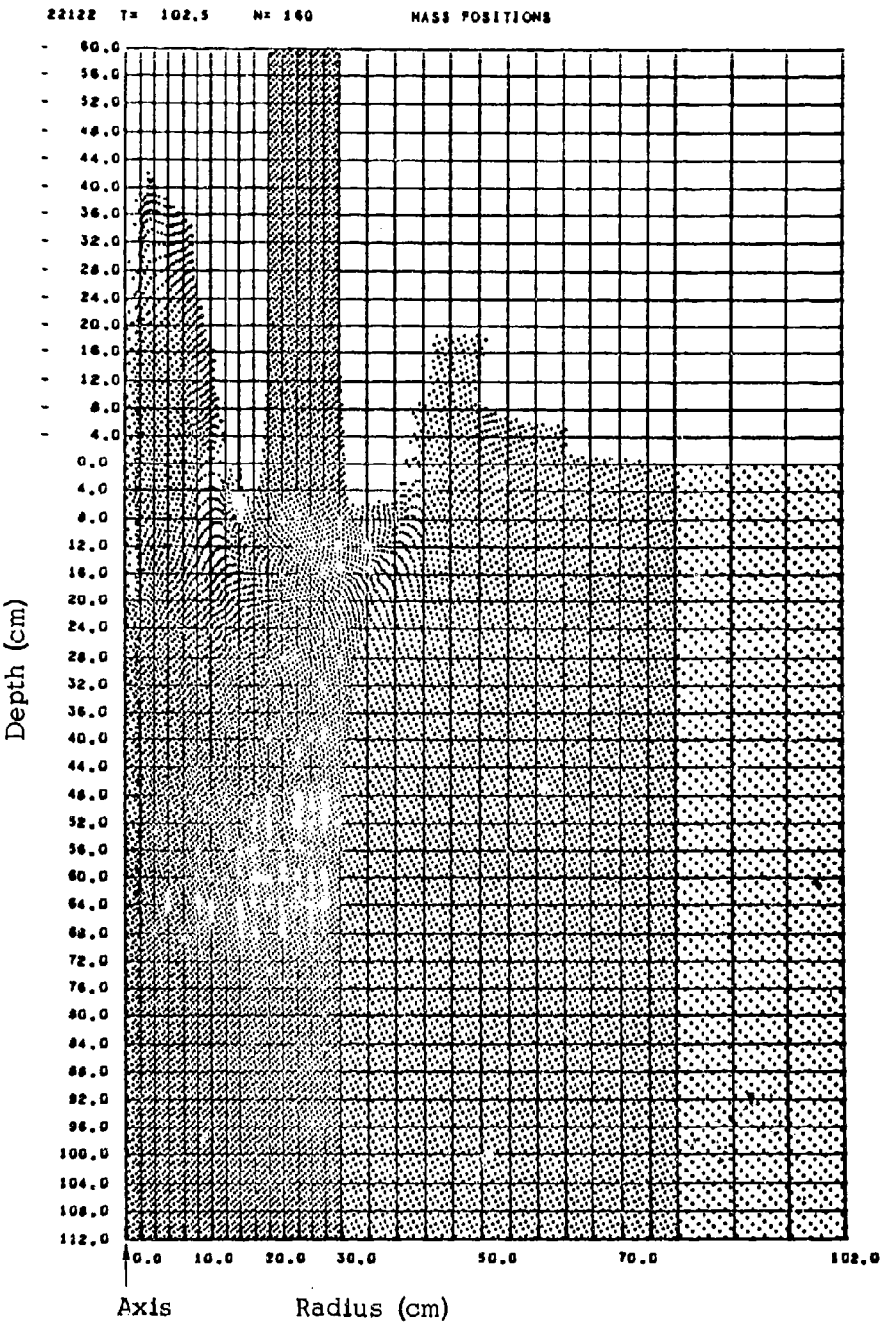

Figure 4-2 Hollow Aluminum Rod Impact
At 4.6 km/sec into Aluminum
At 102.5 μsec

Following the initial transient phase, the flow in hollow rod impacts enters the quasi-steady state phase. The steady state velocity V_∞ will be the same as in solid rod or planar cases, since the steady state equation along a stream line remains the same. Instead of a stagnation point, (as in the axisymmetric case) or a stagnation line (as in the planar case), there is a stagnation "ring".

4.2 MODIFICATION OF ROD LOSS EQUATION FOR HOLLOW RODS

Equation (2-13) gives the basic rod loss relationship for solid rods. For hollow rods, this relationship continues to be valid, except that the time characteristic of the transient stage, τ, will be reduced to reflect the shorter duration of that phase.

Figure 4-3 shows the penetration depth Y_p vs time for two hollow rod solutions (ID/OD = 1/3 and 2/3) and compares these with a corresponding solid rod case. The shorter duration of the initial transient stage is apparent: τ is approximately 125 for both of the hollow rod cases, as compared to 200 for the solid rod. The use of $\tau = 125$ in the exponential eqn. (2-8) for Y_p vs t produces the solid curves, which are seen to be good fits of the numerical points. (Slightly larger values of τ would be expected for the ID/OD = 1/3 case than for ID/OD = 2/3, but no significant difference is apparent from the Y_p vs t plots).

The $V\tau/D$ term in eqn. (2-13) for the hollow aluminum rods impacting at 4.6 km/sec is therefore 0.95. By comparison, the $V\tau/D$ term for solid rods at this velocity is 1.5. Hence the hollow rods will be more efficient by approximately 0.5 D. That is, a greater portion of the length of a hollow rod will remain after the transient phase is completed than will be the case for a solid rod of the same diameter (or mass per unit length). The rod loss during steady state penetration will be identical for hollow and solid rods.

4.3 DISSIMILAR HOLLOW ROD IMPACTS

One numerical solution considered the impact of a hollow steel rod into a T/D = 2 aluminum target. The results are chiefly of interest in confirming the applicability to dissimilar material impacts of the rod loss equations developed in Section 2.2.

Figure 4-4 shows the Y_p vs t data obtained from the numerical solution. The data have been fitted with eqn. (2-9), using values of V_∞, the stagnation point velocity, which from eqn. (2-6) is

$$V_\infty = \frac{V}{1 + \sqrt{\rho_T/\rho_p}} = \frac{4.6}{1.59} = 2.9 \qquad (4\text{-}1)$$

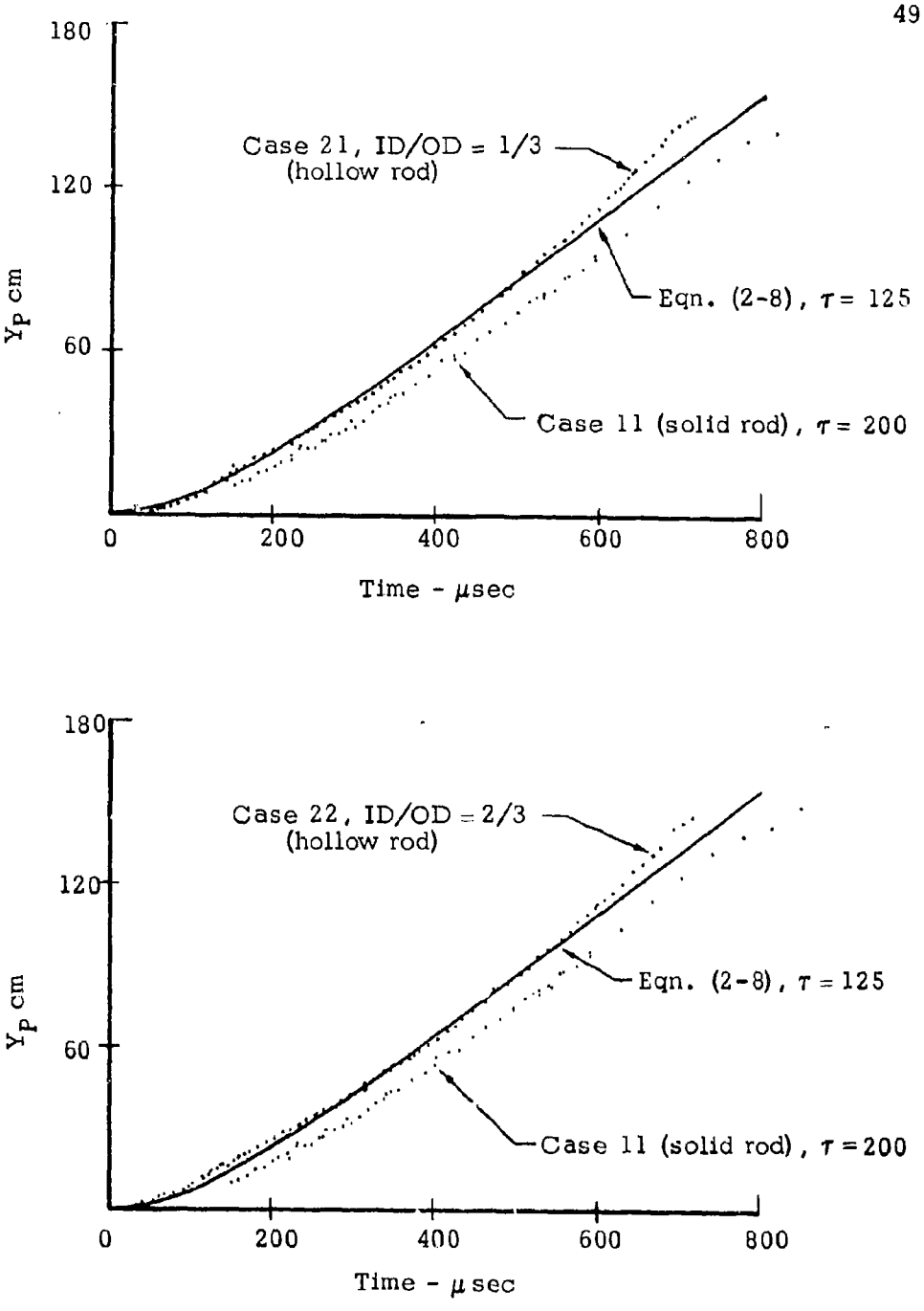

FIGURE 4-3 Penetration Depth vs Time For Hollow Aluminum Rod Impacts at 4.6 km/sec

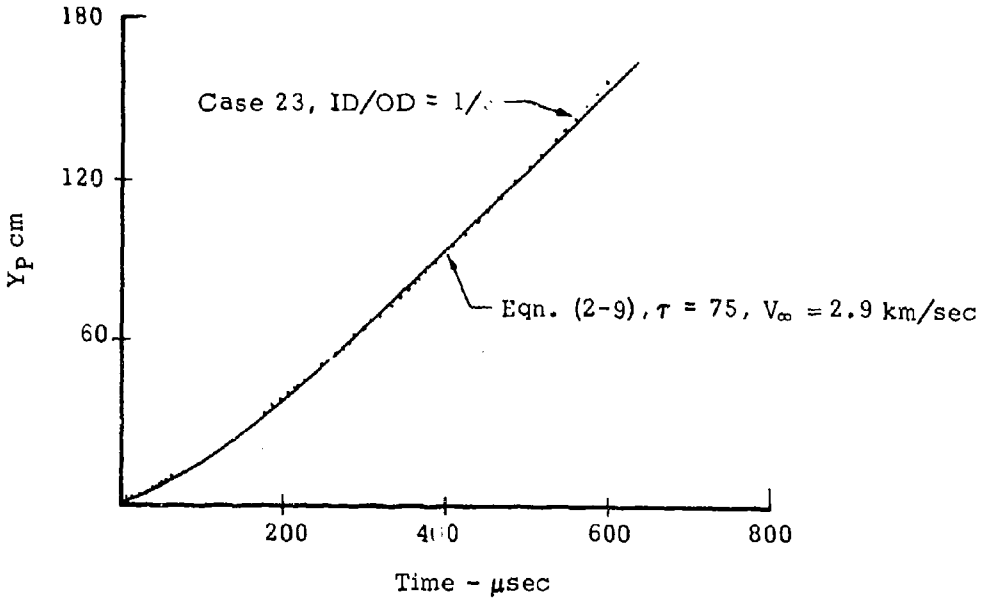

FIGURE 4-4 Penetration Depth vs Time For Hollow Iron Rod Impact into Aluminum at 4.6 km/sec, Target Thickness/ Rod Diameter = 2.

impacts by

$$\tau_{P\to T} = \tau_{T\to T}\sqrt{\frac{\rho_T}{\rho_p}} = 125 \times .6 = 75 \qquad (4\text{-}2)$$

The fit which is obtained using these values in eqn. (2-9) is seen to be excellent.

REFERENCES

1. R. L. Bjork, et al. (Shock Hydrodynamics, Inc.) "Hypervelocity Impact of End-Oriented Rods," NRL Report 6310, April 1965.

2. K. N. Kreyenhagen, et al. (Shock Hydrodynamics, Inc.) "The SHAPE Code" Hardening Technology Studies, Volume V, Part 2, Appendix 5D, Lockheed Missiles and Space Company Report LMSC-B130200, September 1965.

3. H. E. Read, (Shock Hydrodynamics, Inc.) "STRIDE, A Three-Dimensional Code", Hardening Technology Studies-II, Lockheed Missiles and Space Company Report LMSC-D000017, August 1967.

4. L. V. Al'tshuler, et al. "The Isentropic Compressibility of Aluminum, Copper, Lead, and Iron at High Pressures," Soviet Physics JETP, Vol. 11, No. 4, Pg. 766, October 1960.

5. M. H. Rice, J. M. Walsh, and R. G. McQueen, "Compression of Solids by Strong Shock Waves," Solid State Physics, Volume 6, pg. 1, 1958.

6. A. H. Jones, J. F. Polhemus, and W. Herrmann, "Survey of Hypervelocity Impact Information II," MIT Aeroelastic and Structures Research Laboratory Report A.S.R.L. 99-2, December 1963.

APPENDIX A

SPATIAL PLOTS FROM NUMERICAL SOLUTIONS

The two-dimensional hydrodynamic PIC code was used for all of the impact solutions obtained in this investigation. The problems were run on the IBM 7094 computer at Eglin AFB, Florida. For ease of interpretation, the computer output can be obtained in the form of visual displays of spatial plots by use of the SC4020 plotter. Three types of spatial plots are generally called for - showing mass positions, velocity fields, and pressure fields at selected times. Mass position plots indicate the material disposition by arrangements of dots representing masses. Velocity fields show average particle velocities for the mass points in each cell by means of vectors originating at the cell centers. Pressure fields are shown by constant pressure contours (isobars). In this appendix, the development of the impact solutions are illustrated by sequences of the mass position and velocity field plots.

Figures 1-1 and 1-2 of the text summarize the impact cases which have been considered during the study. Spatial plots for cases 1-8 are given in Appendix I of reference 1. Up until the time that the initial shock in a given rod and velocity case reaches the rear surface of a thin target, the solution is identical to an impact on any thicker target. Wherever possible, thicker target solutions in this investigation have hence been "built" upon early stage solutions for thinner targets. Thus in the sequence of impact cases where different thicknesses of targets were considered (i.e. T/D = 1/4, 1/2, 1, 2, 3, 5) the initial conditions for the T/D = 1/2 solution were obtained from the T/D = 1/4 solution at a point just before the shock in the target had reached the rear surface of the T/D = 1/4 plate. Similarly the T/D = 1 solution was started using conditions from the T/D = 1/2 problem just before the shock reached the T/D = 1/2 rear surface.

IMPACT CASE A1: Aluminum Rod vs Aluminum Target
Normal Impact at 4.0 km/sec,
Rod Dia. = 60 cm, Target
Thickness = 180 cm (T/D = 3)

Figure A1 (facing) Initial Conditions

The upper plot illustrates the initial disposition of the mass points in the computational grid, while the lower plot shows the initial velocity field at the instant of impact. In these plots the left ordinate is the axis of symmetry and the line, y = 0, corresponds to the initial interface between rod and target material. Equivalent solutions are obtained either by moving the rod towards the target, or by moving the target towards the rod.

To optimize the resolution obtained in the solutions, those portions of the rod and target materials which are remote from the impact, and which are hence not yet active in the impact process, are not included in the field of view. The rod itself is always shown foreshortened, with new length being added as it advances into the target plate.

Hydrodynamic solutions can be linearly scaled, hence the only important quantity in Figure A1 is the ratio between target thickness and rod radius. For convenience, these problems were set up using 60-cm diameter rods. The results can be scaled to any other size by multiplying all lengths and times by the same factor. To convert to 0.125 in.-diameter rods, one need only multiply all lengths and times by 2.54/(60)(8) = 0.00529166 . . . . This treatment does not alter the thermodynamic and mechanical variables necessary to describe the results.

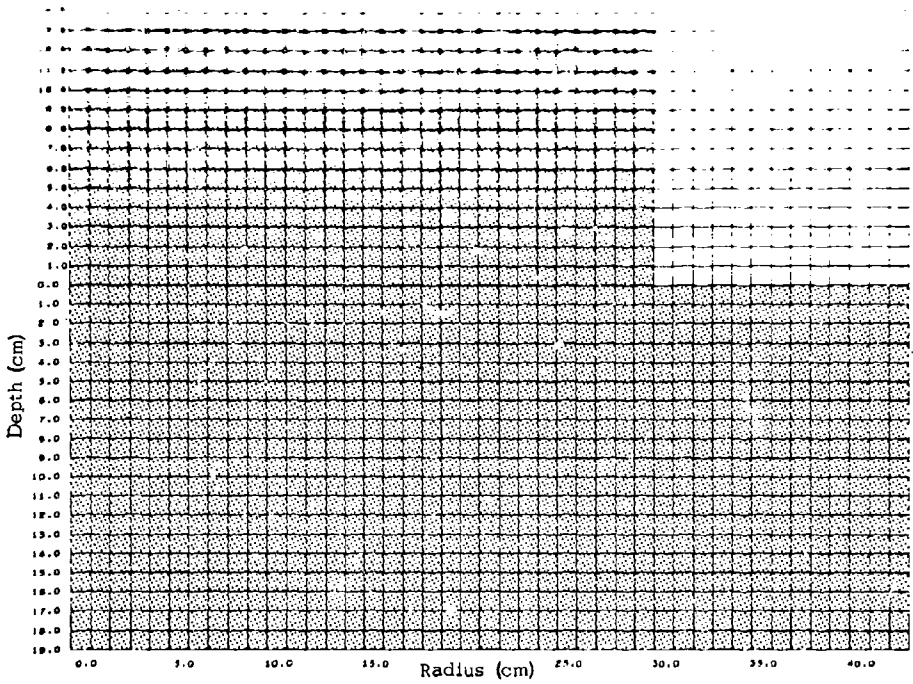
Depth (cm)
Radius (cm)

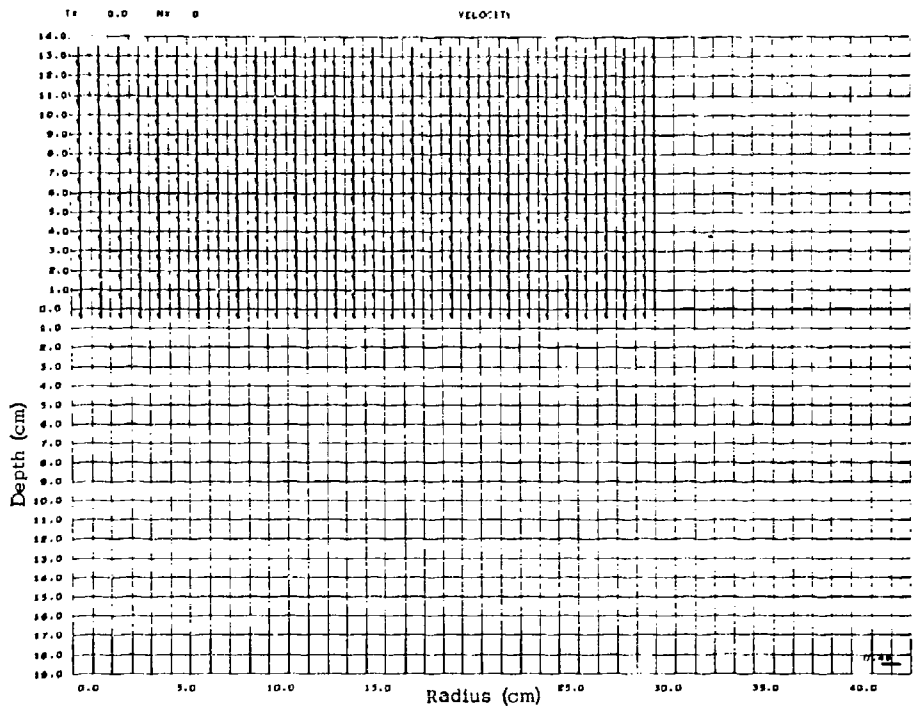
VELOCITY
Depth (cm)
Radius (cm)

IMPACT CASE 11: Al vs Al @ 4.6 km/sec, T/D = 3

Figure A2 (facing): Velocity Fields at 5.7 and 10.7 μsec

These plots, as well as those in Figures A3 - A6 which follow, are taken from the T/D = $\frac{1}{4}$, $\frac{1}{2}$, 1, and 2 solutions in Reference 1. They are included here to provide the "built-up" basis for the continuing solutions of the T/D = 3, 5 impacts.

The early stages of the flow field are seen in Figure A2.

Initially, most of the field is one-dimensional, with shocks propagating in opposite directions from the original interface. Between the diverging shocks is a constant state region moving at half the impact velocity. Pressure relief, in the form of a rarefaction fan, propagates into the high pressure region from the free surfaces. This rarefaction system eventually destroys the one-dimensional nature of the initial flow.

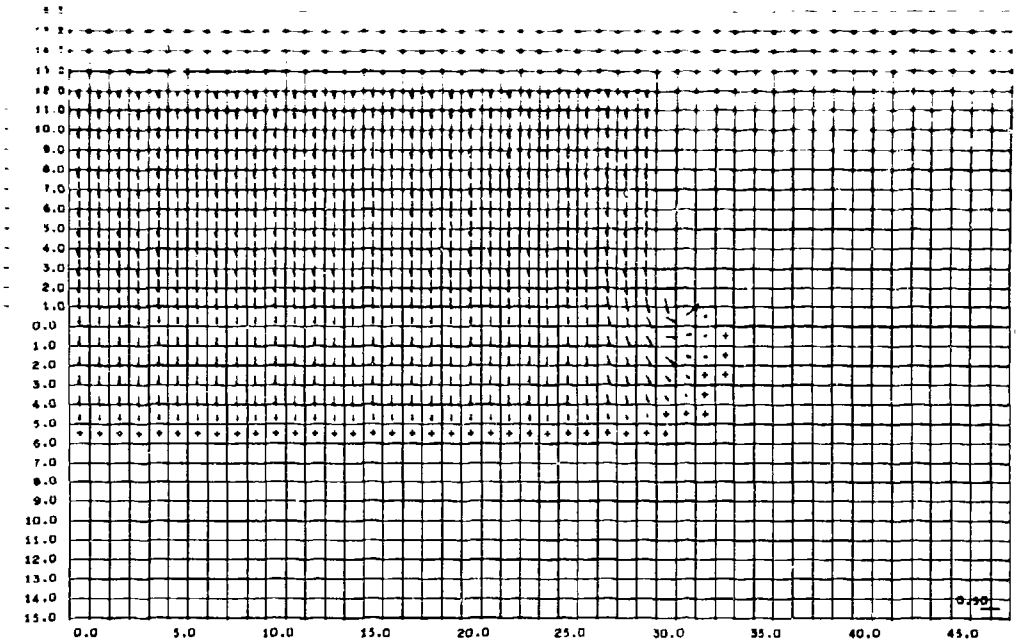

22101 T= 10.7 N= 40 VELOCITY

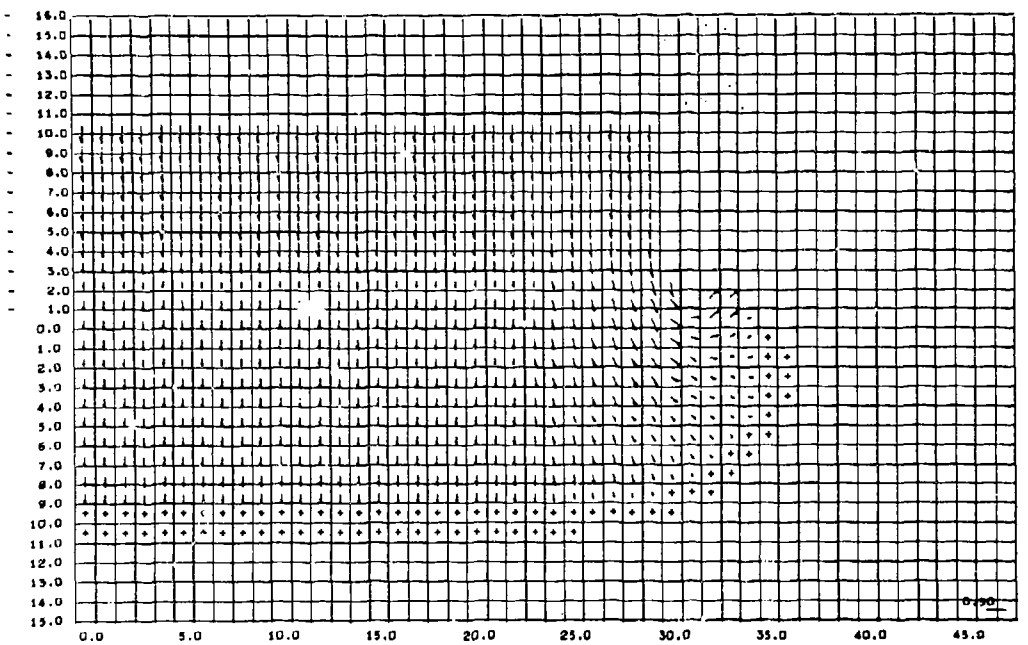

IMPACT CASE 11: Al vs Al @ 4.0 km/sec, T/D = 3

Figure A3 (facing): Velocity Fields at 16.2 and 26.2 μsec

These plots show the continuing development of the velocity field. The particle velocities flowing radially into the target material interact with the front surface to cause upward flow — the front surface splash which is experimentally observed in impacts.

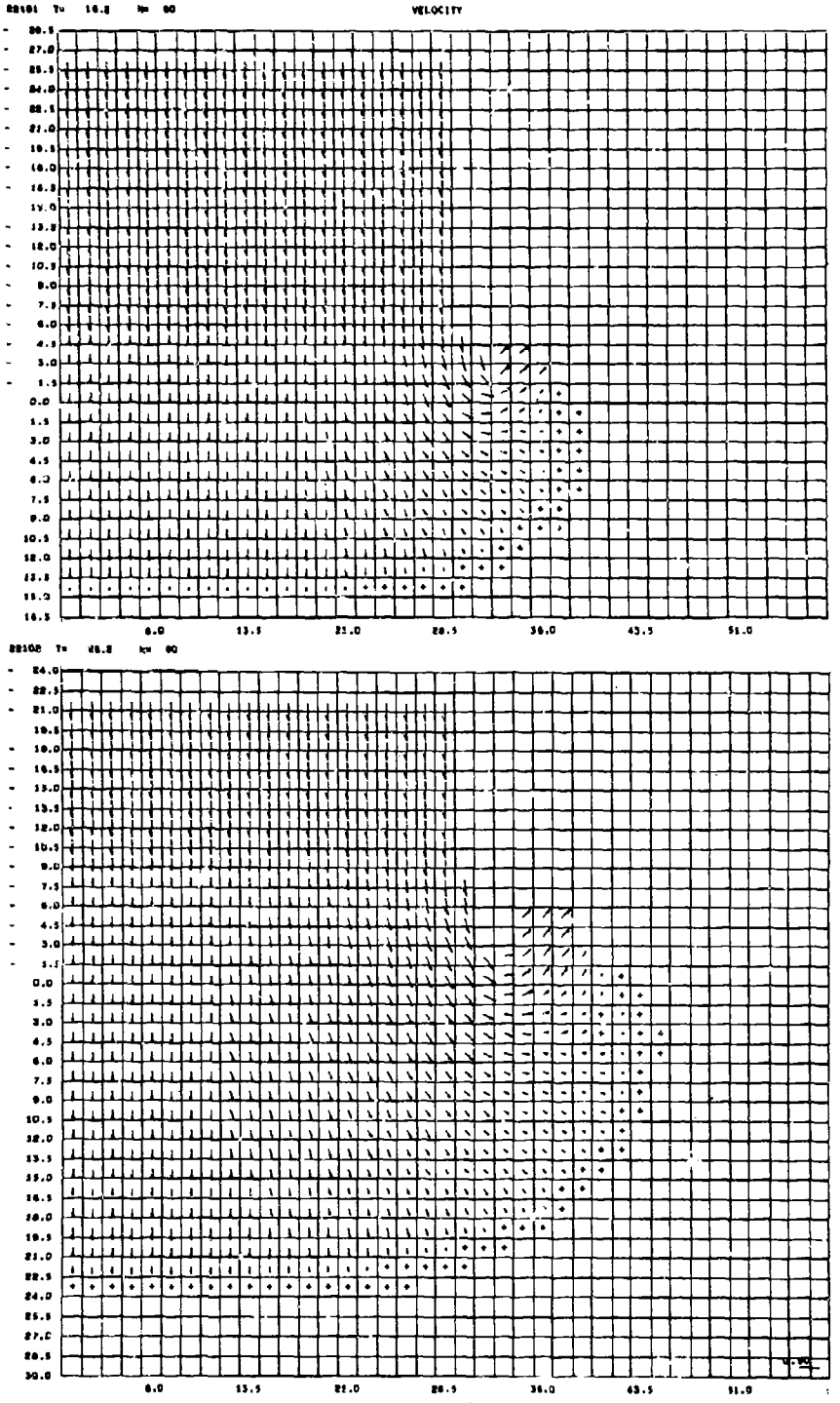
VELOCITY
0.0
13.5
22.0
28.5
36.0
43.5
51.0

IMPACT CASE 11: Al vs Al @ 4.6 km/sec, T/D = 3

Figure A4 (facing): Velocity Fields at 36.2 and 46.2 μ sec

A grid change has enlarged the field of view for these plots (as compared with Figure A3). The lateral rarefaction system reaches the axis at about 36 μsec, and the velocity field thereafter is substantially two-dimensional.

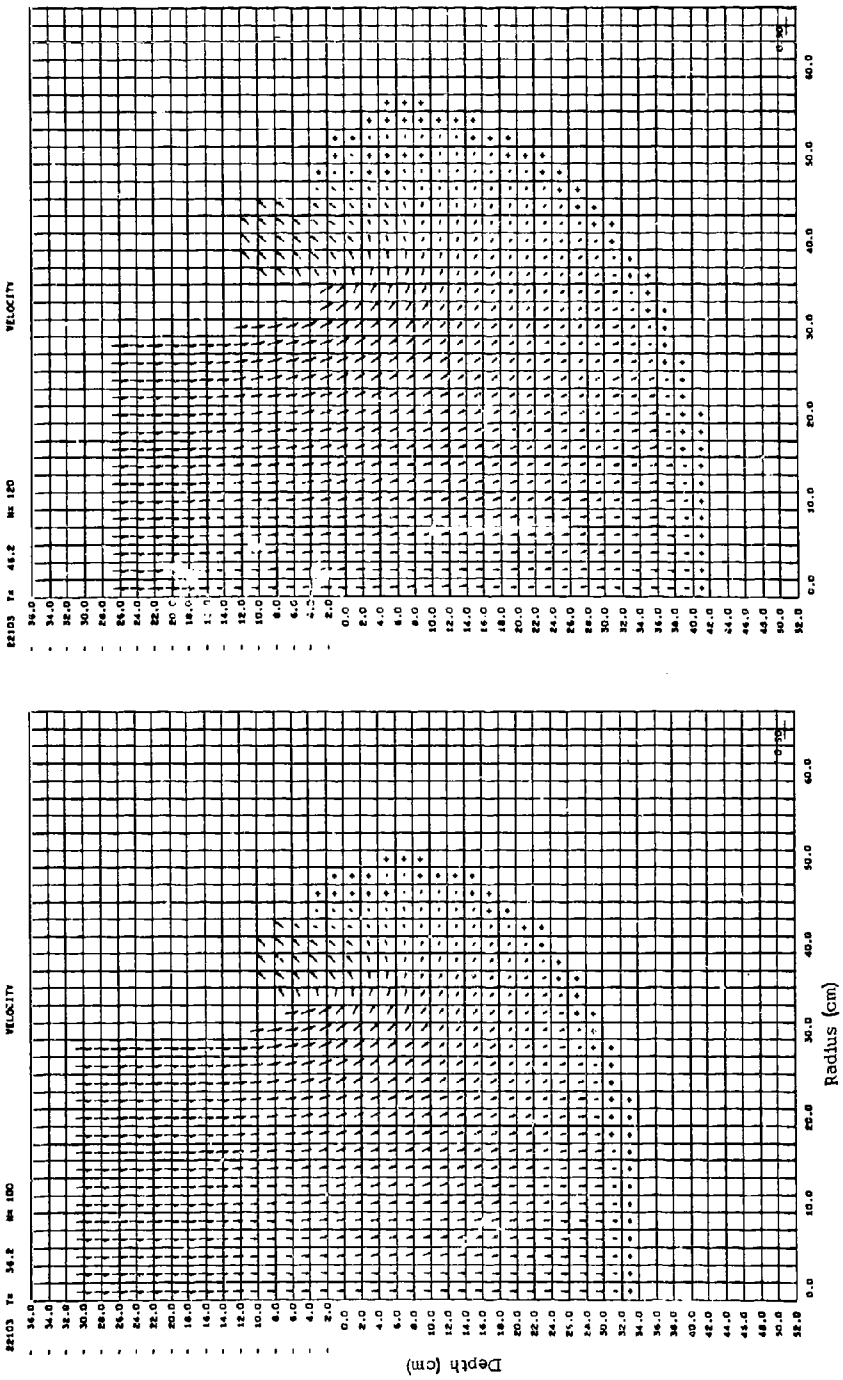
VELOCITY
VELOCITY
Depth (cm)
Radius (cm)

IMPACT CASE 11: Al vs Al @ 4.6 km/sec, T/D = 3

Figure A5 (facing): Velocity Fields at 56.2 and 81.2 μsec

A grid change is again used to enlarge the field of view. By 81.2μsec the velocity field is essentially hemispherical.

These solutions assume that the rod is ten diameters in length, such that the back end of the rod is never active in the impact response. During the course of the solutions, most of the inactive portion of the rod is not included. As the region of activity spreads upward in the rod, additional material is added from time to time.

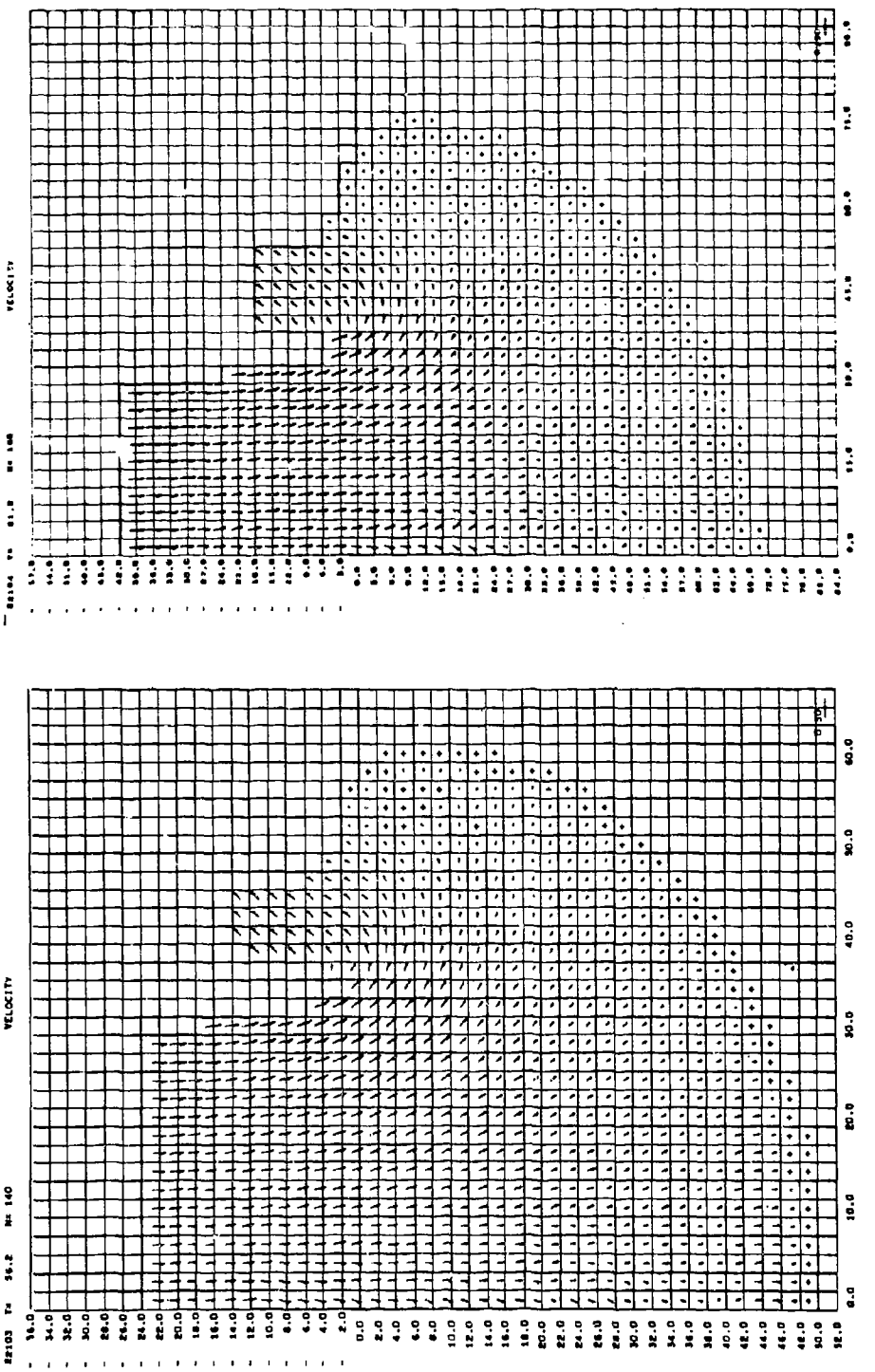
VELOCITY
VELOCITY

IMPACT CASE 11: Al vs Al @ 4.6 km/sec, T/D = 3

Figure A6 (facing): Mass Positions and Velocity Field at 111.2 μsec

The darker region near the axis in the mass position plot is caused by use of a larger number of mass points to provide better resolution in this region.

By 111 μsec, the shock in the target has reached a depth and lateral extent of 90 cm. The higher density of material behind the shock is evident in the mass plot.

An open hole (void) extending below the original surface has begun to form at this time at a radius of about 40 cm.

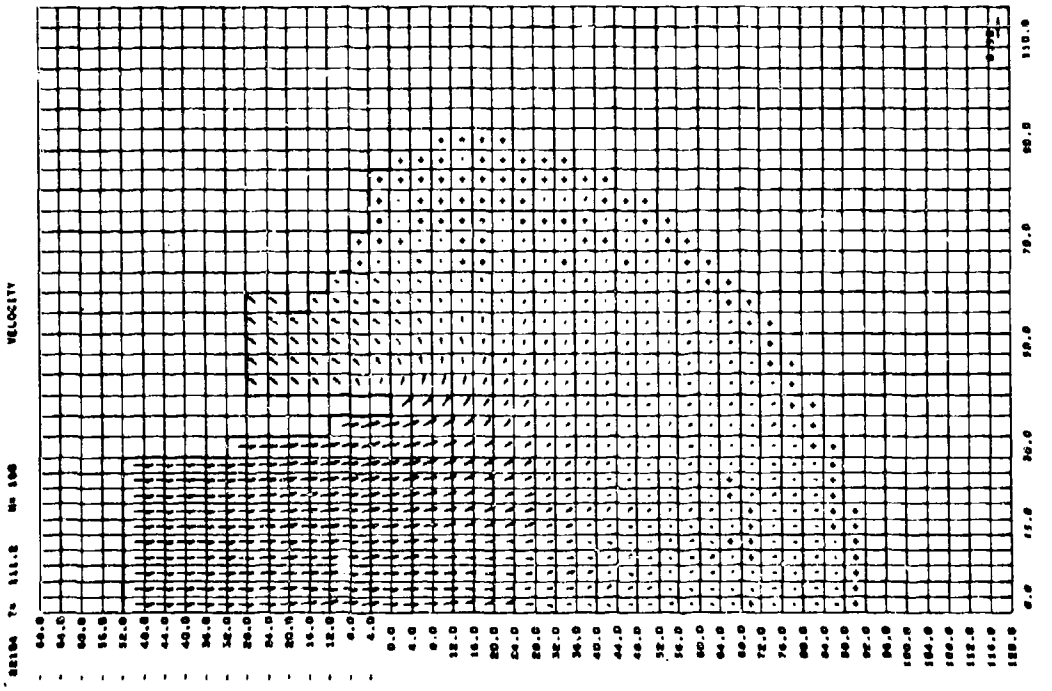
VELOCITY

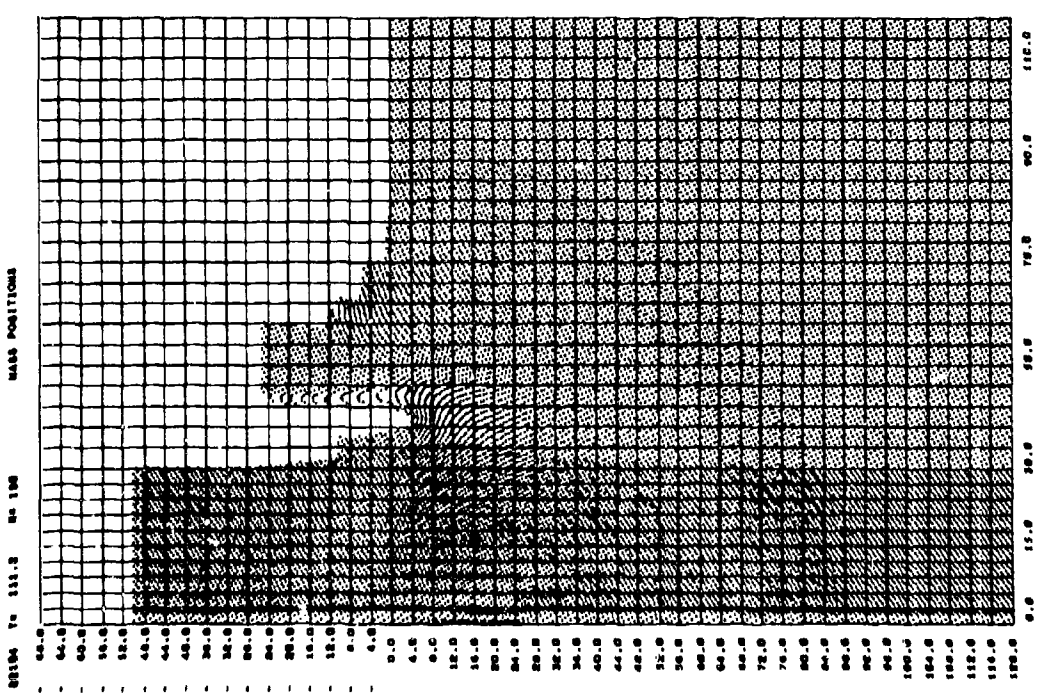
MASS POSITIONS

IMPACT CASE 11: Al vs Al @ 4.6 km/sec, T/D = 3

Figure A7 (facing): Mass Positions and Velocity Fields at 202.3 and 422.9 μsec.

Shortly before 200 μsec, the shock in the target first reaches the rear free surface at 180 cm depth. Motion along that surface is evident in the plots at 202.3 μsec.

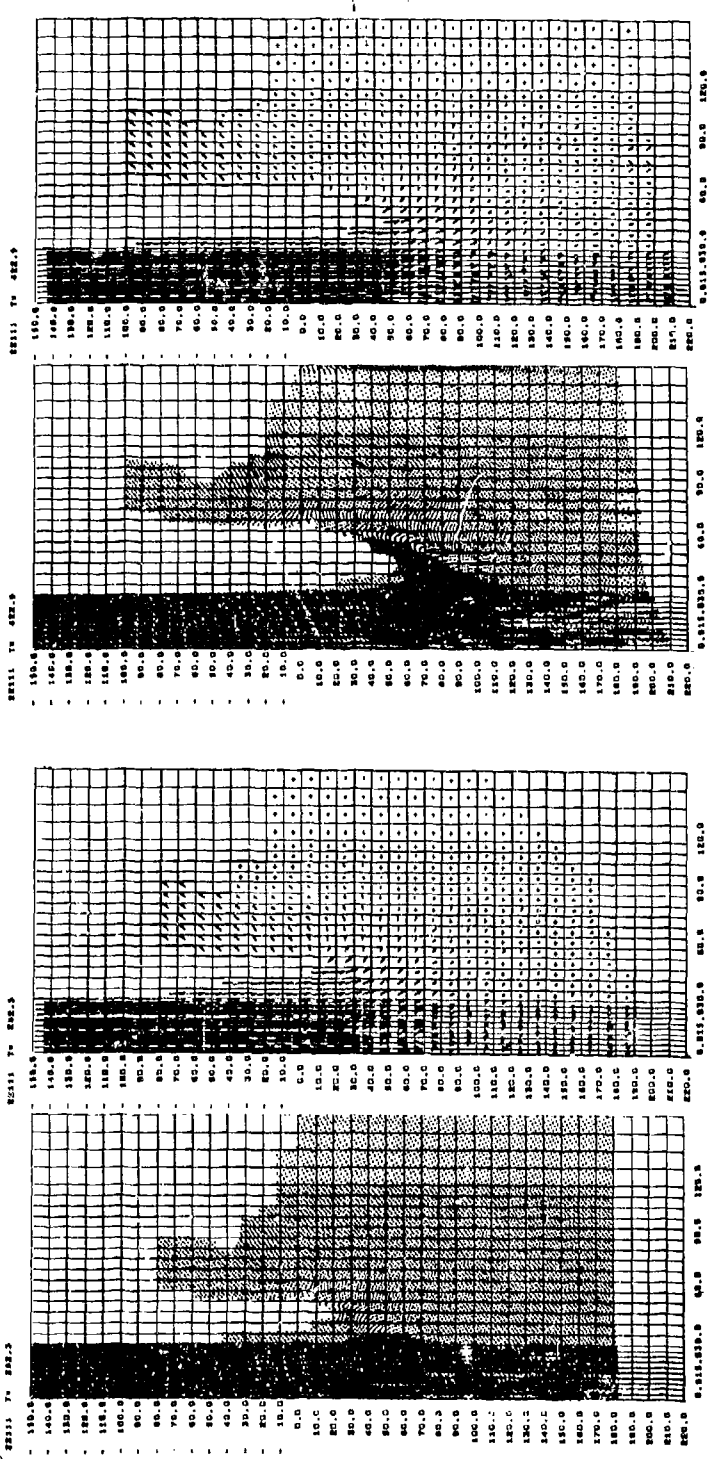

IMPACT CASE 11: Al vs Al @ 4.6 km/sec, T/D = 3

Figure A8 (facing): Mass Positions and Velocity Field @ 580.9 μsec

The open hole continues to form as the tip of the rod advances into the target.

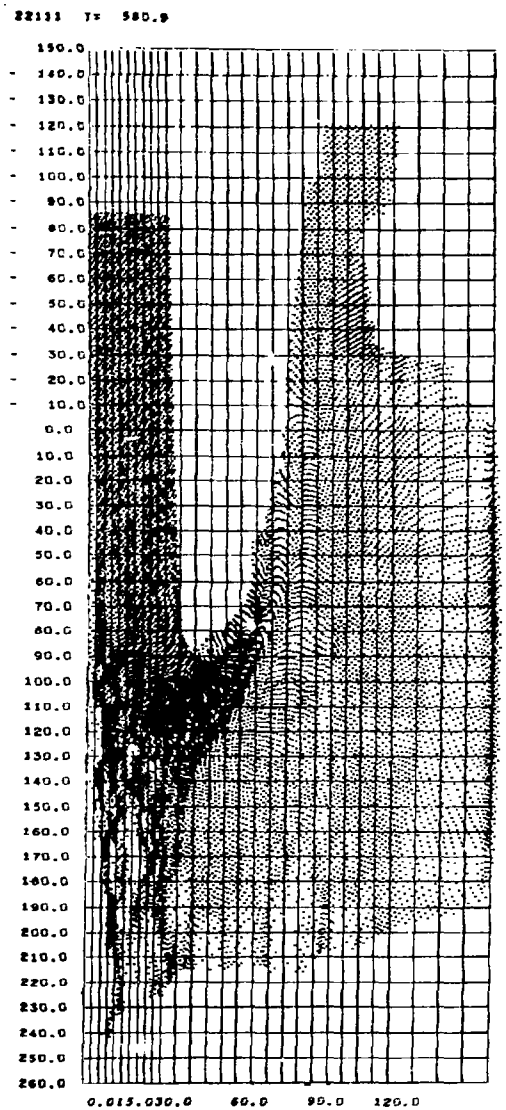
22111 T= 580.0
150.0
140.0
130.0
120.0
110.0
100.0
90.0
80.0
70.0
60.0
50.0
40.0
30.0
20.0
10.0
0.0
10.0
20.0
30.0
40.0
50.0
60.0
70.0
80.0
90.0
100.0
110.0
120.0
130.0
140.0
150.0
160.0
170.0
180.0
190.0
200.0
210.0
220.0
230.0
240.0
250.0
260.0
0.015.030.0 60.0 90.0 120.0

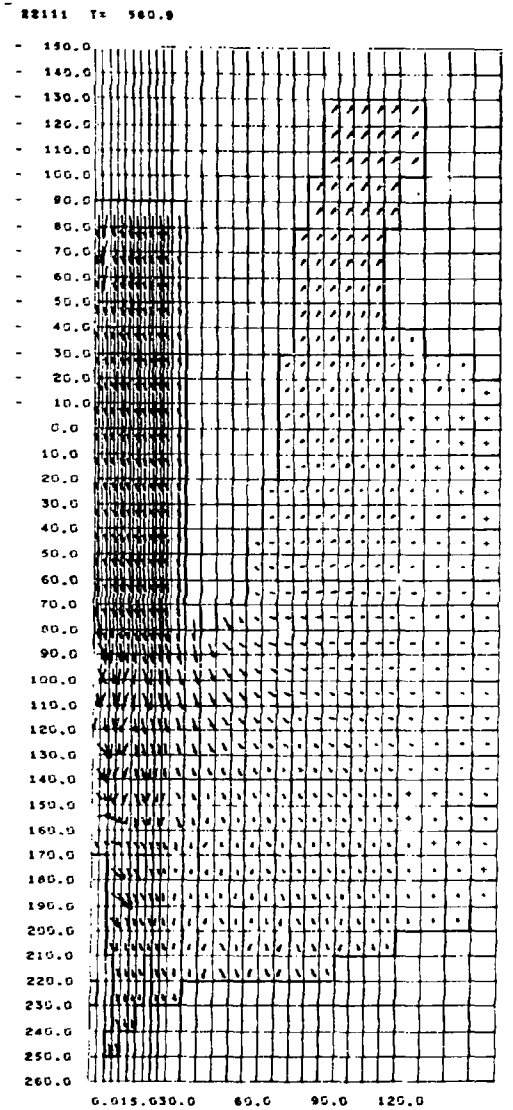
22111 T= 580.0
150.0
140.0
130.0
120.0
110.0
100.0
90.0
80.0
70.0
60.0
50.0
40.0
30.0
20.0
10.0
0.0
10.0
20.0
30.0
40.0
50.0
60.0
70.0
80.0
90.0
100.0
110.0
120.0
130.0
140.0
150.0
160.0
170.0
180.0
190.0
200.0
210.0
220.0
230.0
240.0
250.0
260.0
0.015.030.0 60.0 90.0 120.0

IMPACT CASE 11: Al vs Al @ 4.6 km/sec, T/D = 3

Figure A9 (facing): Mass Positions and Velocity Field @ 708.4 μsec

In the velocity field, (+) indicates a non-zero velocity vector whose magnitude is too small to be plotted.

By 708 μsec, the open hole depth is at about 120 cm. The rod shaft continues to advance into relatively low velocity target material ahead of the tip.

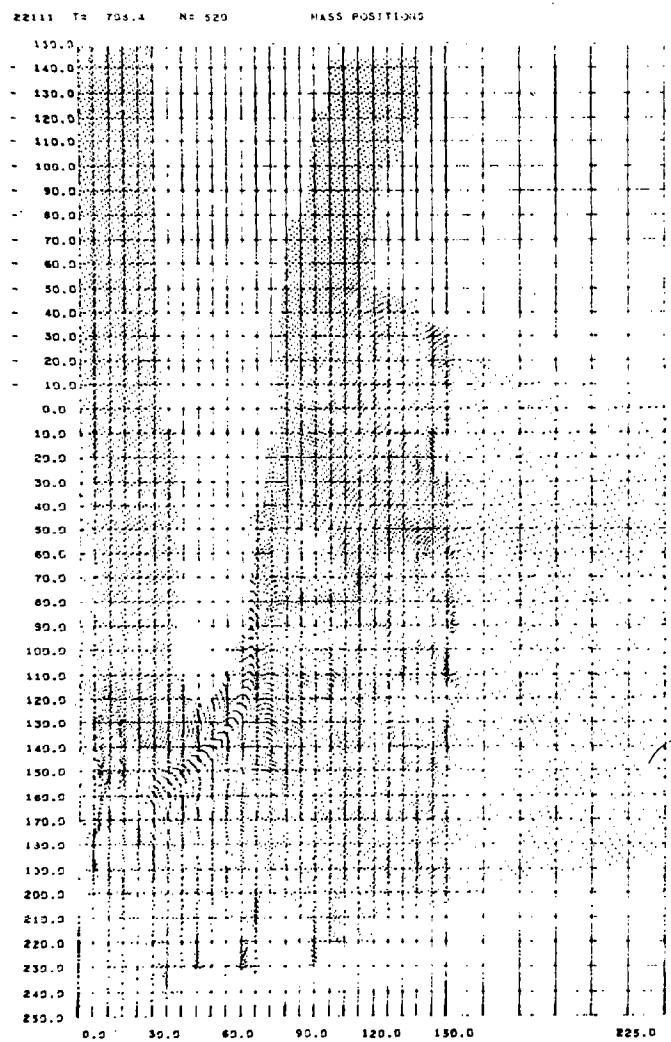
22111 Ts 703.4 Ns 520
MASS POSITIONS
150.0
140.0
130.0
120.0
110.0
100.0
90.0
80.0
70.0
60.0
50.0
40.0
30.0
20.0
10.0
0.0
10.0
20.0
30.0
40.0
50.0
60.0
70.0
80.0
90.0
100.0
110.0
120.0
130.0
140.0
150.0
160.0
170.0
180.0
190.0
200.0
210.0
220.0
230.0
240.0
250.0
0.0
30.0
60.0
90.0
120.0
150.0
225.0

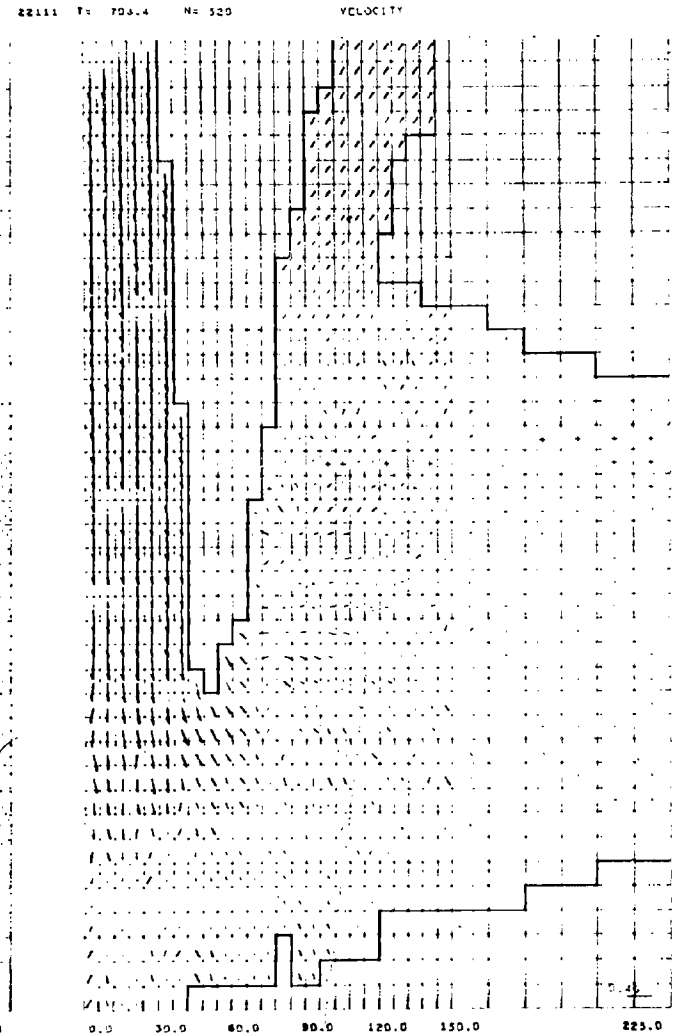
22111 Ts 703.4 Ns 520
VELOCITY
0.0
30.0
60.0
90.0
120.0
150.0
225.0

IMPACT CASE 11: Al vs Al @ 4.6 km/sec, T/D = 3

Figure A10 (facing): Mass Positions and Velocity Field at 857.4 μsec

Instabilities are beginning to appear in the numerical solution by this time, and these have resulted in inward motion of mass from the sides of the open hole. The mass involved is small, however, and it does not have a strong effect on the continuing solution.

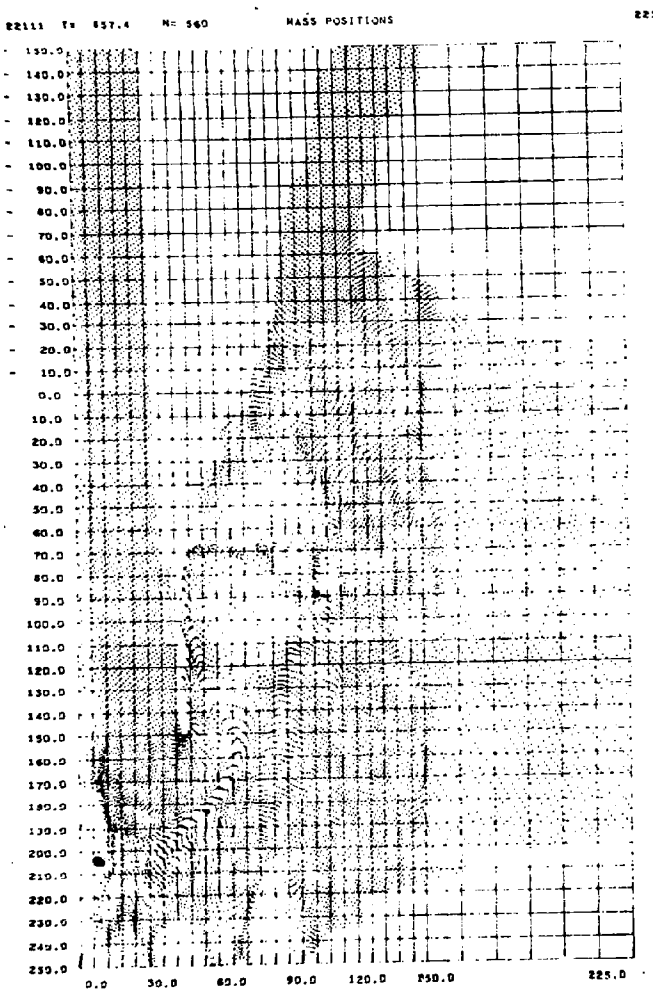
22111 T= 857.4 N= 560
MASS POSITIONS
150.0
140.0
130.0
120.0
110.0
100.0
90.0
80.0
70.0
60.0
50.0
40.0
30.0
20.0
10.0
0.0
10.0
20.0
30.0
40.0
50.0
60.0
70.0
80.0
90.0
100.0
110.0
120.0
130.0
140.0
150.0
160.0
170.0
180.0
190.0
200.0
210.0
220.0
230.0
240.0
250.0
0.0
30.0
60.0
90.0
120.0
150.0
225.0

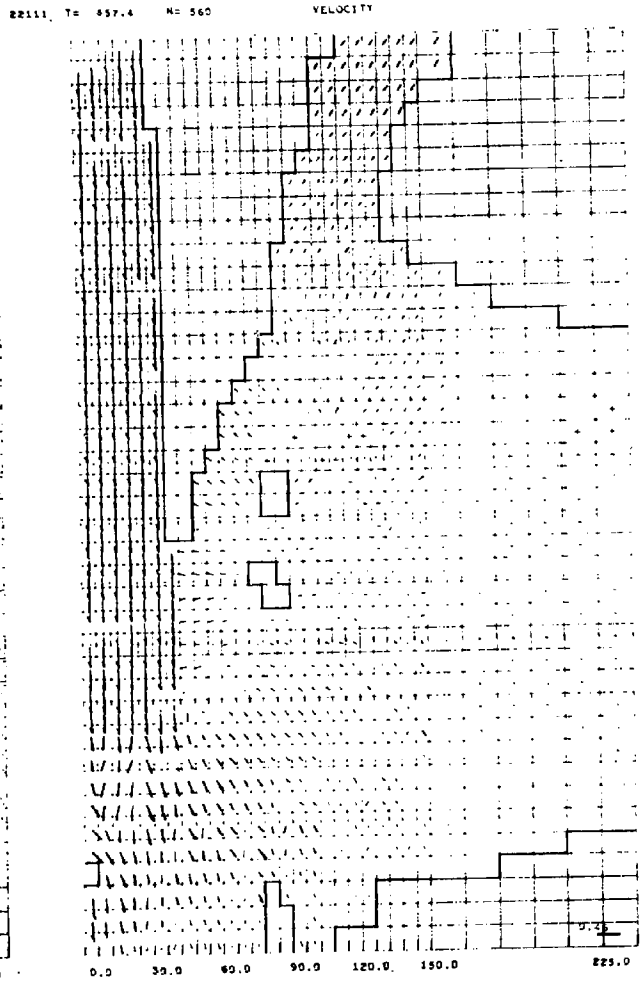
22111 T= 857.4 N= 560
VELOCITY
0.0
30.0
60.0
90.0
120.0
150.0
225.0

IMPACT CASE 11: Al vs Al @ 4.6 km/sec, T/D = 3

Figure A11 (facing): Mass Positions and Velocity Field at 1006.4 μsec

These are the final plots from Case 11. The open hole has reached the depth (180 cm) of the original rear surface of the target, which is the point at which the quasi-steady state flow is assumed to terminate. By this time, the remaining material ahead of the rod has been accelerated to nearly the impact velocity, so that additional rod loss will not be large.

Instabilities have obscured some of the details of the hole formation but the general features of the flow at this time are evident.

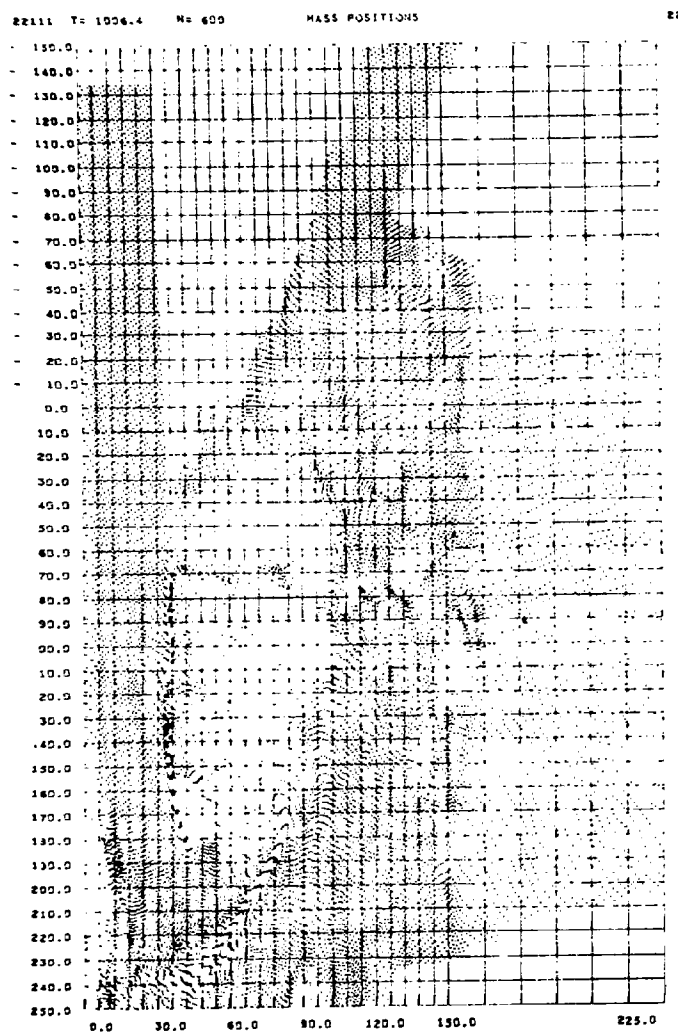
22111 T= 1006.4 N= 600
MASS POSITIONS
150.0
140.0
130.0
120.0
110.0
100.0
90.0
80.0
70.0
60.0
50.0
40.0
30.0
20.0
10.0
0.0
10.0
20.0
30.0
40.0
50.0
60.0
70.0
80.0
90.0
100.0
110.0
120.0
130.0
140.0
150.0
160.0
170.0
180.0
190.0
200.0
210.0
220.0
230.0
240.0
250.0
0.0
30.0
60.0
90.0
120.0
150.0
225.0

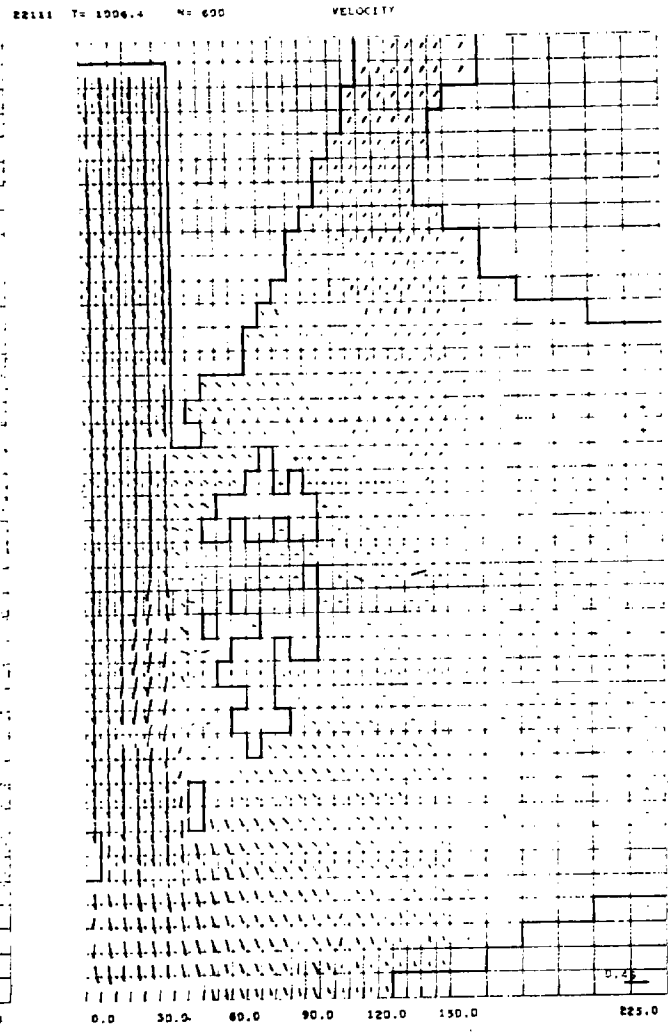
22111 T= 1006.4 N= 600
VELOCITY
0.0
30.0
60.0
90.0
120.0
150.0
225.0

IMPACT CASE 12: Aluminum Rod vs Aluminum Plate, Normal Impact at 4.6 km/sec. Rod Diameter = 60 cm, Target Thickness = 300 cm (T/D = 5)

Figure A12 (facing): Mass Positions and Velocity Field at 297.9 μsec

The solution for Case 12 was started using the conditions generated by the Case 11 (T/D = 3) solution just before the shock had reached the rear surface at 180 cm (at about 200 μsec). Additional target mass was added to increase the thickness to 300 cm.

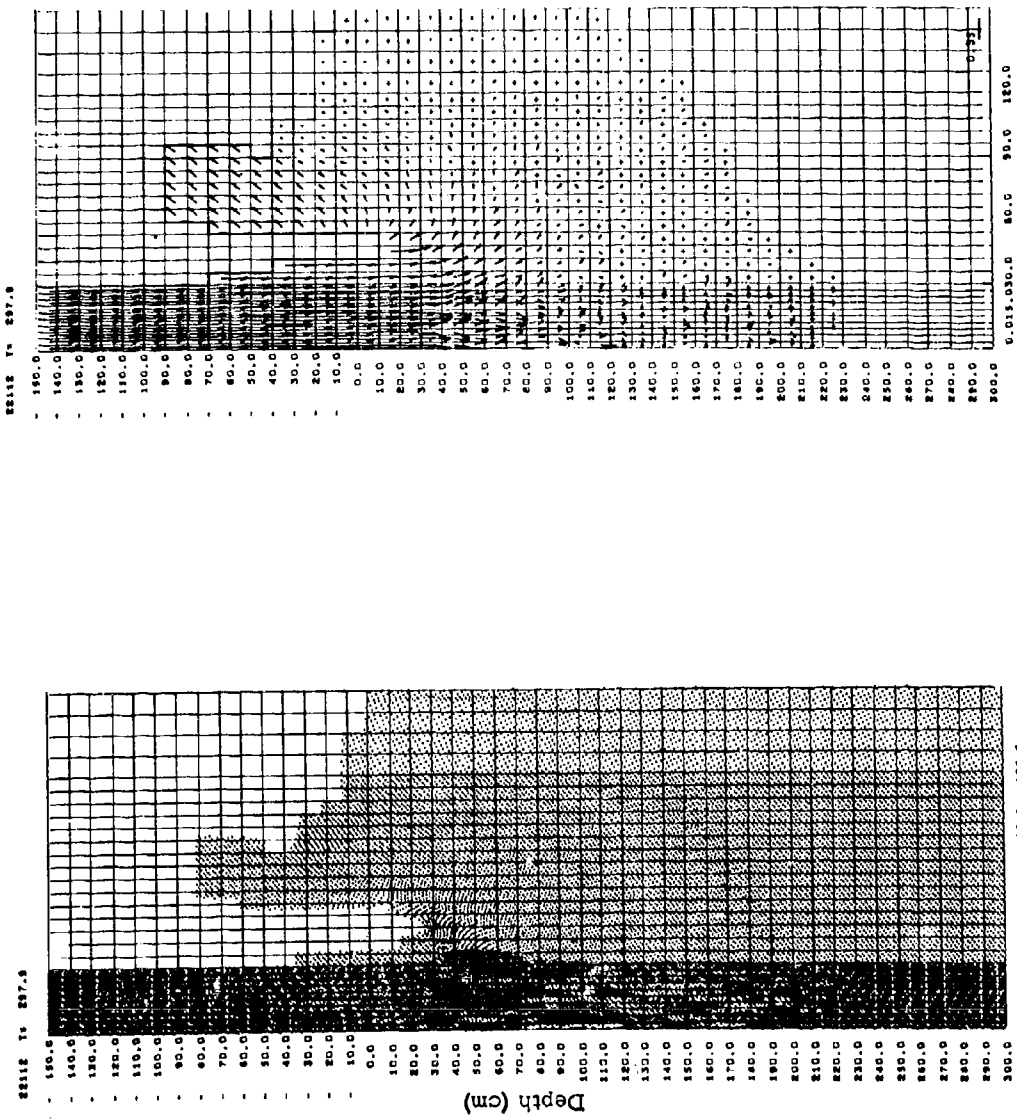
Depth (cm)
Radius (cm)

IMPACT CASE 12: Al vs Al @ 4.6 km/sec, T/D = 5

Figure A13 (facing): Mass Positions at 486, 565.3, and 742.1 μsec

The shock reaches the rear surface just before the first of these plots. Although instabilities are evident throughout the field at these late times, the shaft of the rod continues to advance into the target, opening a deeper hole.

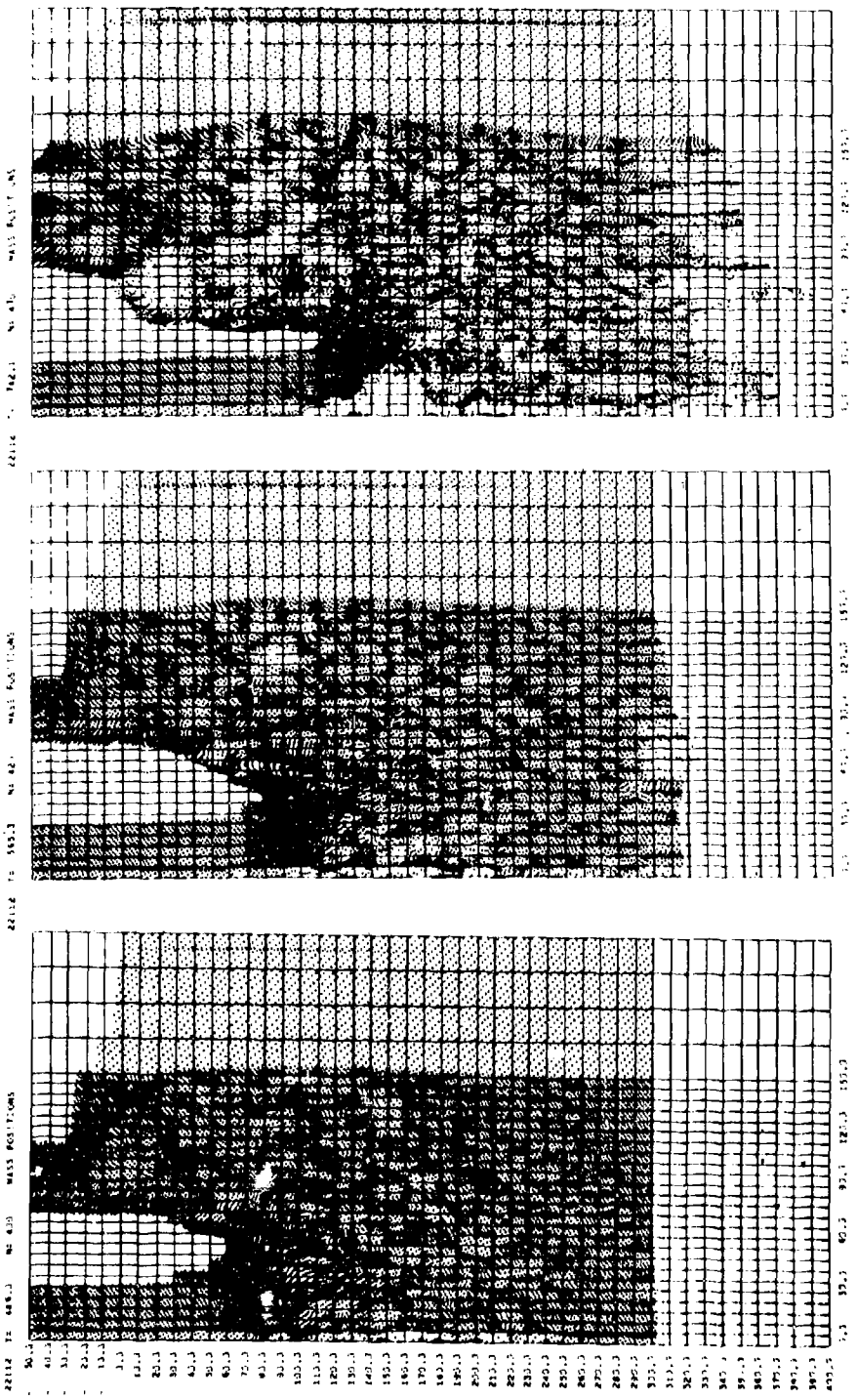

IMPACT CASE 12: Al vs Al @ 4.6 km/sec, T/D = 5

Figure A14(facing): Mass Positions at 872.7 and 1214 μsec, and Velocity Field at 1214 μsec

The effects of the instabilities which occur at low pressures are causing gross distortions in the solution, as is especially evident in the mass position plots. For this reason, little quantitative information can be obtained at these late times.

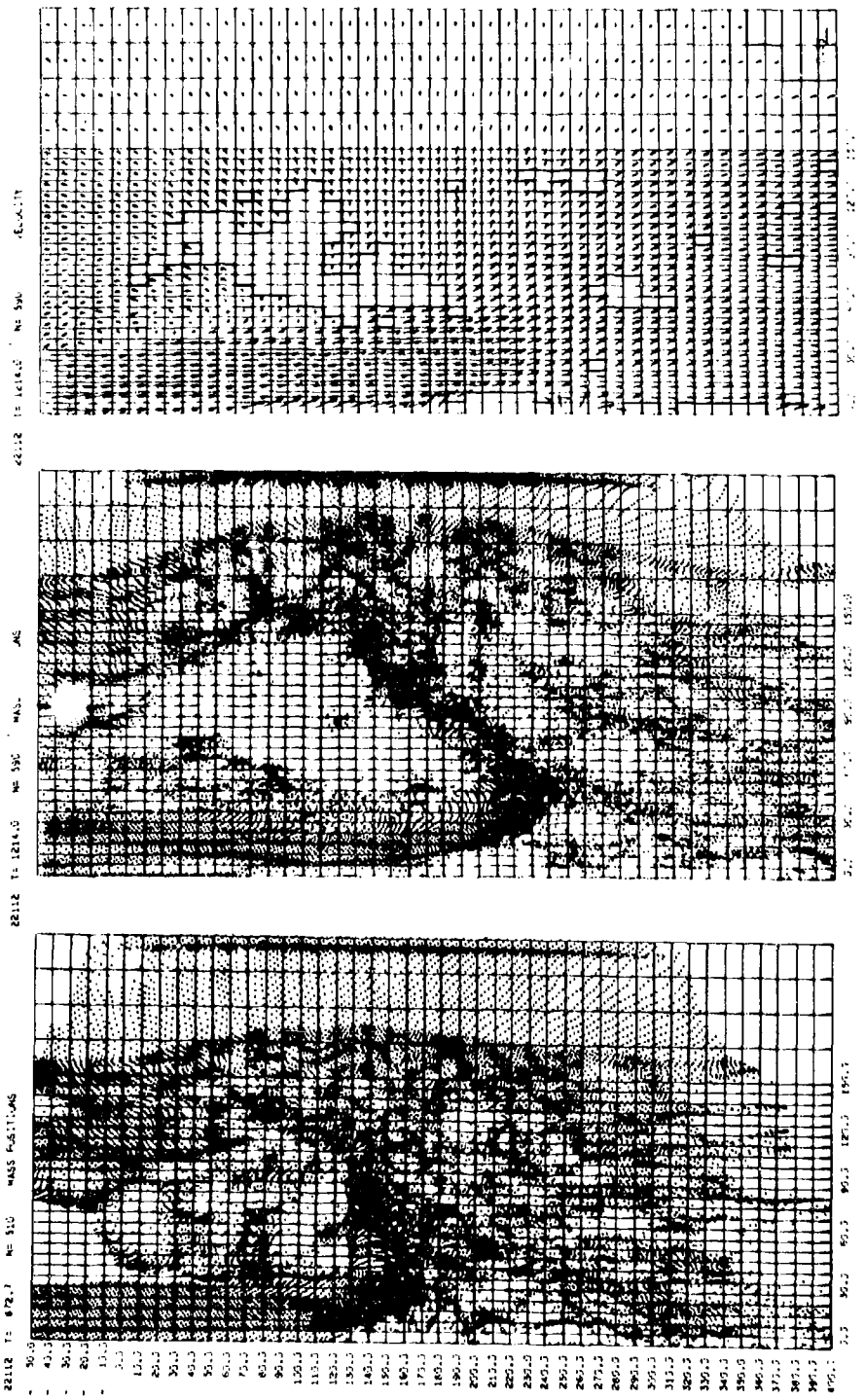

IMPACT CASE 21: Hollow Aluminum Rod vs Aluminum Plate, Normal Impact at 4.6 km/sec, Rod OD = 60 cm, ID = 20 cm (ID/OD = 1/3), Target Thickness = 120 cm (T/OD = 2)

Figure A15 (facing): Pressure Fields at 13.9 and 18.6 μsec

The left axis in these plots is the axis of symmetry (the center of the hollow rod). The contour lines are 10, 50, 100, 300, and 500 kb isobars. In these plots, the pressure field is expanding from the initial impact surface of the rod wall on the target. Convergence causes the pressures to be higher near the axis than in the outer direction. The shock consequently propagates more rapidly in the inner direction. This is evident at 13.9 μsec, in that while the pressure field extends nearly to the axis, a distance of 10 cm from the inner wall of the rod, it has propagated only about 8 cm outward from the outer wall of the rod.

By 18.6 μsec, the converging wave has reached the axis, resulting in a sharp build-up of pressure there.

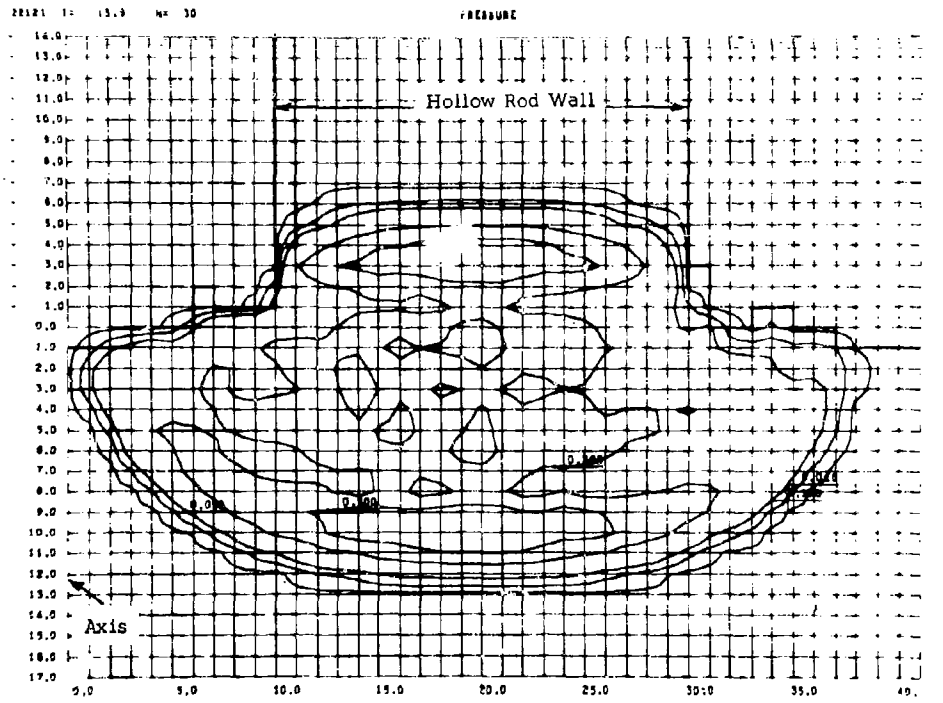
Hollow Rod Wall
Axis

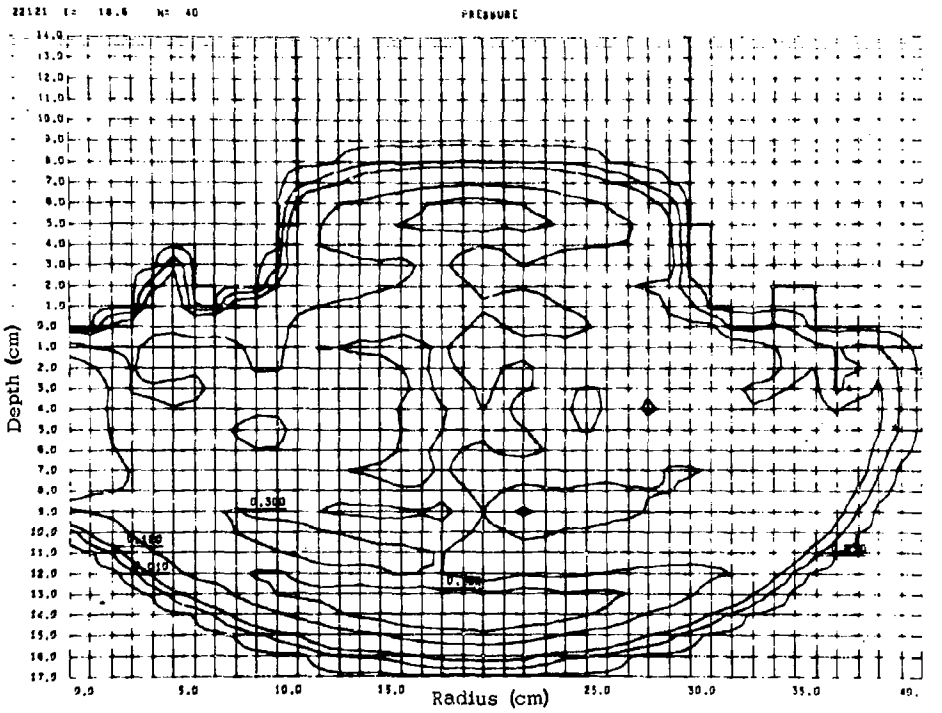
Depth (cm)
Radius (cm)

IMPACT CASE 21: Hollow Al vs Al @ 4.6 km/sec,
ID/OD = 1/3, T/OD = 2

Figure A16 (facing): Mass Positions and Velocity Field at 42.6 μsec

The pressure buildup caused by convergence of the shock upon the axis results in jetting of material back up the hollow center of the rod.

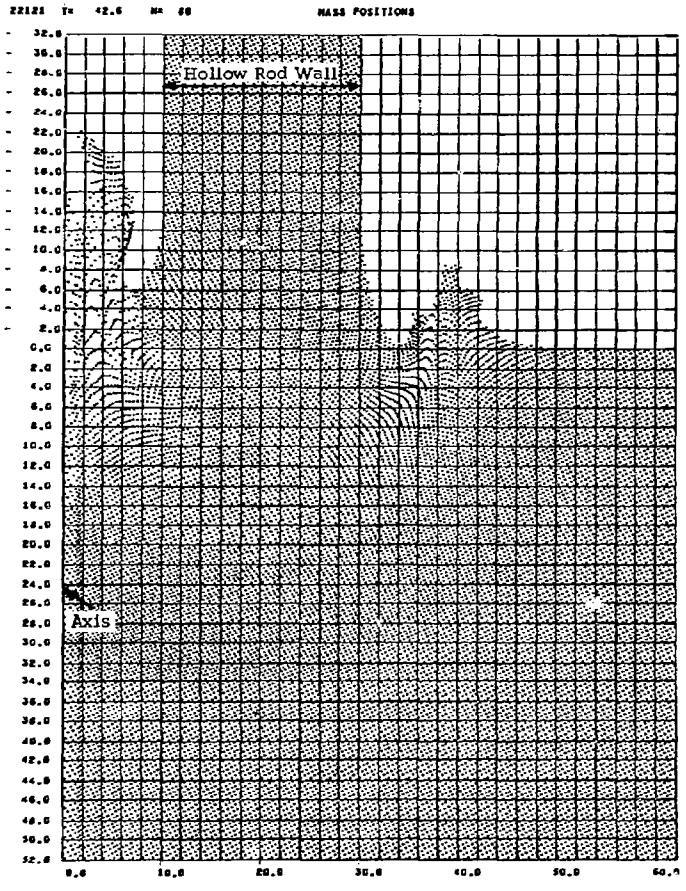
MASS POSITIONS
Hollow Rod Wall
Axis

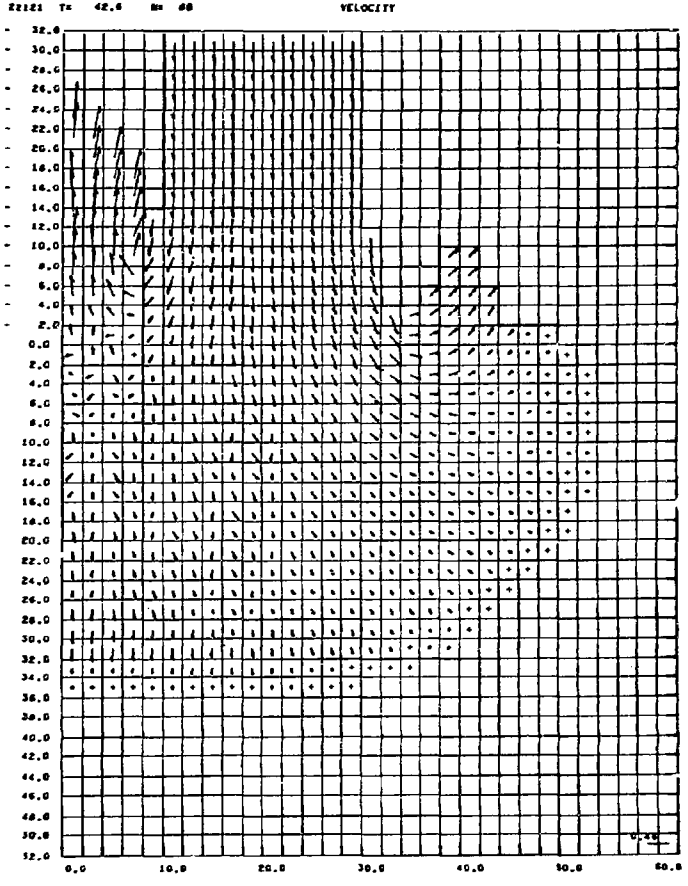
VELOCITY

IMPACT CASE 21: Hollow Al vs Al @ 4.6 km/sec,
ID/OD = 1/3, T/OD = 2

Figure A17 (facing): Mass Positions and Velocity Field at 61.1 μsec

The upward velocity of the center jet has a magnitude at least as large as the impact velocity.

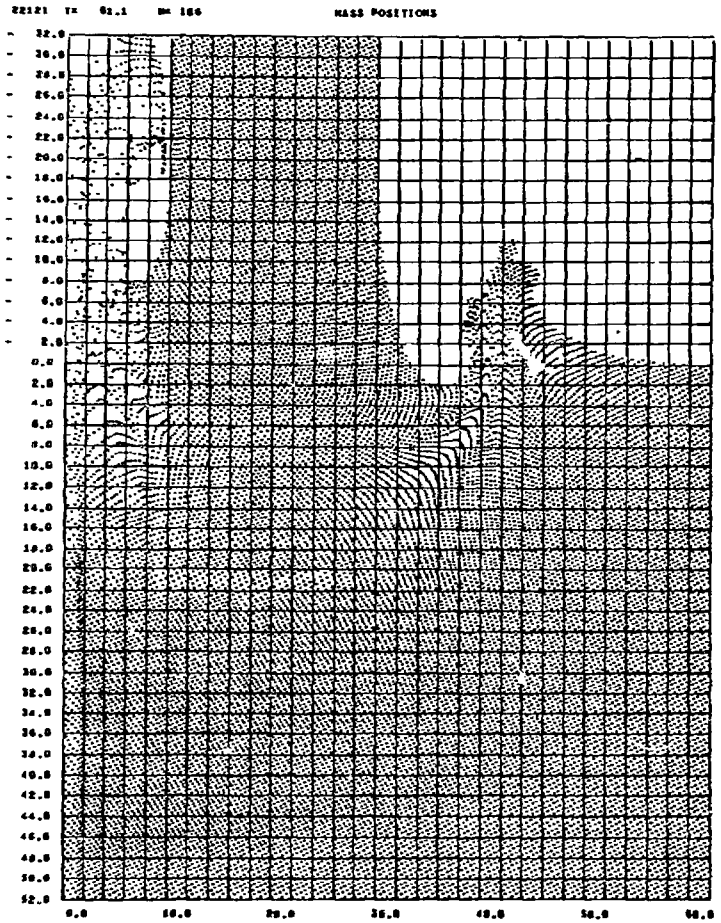
22121 T= 61.1 N= 186
MASS POSITIONS

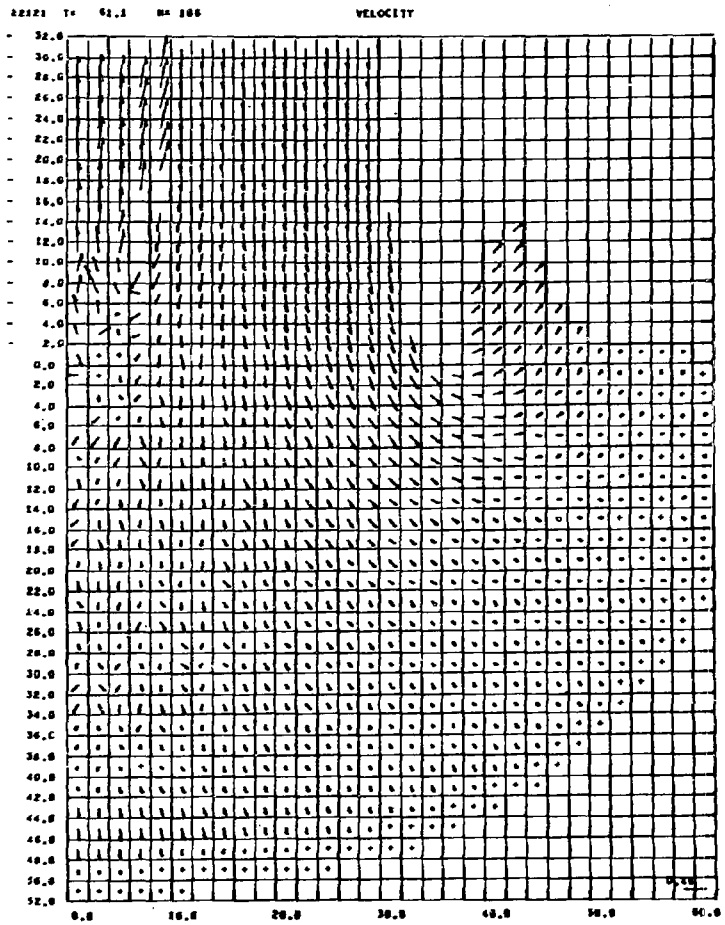
22121 T= 61.1 N= 186
VELOCITY

IMPACT CASE 21: Hollow Al vs Al @ 4.6 km/sec,
ID/OD = 1/3, T/OD = 2

Figure A18 (facing): Mass Positions and Velocity Field at 105.4 μsec

Deep in the target, and also at locations outside the rod wall, the flow field has characteristics similar to a solid rod impact. At shallow depths inside the rod wall, however, the flow is clearly perturbed by the hollow center. Jetting of material into this center continues.

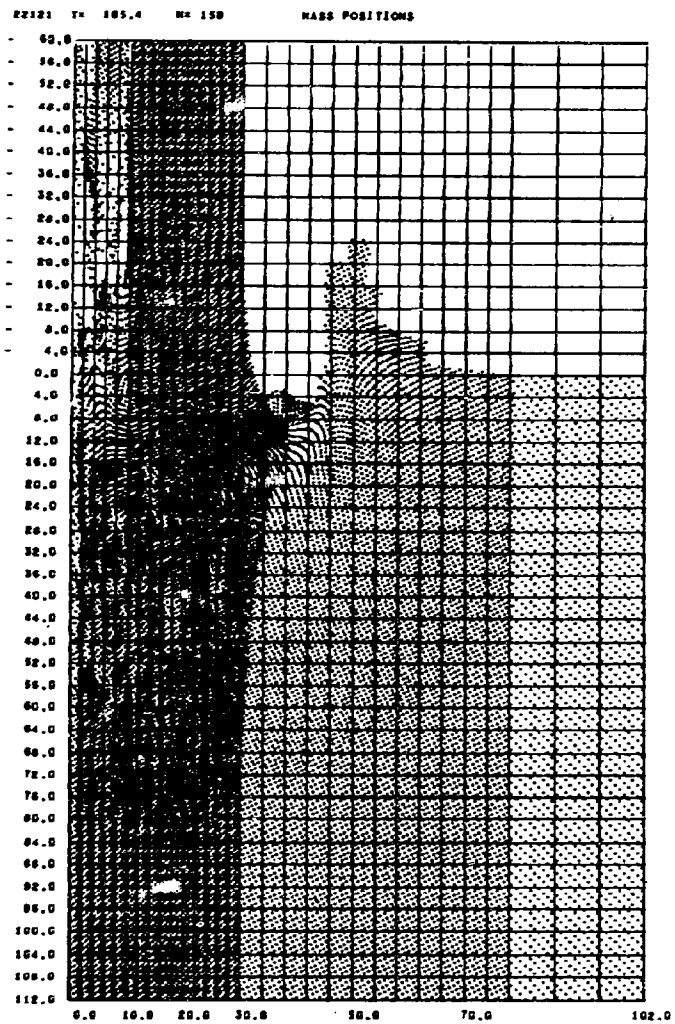
22121 T= 185.4 N= 150
MASS POSITIONS
0.0
10.0
20.0
30.0
50.0
70.0
102.0

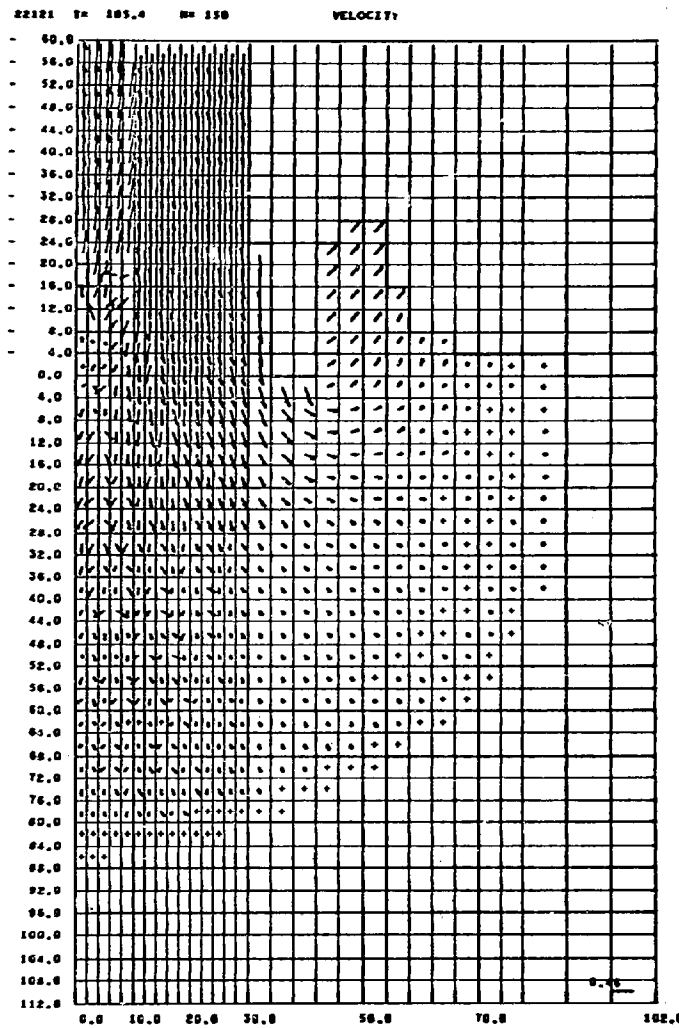
22121 T= 185.4 N= 150
VELOCITY
0.0
10.0
20.0
30.0
50.0
70.0
102.0

IMPACT CASE 21: Hollow Al vs Al @ 4.6 km/sec,
ID/OD = 1/3, T/OD = 2

Figure A19 (facing): Mass Positions at 255.4 and 411.1 μsec

An open hole, similar to that seen in solid rod impacts, is being formed as the hollow rod advances into the target. (Saturation of the reproduction process caused the large light regions below the hole.)

Jetting up the center hole has become relatively unstable in the numerical solution, and the resulting deterioration of the jet causes weak interactions with the inner walls.

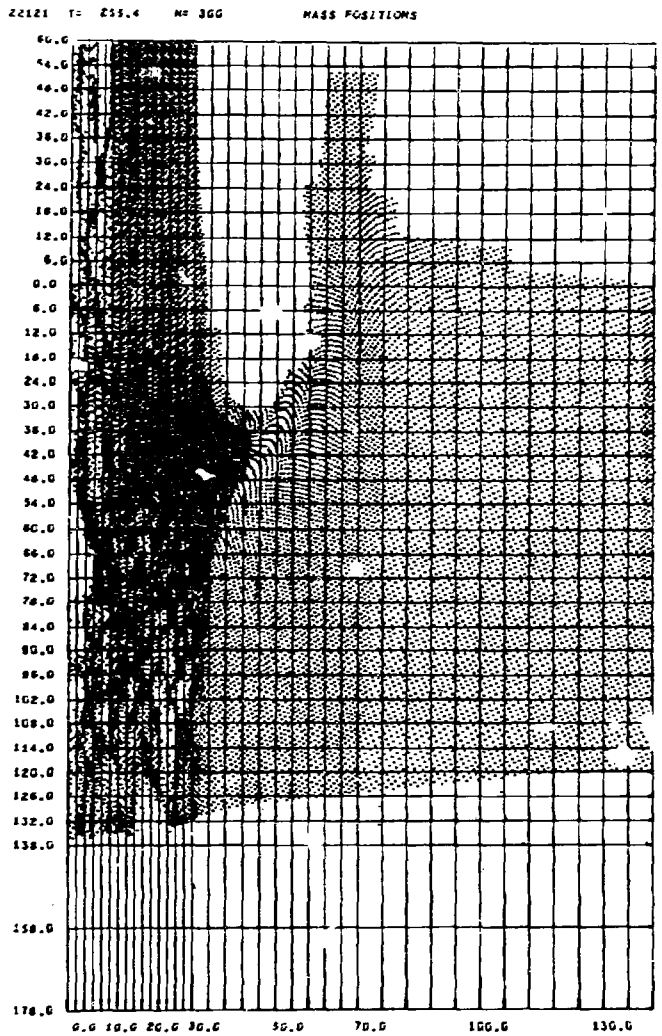
22121 T= 255.4 N= 300 MASS POSITIONS
0.0 10.0 20.0 30.0 50.0 70.0 100.0 130.0

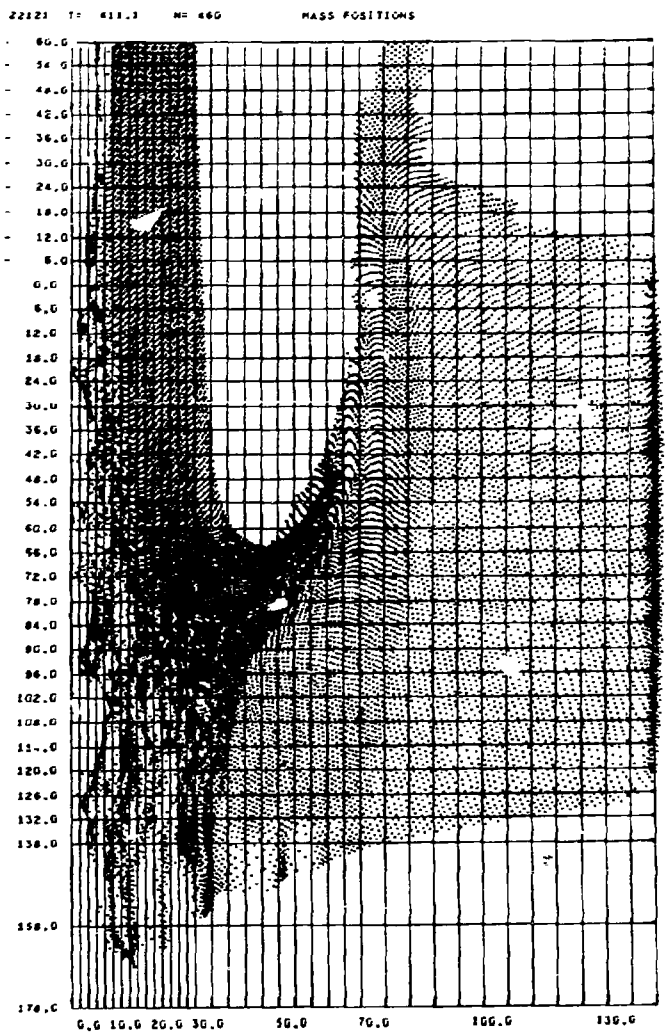
22121 T= 411.3 N= 460 MASS POSITIONS
0.0 10.0 20.0 30.0 50.0 70.0 100.0 130.0

IMPACT CASE 21: Hollow Al vs Al @ 4.6 km/sec
ID/OD = 1/3, T/OD = 2

Figure A20 (facing): Mass Positions and Velocity Field at 507.8 μsec

Although marked instabilities appear all along the axis, formation of the open hole continues in a smooth manner.

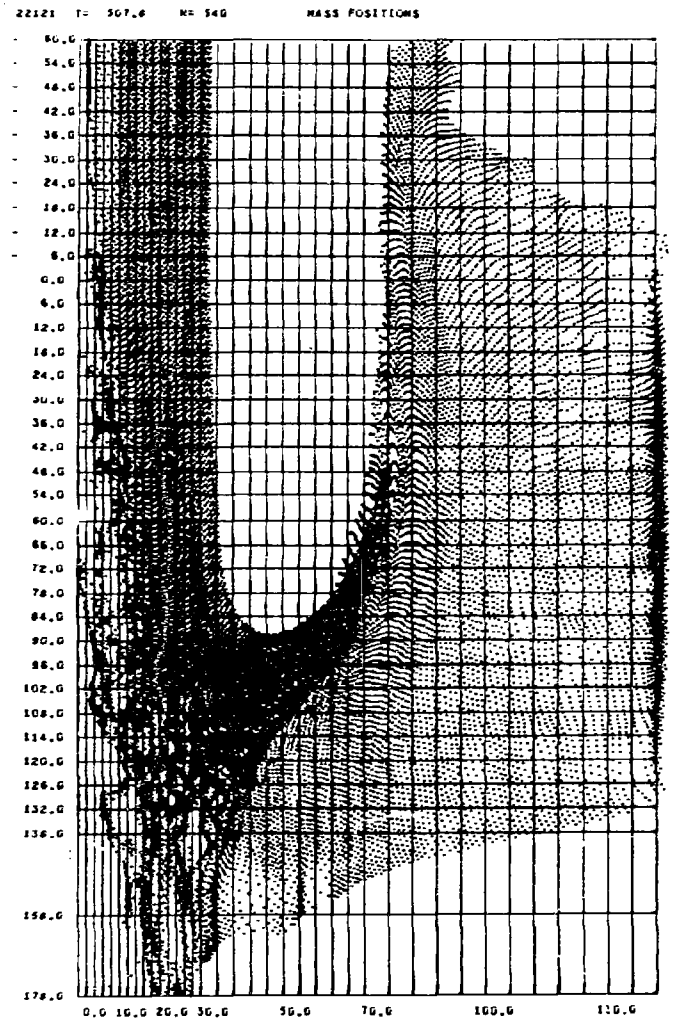
22121 T= 507.6 N= 548
MASS POSITIONS
0.0 10.0 20.0 30.0 50.0 70.0 100.0 130.0

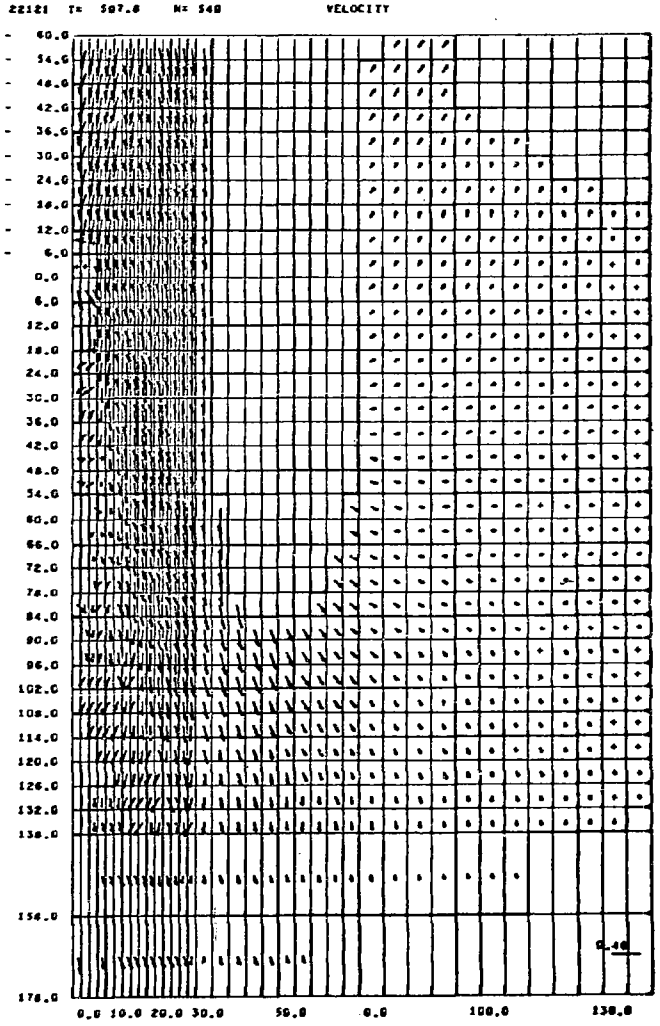
22121 T= 507.6 N= 548
VELOCITY
0.0 10.0 20.0 30.0 50.0 0.0 100.0 130.0

IMPACT CASE 22: Hollow Aluminum Rod vs Aluminum Plate,
Normal Impact at 4.6 km/sec,
Rod OD = 60 cm, ID = 40 cm
(ID/OD = 2/3),
Target Thickness = 120 cm (T/OD = 2)

Figure A21 (facing): Mass Positions and Velocity Vield at 52.4 μsec

As in Case 21 (ID/OD = 1/3) convergence of the shock wave system from the annular impact surface produces extreme pressures and consequent jetting back up the axis into the hollow center of the rod.

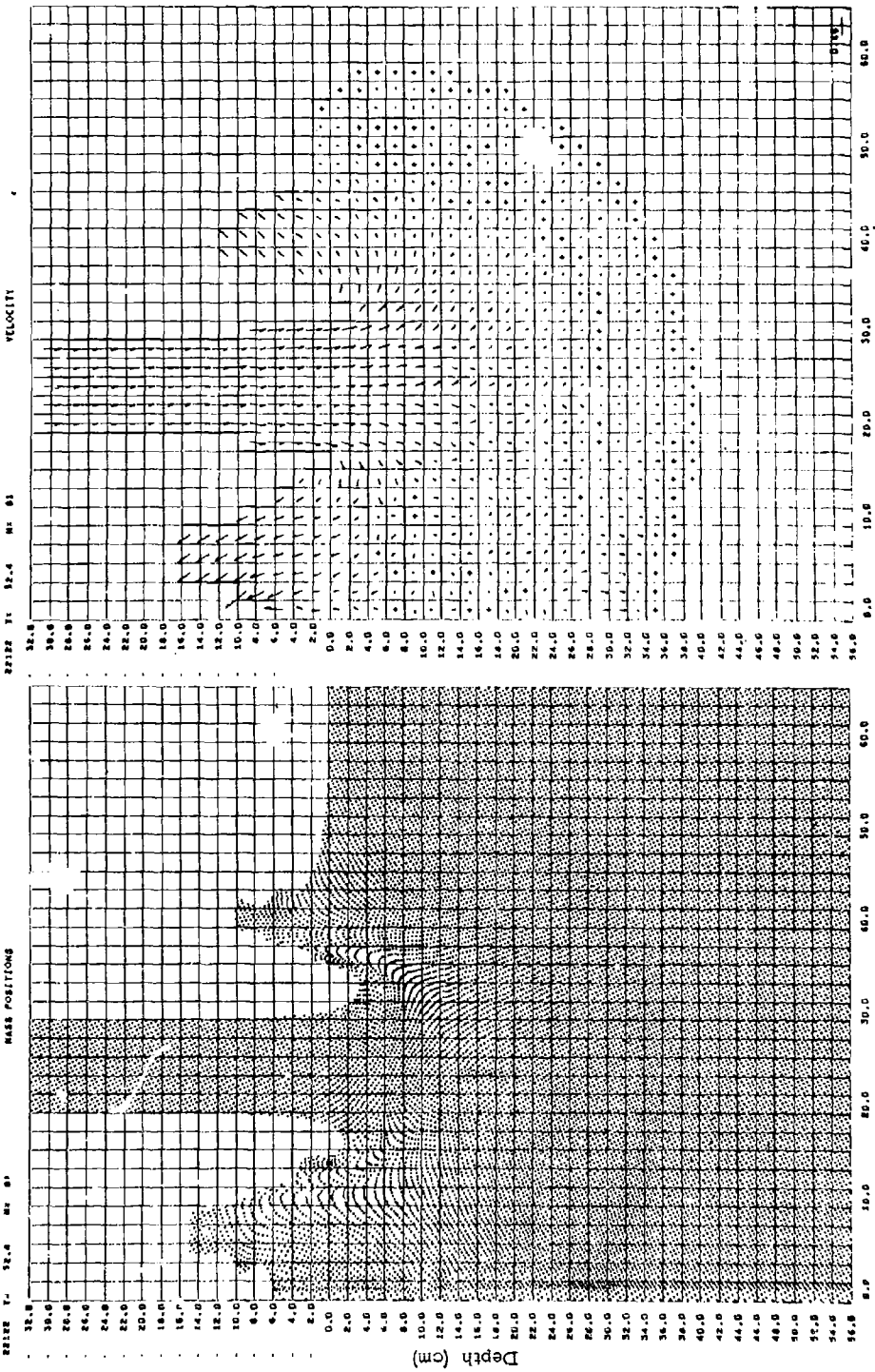
MASS POSITIONS
VELOCITY
Depth (cm)
Radius (cm)

IMPACT CASE 22: Hollow Al vs Al @ 4.6 km/sec,
ID/OD = 2/3, T/OD = 2

Figure A22 (facing): Mass Positions and Velocity Field at 126.6 μsec

A very pronounced, relatively massive counterflowing jet is apparent at this time, moving at an upward velocity slightly less than the impact velocity.

Outside of the hollow rod, an open hole is starting to form.

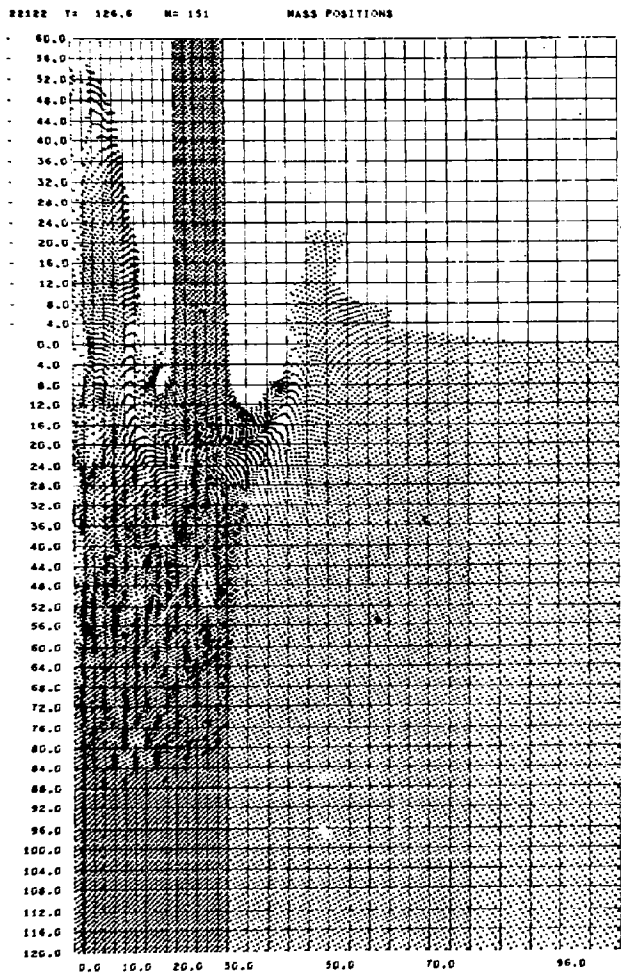
22122 T= 126.6 N= 151 MASS POSITIONS
60.0
56.0
52.0
48.0
44.0
40.0
36.0
32.0
28.0
24.0
20.0
16.0
12.0
8.0
4.0
0.0
4.0
8.0
12.0
16.0
20.0
24.0
28.0
32.0
36.0
40.0
44.0
48.0
52.0
56.0
60.0
64.0
68.0
72.0
76.0
80.0
84.0
88.0
92.0
96.0
100.0
104.0
108.0
112.0
116.0
120.0
0.0 10.0 20.0 30.0 50.0 70.0 96.0

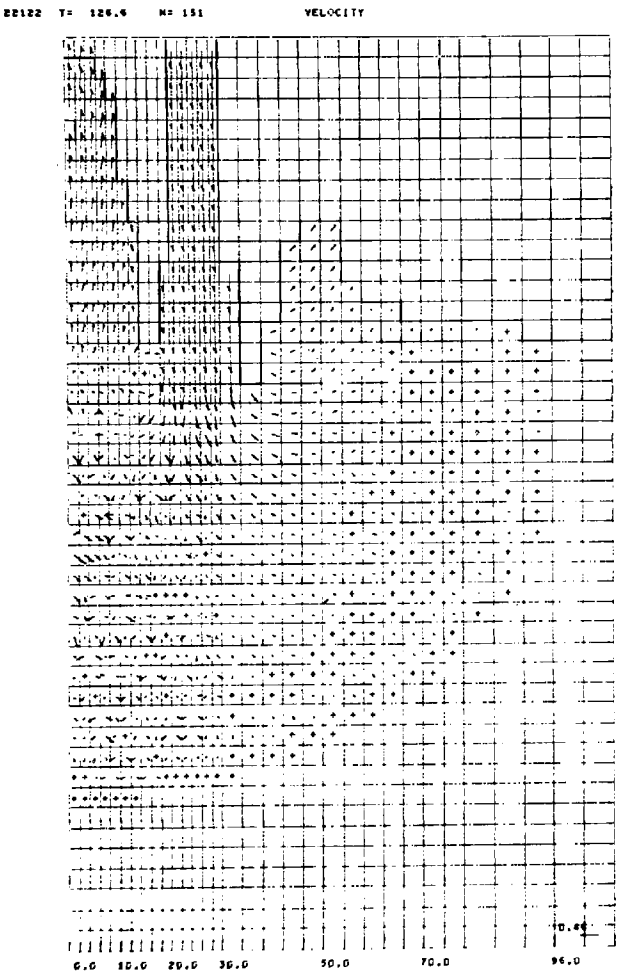
22122 T= 126.6 N= 151 VELOCITY
0.0 10.0 20.0 30.0 50.0 70.0 96.0

IMPACT CASE 22: Hollow Al vs Al @ 4.6 km/sec,
ID/OD = 2/3, T/OD = 2

Figure A23 (facing): Mass Positions and Velocity Field at 223.7 μsec

The counterflow in this ID/OD = 2/3 problem is more massive and more stable than in Case 21 (ID/OD = 1/3). This is evident in comparing the flow field in Figure A23 with that in Figure A19 at 255 μsec.

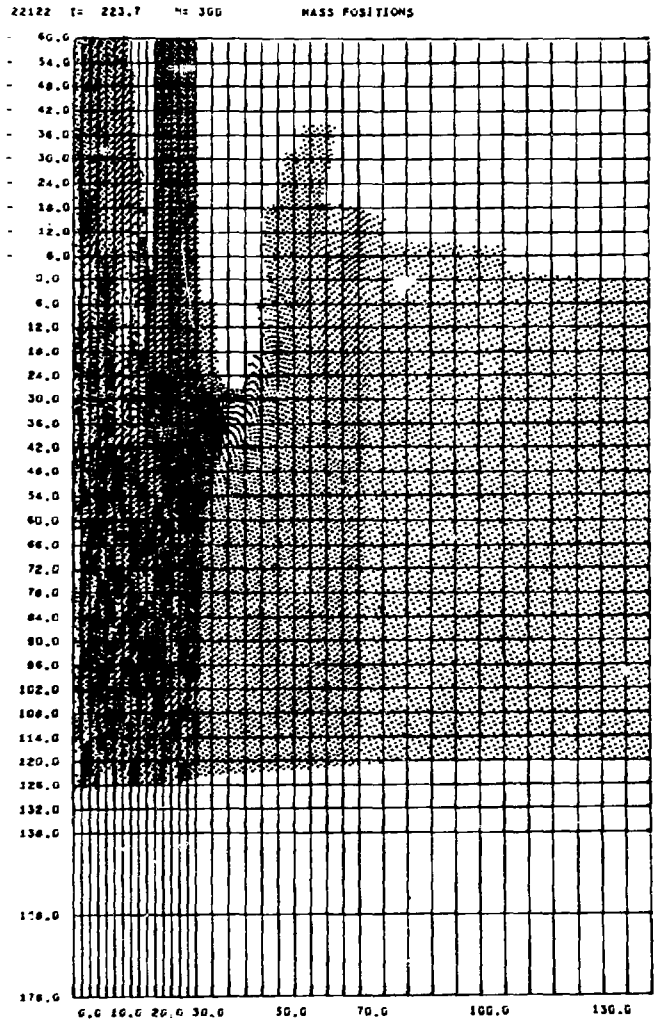
22122 T= 223.7 N= 300
MASS POSITIONS
60.0
54.0
48.0
42.0
36.0
30.0
24.0
18.0
12.0
6.0
0.0
6.0
12.0
18.0
24.0
30.0
36.0
42.0
48.0
54.0
60.0
66.0
72.0
78.0
84.0
90.0
96.0
102.0
108.0
114.0
120.0
126.0
132.0
138.0
178.0
0.0 10.0 20.0 30.0 50.0 70.0 100.0 130.0

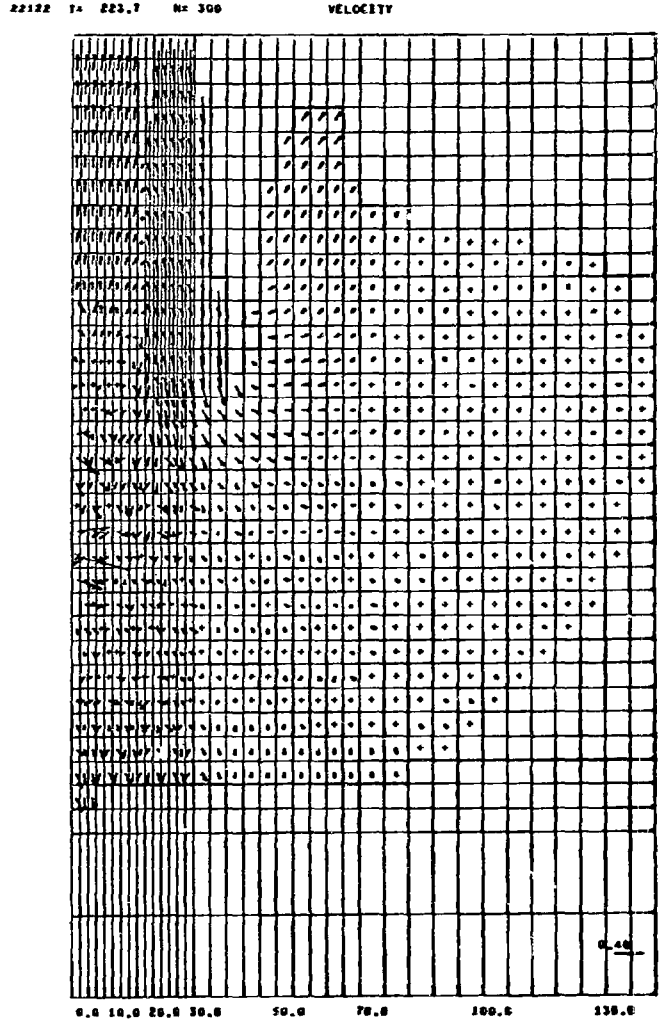
22122 T= 223.7 N= 300
VELOCITY
0.0 10.0 20.0 30.0 50.0 70.0 100.0 130.0

IMPACT CASE 22: Hollow Al vs Al @ 4.6 km/sec,
ID/OD = 2/3, T/OD = 2

Figure A24 (facing): Mass Positions
at 325.3 and 630.9 μsec

The counterflow is becoming unstable by 630.9 μsec.

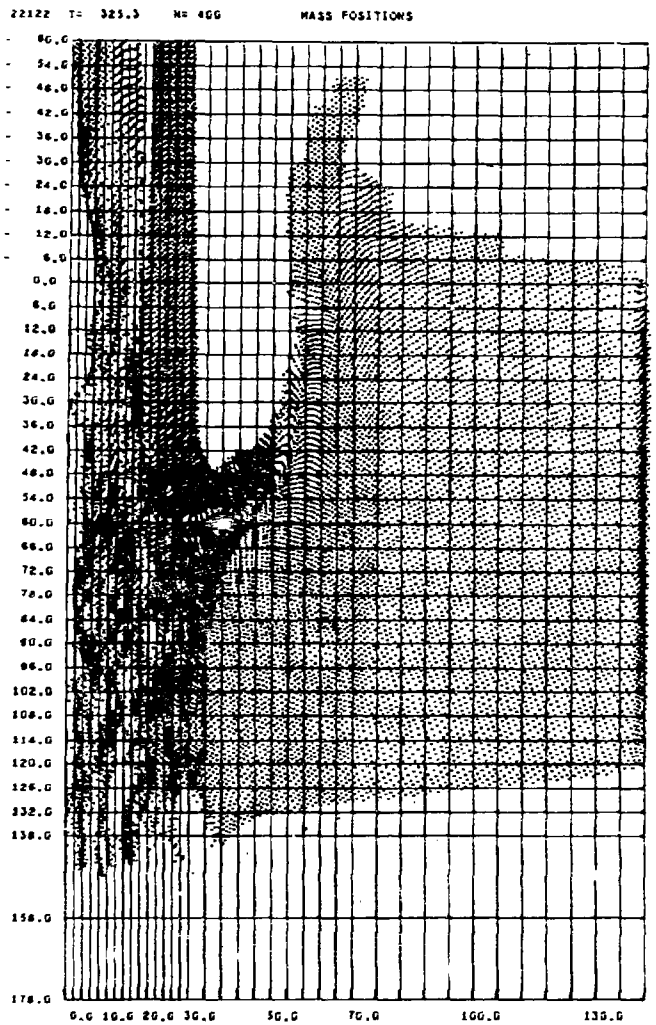
22122 T= 325.5 N= 400
MASS POSITIONS
0.0 10.0 20.0 30.0 50.0 70.0 100.0 130.0

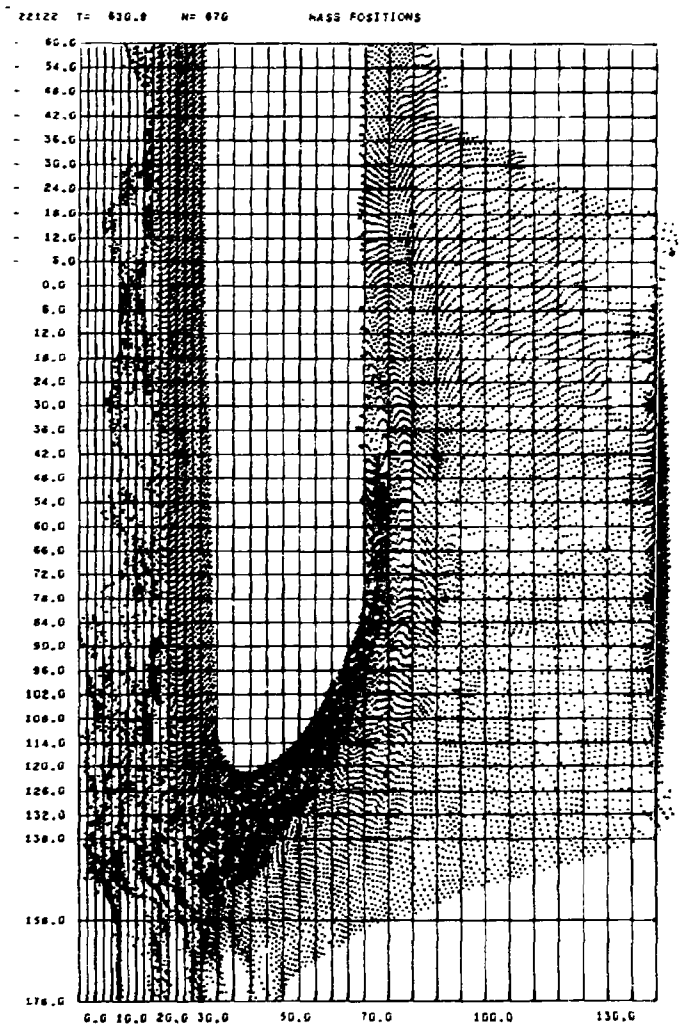
22122 T= 630.0 N= 670
MASS POSITIONS
0.0 10.0 20.0 30.0 50.0 70.0 100.0 130.0

IMPACT CASE 22: Hollow Al vs Al @ 4.6 km/sec,
ID/OD = 2/3, T/OD = 2

Figure A25 (facing): Mass Positions and Velocity Field at 718.2 μsec

The open hole has reached a depth of over 140 cm by this time. The counterflow is unstable, and is interacting weakly with the inner walls. The instabilities are probably due to limitations of the numerical technique at low stresses. In actual physical cases, a stable jet probably forms.

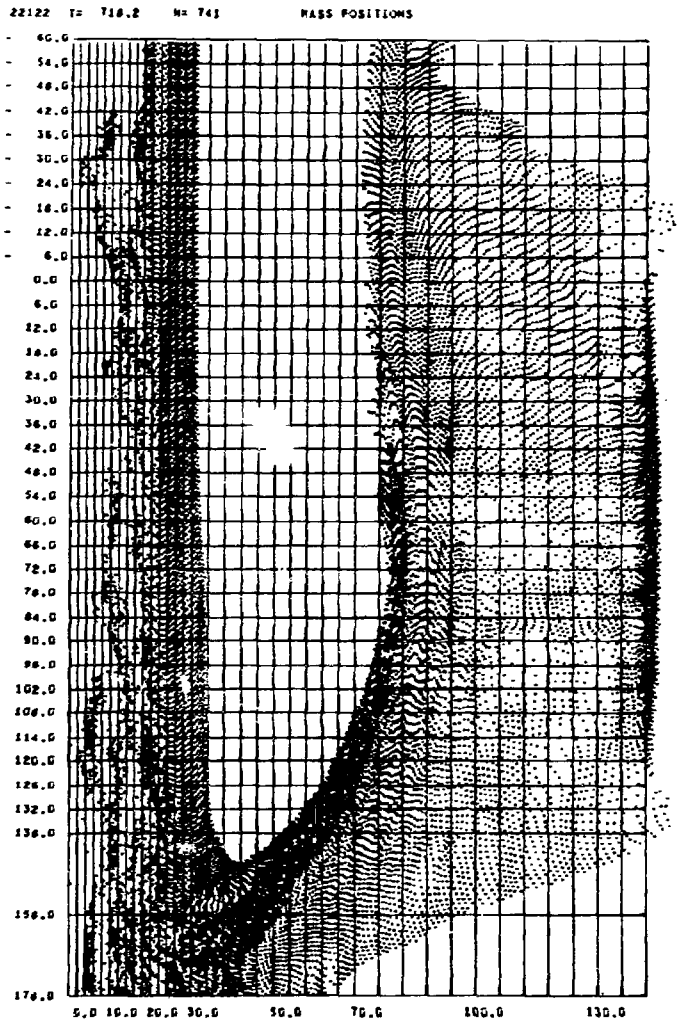
22122 T= 718.2 N= 741
MASS POSITIONS
0.0 10.0 20.0 30.0 50.0 70.0 100.0 130.0

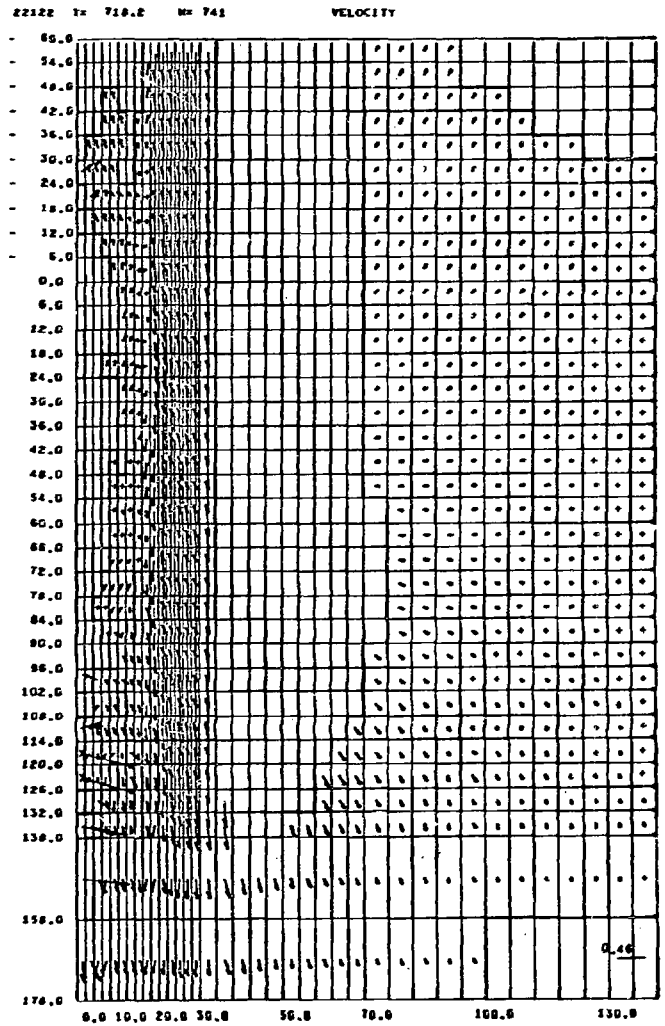
22122 T= 718.2 N= 741
VELOCITY
0.0 10.0 20.0 30.0 50.0 70.0 100.0 130.0

IMPACT CASE 23: Hollow Iron Rod vs Aluminum Plate.
Normal Impact at 4.6 km/sec,
Rod OD = 60 cm, ID = 40 cm
(ID/OD = 2/3)
Target Thickness = 120 cm (T/OD = 2)

Figure A26 (facing): Mass Positions and Velocity and Pressure Fields at 23.2 μsec

Impact of the hollow iron rod produces higher initial pressures than the corresponding aluminum rod impact (Case 22).

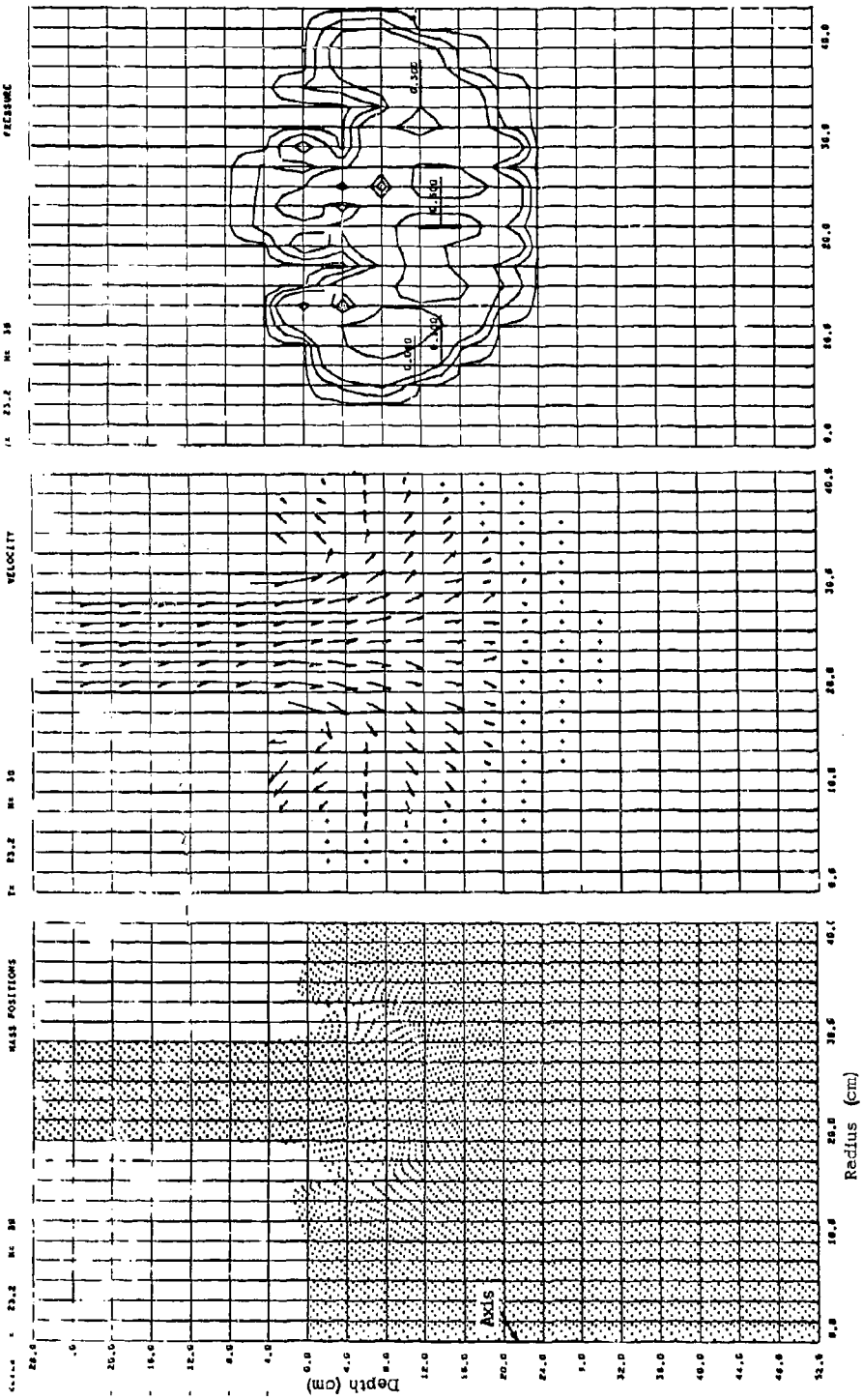
MASS POSITIONS
VELOCITY
PRESSURE
Axis
Depth (cm)
Radius (cm)

IMPACT CASE 23: Hollow Fe vs Al @ 4.6 km/sec,
ID/OD = 2/3, T/OD = 2

Figure A27 (facing): Mass Positions at 43.2 and 63.0 μsec

Note the rebound of material from the sides of the open annular holes towards the rod wall.

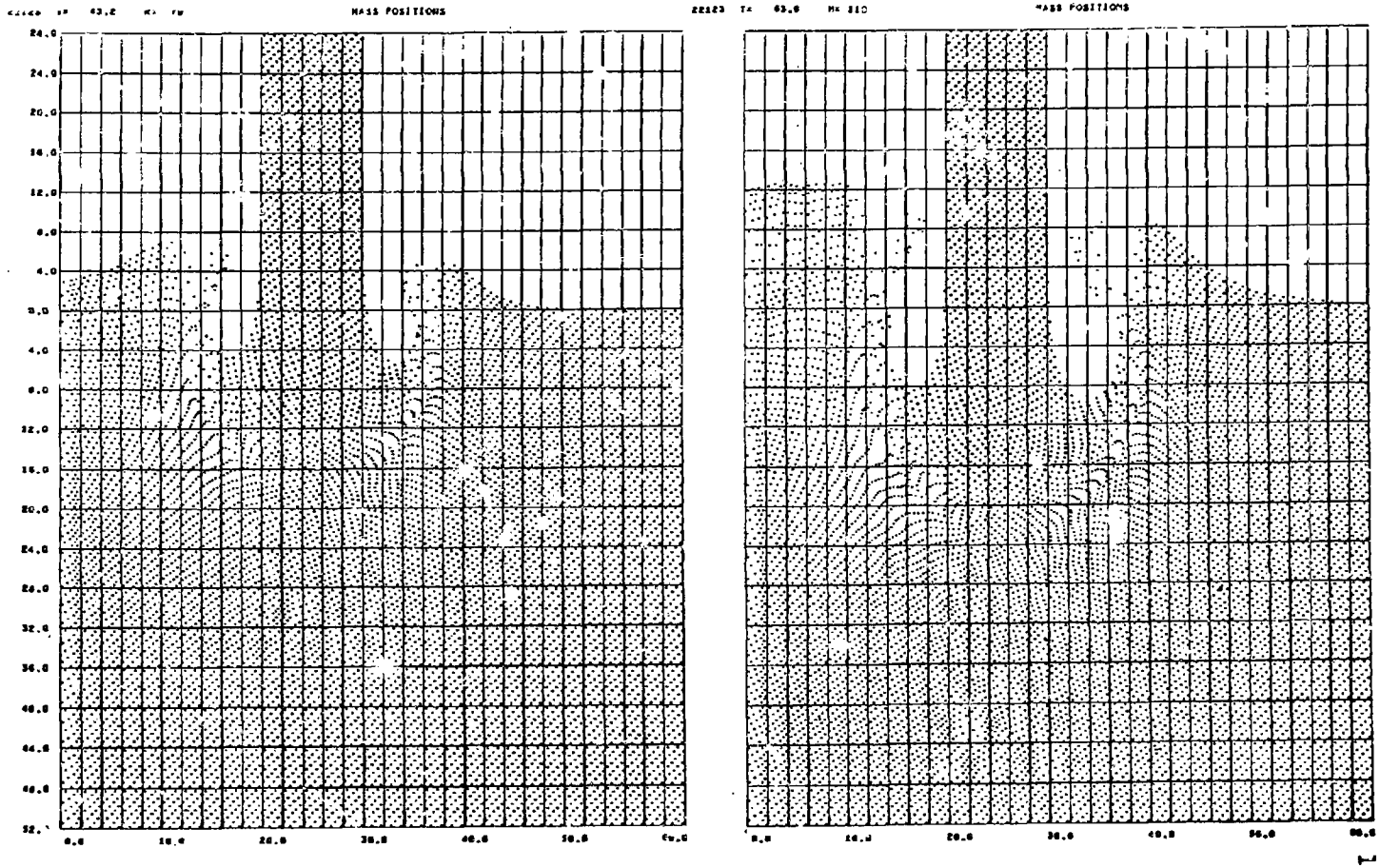
MASS POSITIONS
MASS POSITIONS

IMPACT CASE 23: Hollow Fe vs Al @ 4.6 km/sec,
ID/OD = 2/3, T/OD = 2

Figure A28 (facing): Mass Positions and Velocity Field at 149.2 μsec

As in the corresponding hollow aluminum rod (Case 22), a relatively large counterflowing mass travels back up the hollow center. This mass is primarily target material.

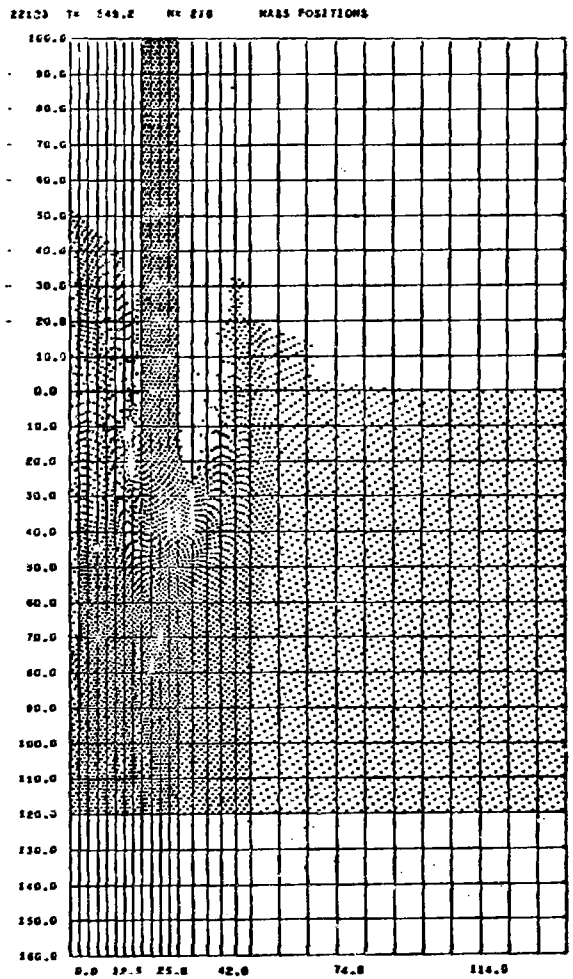
22123 T= 549.2 N= 210 MASS POSITIONS
0.0
12.5
25.0
42.0
74.0
114.0

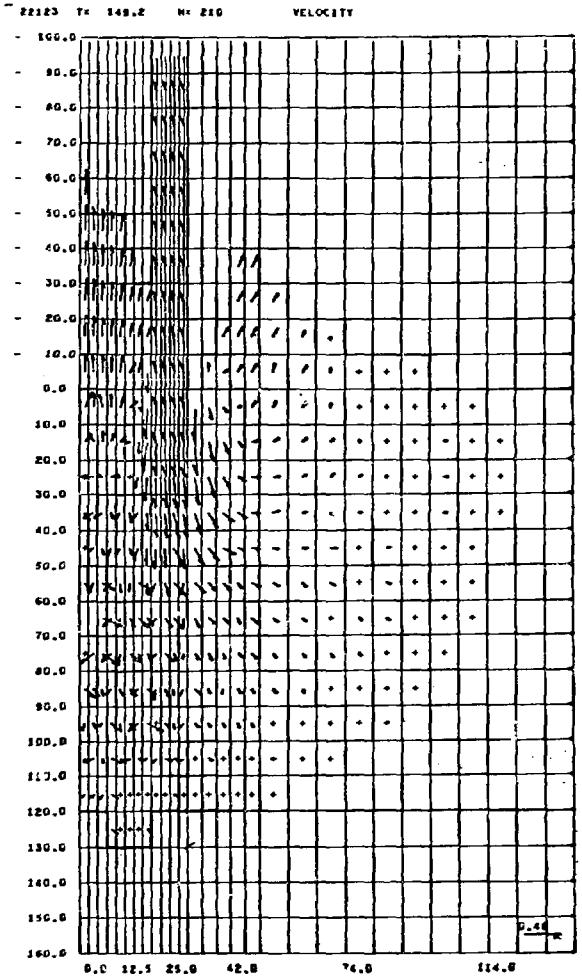
22123 T= 549.2 N= 210 VELOCITY
0.0
12.5
25.0
42.0
74.0
114.0

IMPACT CASE 23: Hollow Fe vs Al @ 4.6 km/sec,
ID/OD = 2/3, T/OD = 2

Figure A29 (facing): Mass Positions and Velocity Field at 219.1 μsec

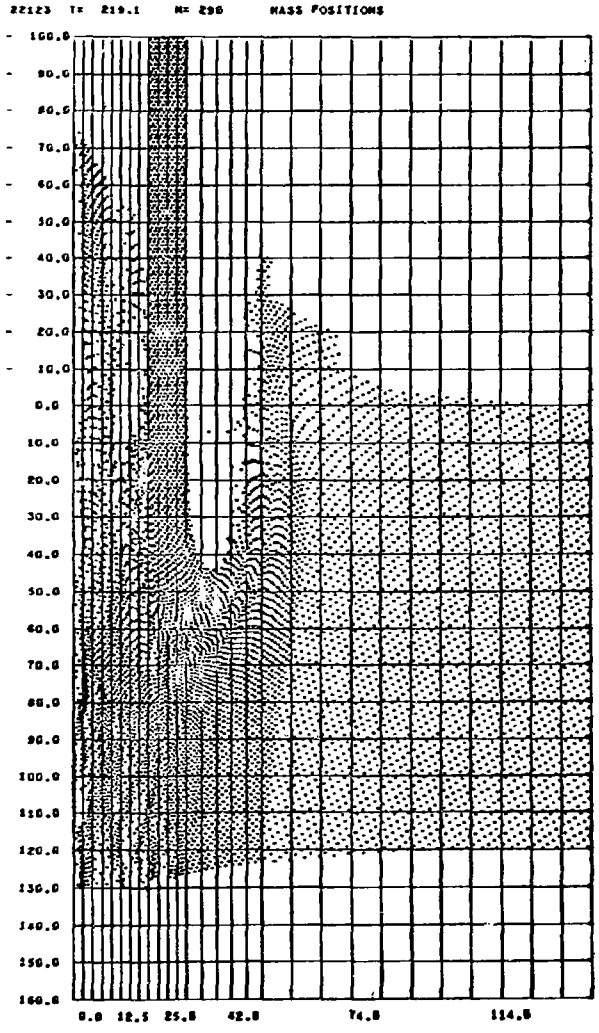
22123 T= 219.1 N= 298 MASS POSITIONS
100.0
90.0
80.0
70.0
60.0
50.0
40.0
30.0
20.0
10.0
0.0
10.0
20.0
30.0
40.0
50.0
60.0
70.0
80.0
90.0
100.0
110.0
120.0
130.0
140.0
150.0
160.0
0.0 12.5 25.0 42.0 74.0 114.0

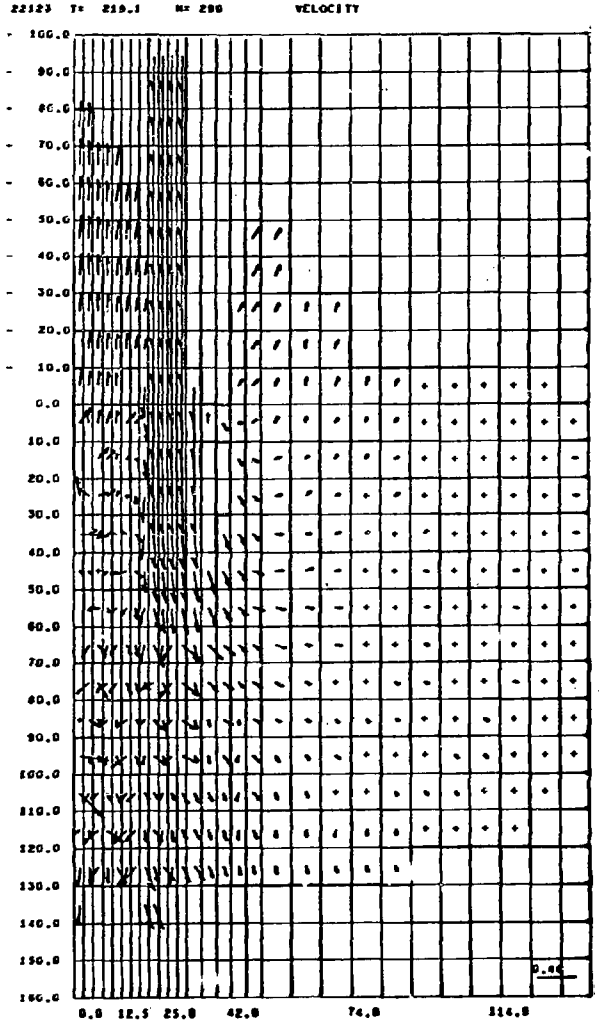
22123 T= 219.1 N= 298 VELOCITY
100.0
90.0
80.0
70.0
60.0
50.0
40.0
30.0
20.0
10.0
0.0
10.0
20.0
30.0
40.0
50.0
60.0
70.0
80.0
90.0
100.0
110.0
120.0
130.0
140.0
150.0
160.0
0.0 12.5 25.0 42.0 74.0 114.0

IMPACT CASE 23: Hollow Fe vs Al @ 4.6 km/sec,
ID/OD = 2/3, T/OD = 2

Figure A30 (facing): Mass Positions at 320.3 and 484.7 μsec

The mass positions at 320.3 μsec can be directly compared with the plot in Figure A24 for the corresponding aluminum rod impact. The iron rod impact produces an appreciably deeper annular hole.

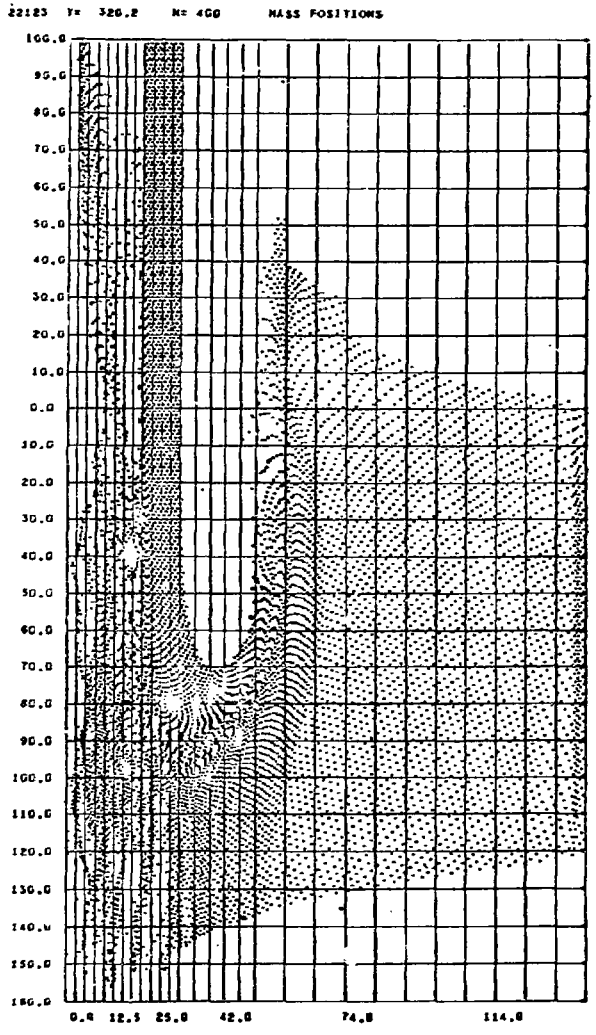
22123 Y= 326.2 N= 400 MASS POSITIONS
100.0
90.0
80.0
70.0
60.0
50.0
40.0
30.0
20.0
10.0
0.0
10.0
20.0
30.0
40.0
50.0
60.0
70.0
80.0
90.0
100.0
110.0
120.0
130.0
140.0
150.0
160.0
0.0 12.5 25.0 42.0 74.0 114.0

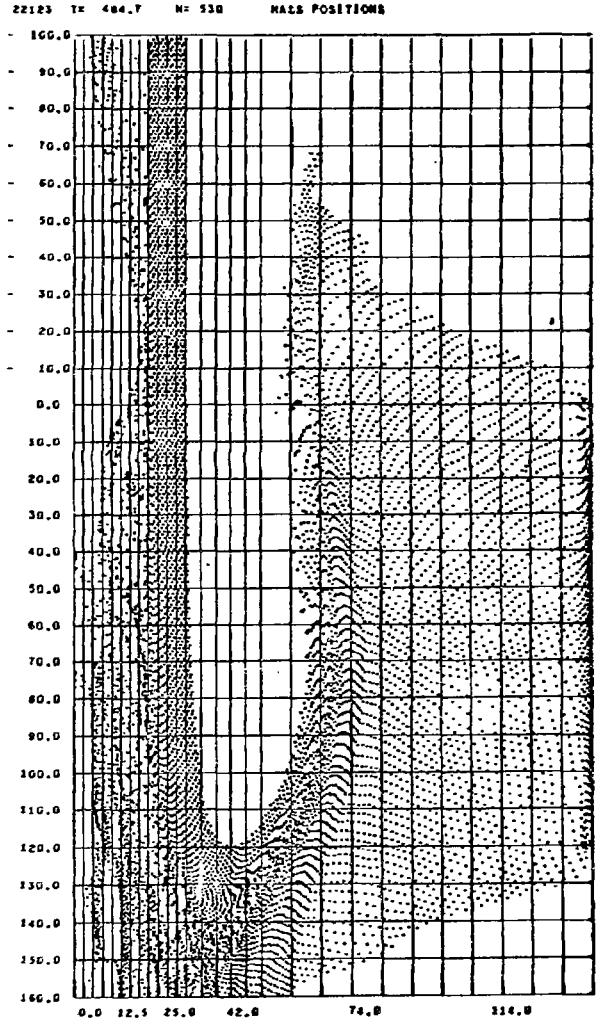
22123 Y= 484.7 N= 530 MASS POSITIONS
100.0
90.0
80.0
70.0
60.0
50.0
40.0
30.0
20.0
10.0
0.0
10.0
20.0
30.0
40.0
50.0
60.0
70.0
80.0
90.0
100.0
110.0
120.0
130.0
140.0
150.0
160.0
0.0 12.5 25.0 42.0 74.0 114.0

IMPACT CASE 23: Hollow Fe vs Al @ 4.6 km/sec,
ID/OD = 2/3, T/OD = 2

Figure A31 (facing): Mass Positions and Velocity Field at 585 μsec

The leading (upper) tip of the center jet continues to travel upward at high velocity.

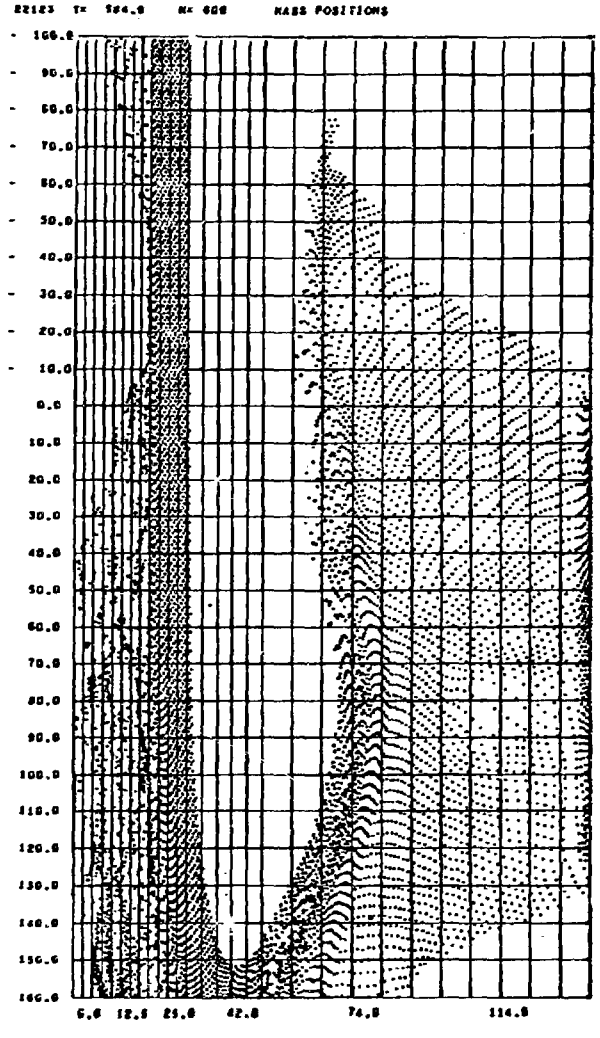
22123 T= 584.0 N= 600 MASS POSITIONS
100.0
90.0
80.0
70.0
60.0
50.0
40.0
30.0
20.0
10.0
0.0
10.0
20.0
30.0
40.0
50.0
60.0
70.0
80.0
90.0
100.0
110.0
120.0
130.0
140.0
150.0
160.0
6.0 12.5 25.0 42.0 74.0 114.0

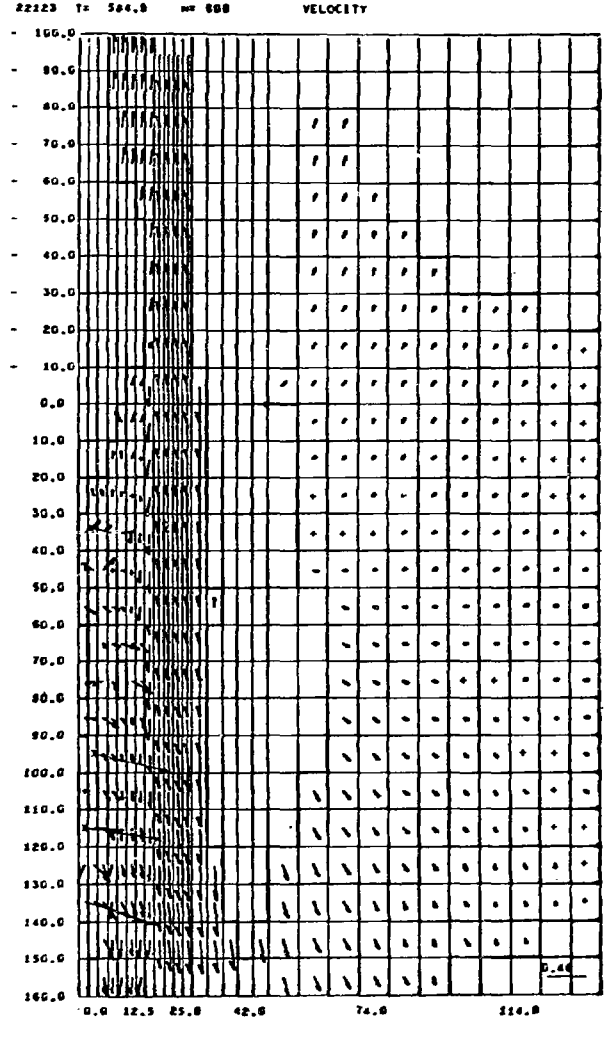
22123 T= 584.0 N= 600 VELOCITY
100.0
90.0
80.0
70.0
60.0
50.0
40.0
30.0
20.0
10.0
0.0
10.0
20.0
30.0
40.0
50.0
60.0
70.0
80.0
90.0
100.0
110.0
120.0
130.0
140.0
150.0
160.0
0.0 12.5 25.0 42.0 74.0 114.0

IMPACT CASE 31: Aluminum Plate vs Aluminum Plate (Planar Solution),
Normal Impact at 4.6 km/sec,
Projectile Plate Thickness ("D") = 60 cm,
Target Plate Thickness = 120 cm (T/D = 2)

Figure A32 (facing): Mass Positions and Velocity Field at 33.8 μsec

This planar solution was made for comparison with axisymmetric Case 4. The left axis is a plane of symmetry. At early times, the differences between axial and plane symmetry solutions are small, as can be seen by the comparison of the velocity field facing with the axisymmetric velocity field at 36.2 μsec in Figure A4.

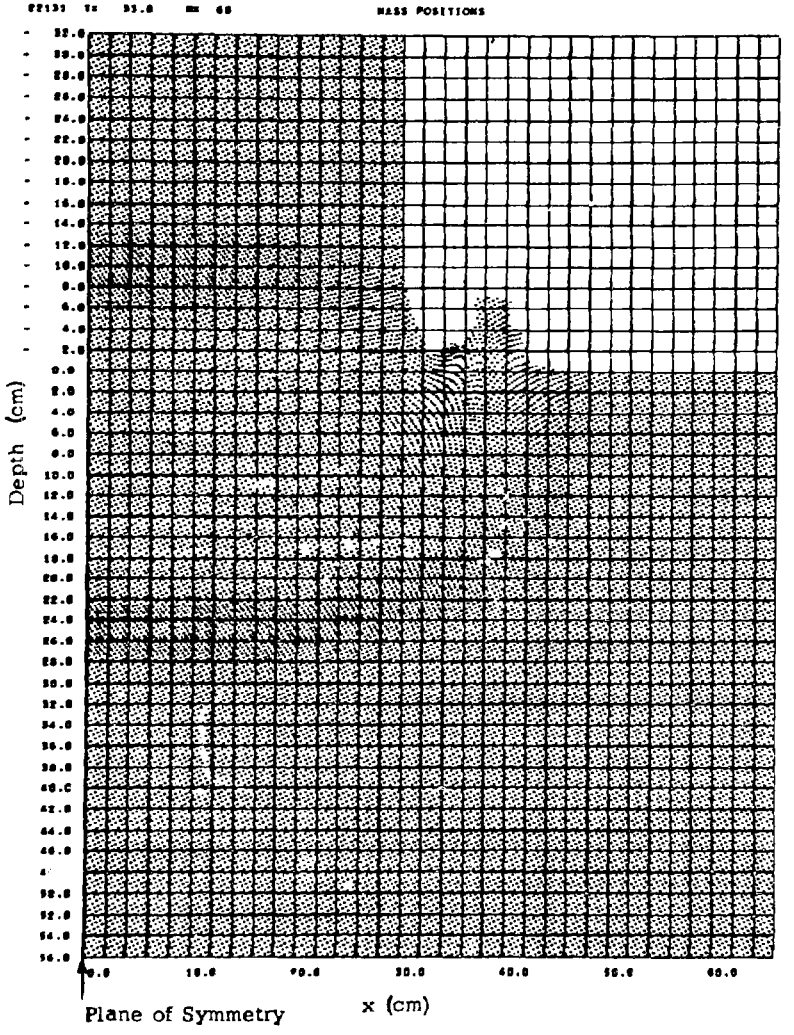
MASS POSITIONS
Depth (cm)
Plane of Symmetry
x (cm)

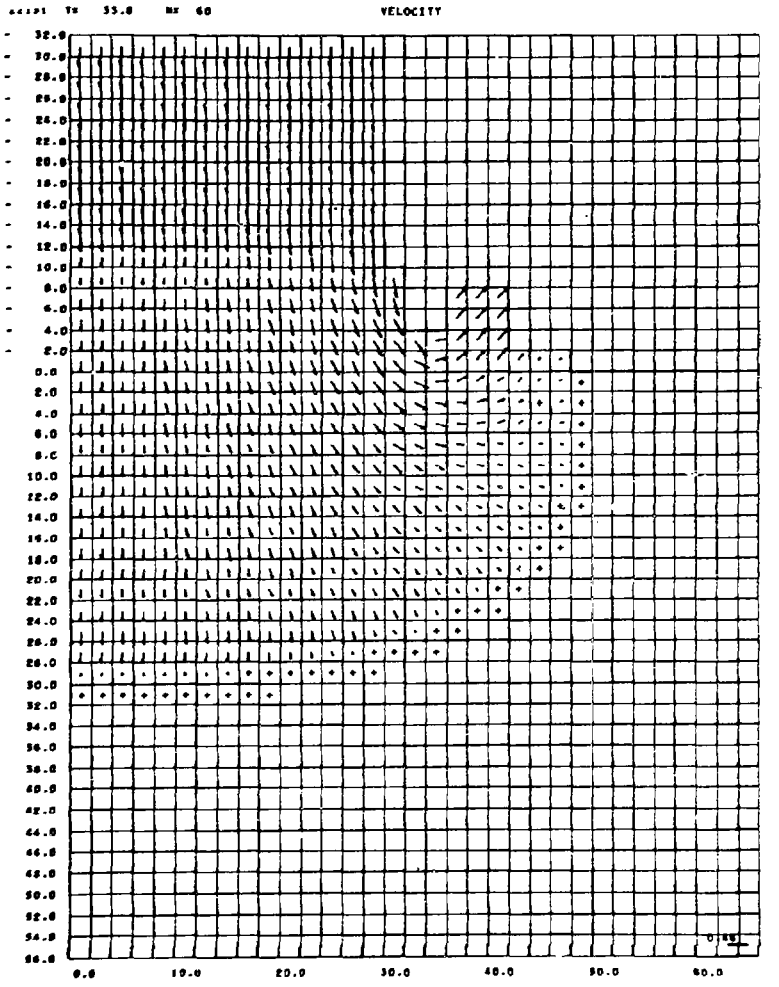
VELOCITY

IMPACT CASE 31: Planar Solution of Al vs Al @ 4.6 km/sec, (T/D = 2)

Figure A33 (facing): Mass Positions and Velocity Field at 116.1 μsec

The closest comparable plots for the axisymmetric solution are at 111.2 μsec in Figure A6. By this time, perceptible differences in the flow fields are appearing, in that the planar solution flow field engulfs a greater volume of material.

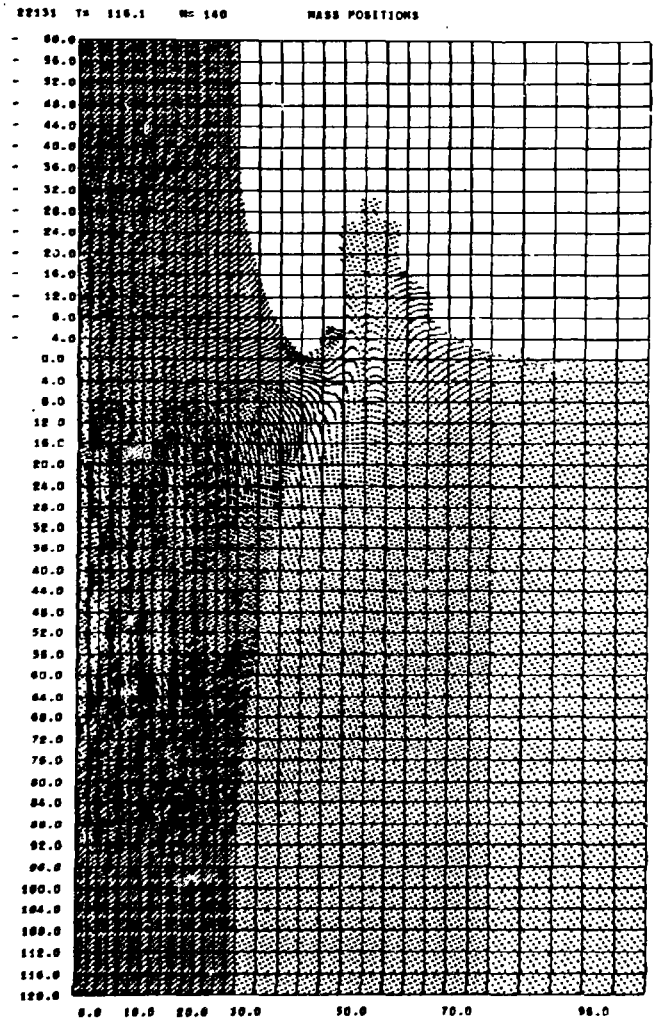
22131 T= 116.1 N= 140
MASS POSITIONS

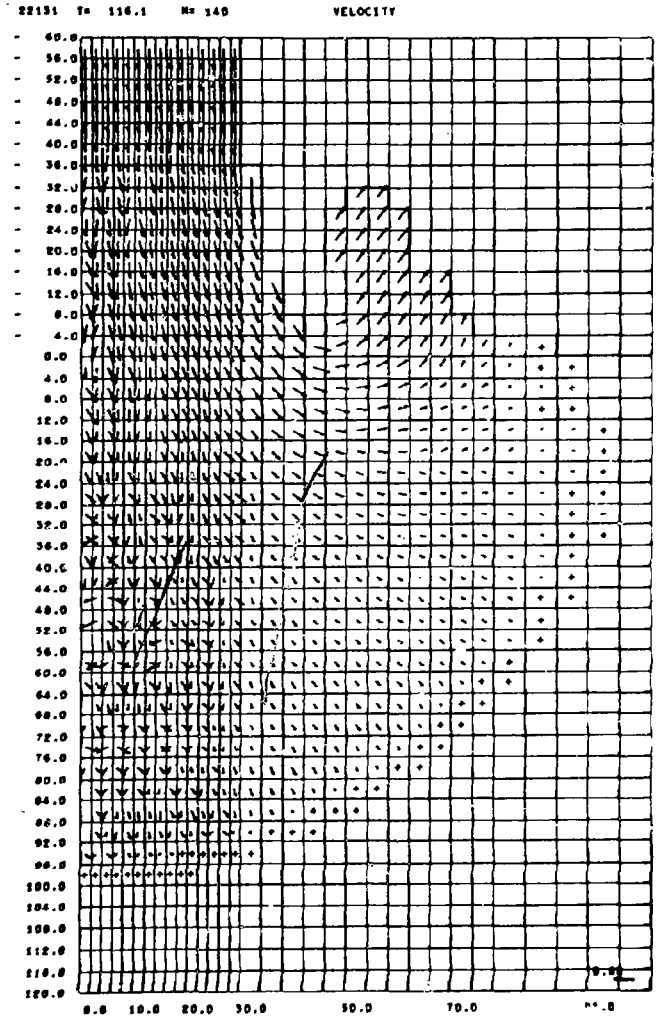
22131 T= 116.1 N= 140
VELOCITY

IMPACT CASE 31: Planar Solution of Al vs Al @ 4.6 km/sec, T/D = 2

Figure A34 (facing): Mass Positions and Velocity Field at 338.9 μsec

The complete sequence of plots for the axisymmetric solution which corresponds to this planar case is found in Figure AI(a) - (o) in Appendix I of reference 1 (pages 63 - 66). The plots in reference 1 were scaled, however, to 1/8-in. dia. projectile rods. For comparisons with reference 1, values of time and length in the planar solution plots must therefore be multiplied by the factor 0.00529116 . . . .

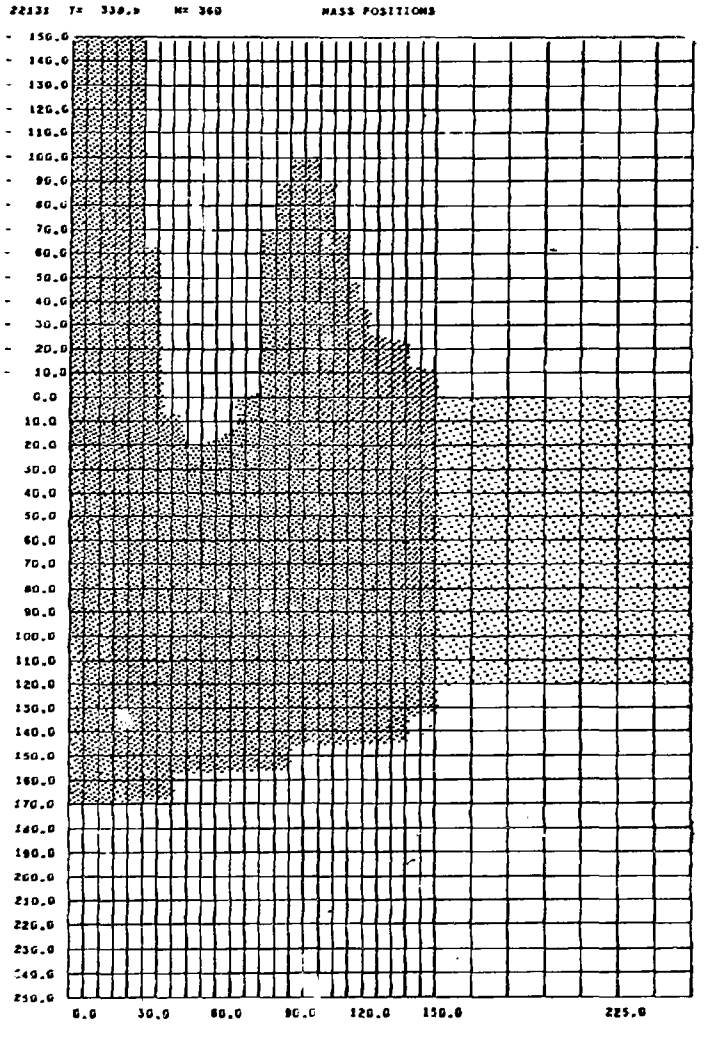
22131 T= 330.0 M= 360
MASS POSITIONS
150.0
140.0
130.0
120.0
110.0
100.0
90.0
80.0
70.0
60.0
50.0
40.0
30.0
20.0
10.0
0.0
10.0
20.0
30.0
40.0
50.0
60.0
70.0
80.0
90.0
100.0
110.0
120.0
130.0
140.0
150.0
160.0
170.0
180.0
190.0
200.0
210.0
220.0
230.0
240.0
250.0
0.0
30.0
60.0
90.0
120.0
150.0
225.0

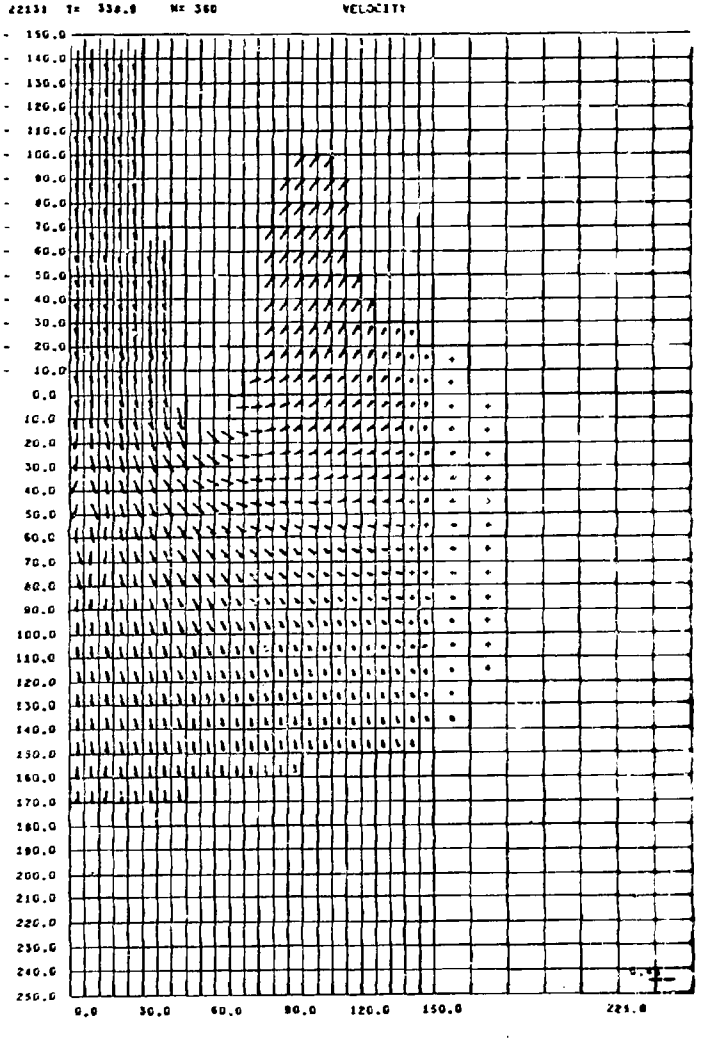
22131 T= 330.0 M= 360
VELOCITY
150.0
140.0
130.0
120.0
110.0
100.0
90.0
80.0
70.0
60.0
50.0
40.0
30.0
20.0
10.0
0.0
10.0
20.0
30.0
40.0
50.0
60.0
70.0
80.0
90.0
100.0
110.0
120.0
130.0
140.0
150.0
160.0
170.0
180.0
190.0
200.0
210.0
220.0
230.0
240.0
250.0
0.0
30.0
60.0
90.0
120.0
150.0
225.0

IMPACT CASE 31: Planar Solution of Al vs Al @ 4.6 km/sec,
T/D = 2

Figure A35 (facing): Mass Positions and Velocity Field at 519.7 μsec

By comparison with Figures AI - 4 (n) and 4(o) in reference 1 (page 66) it is seen that the width of the open hole (or more precisely open slot) is greater than the diameter of the open hole in the axisymmetric case.

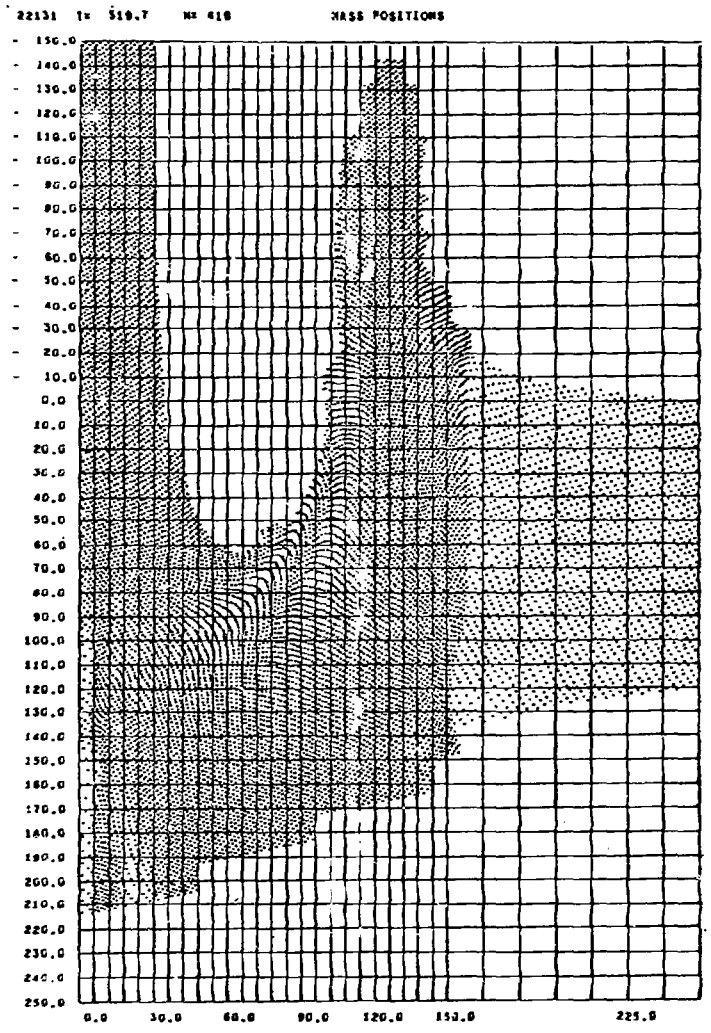
22131 T= 519.7 N= 418
MASS POSITIONS

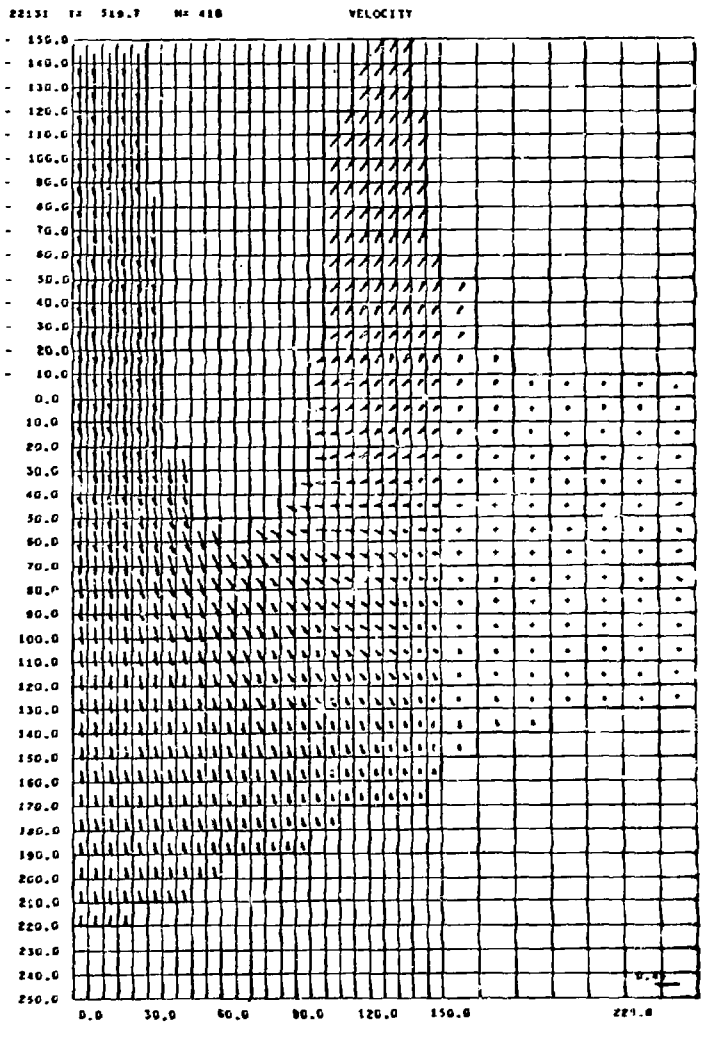
22131 T= 519.7 N= 418
VELOCITY

IMPACT CASE 31: Planar Solution of Al vs Al @ 4.6 km/sec, T/D = 2

Figure A36 (facing): Mass Positions and Velocity Field at 731.8 μsec

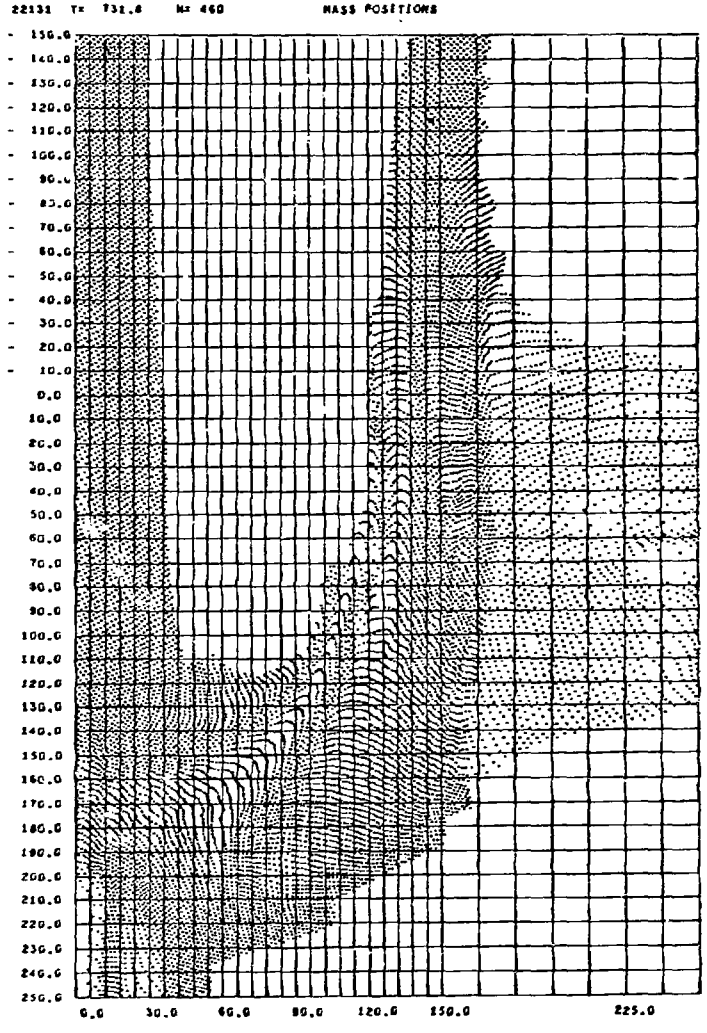
22131 T= 731.8 N= 460
MASS POSITIONS
0.0
30.0
60.0
90.0
120.0
150.0
225.0

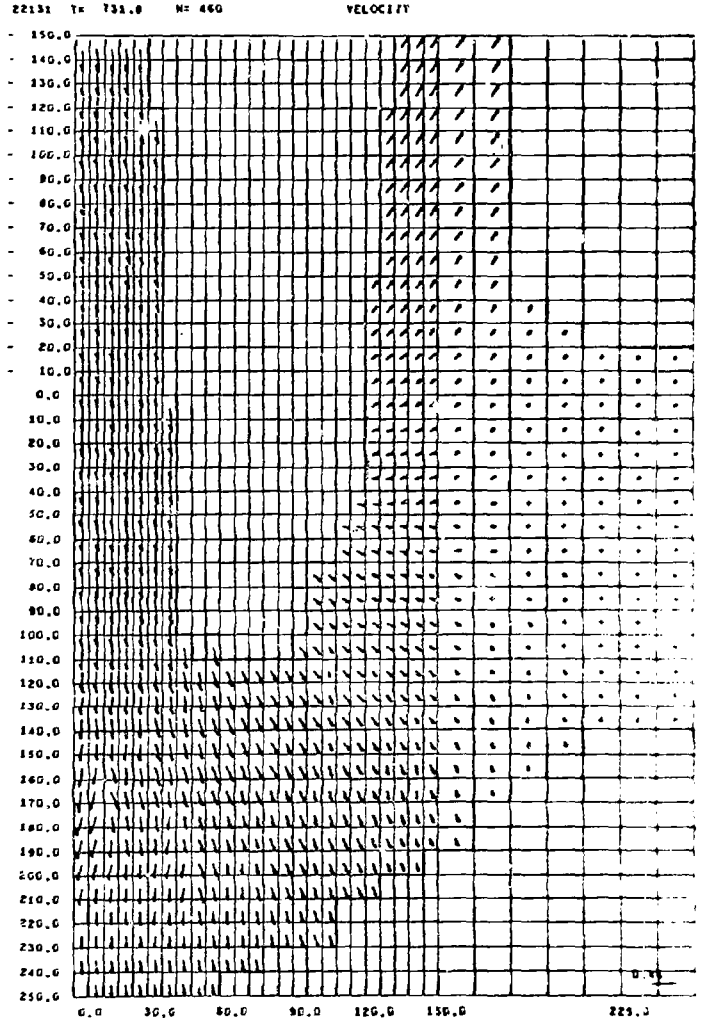
22131 T= 731.8 N= 460
VELOCITY
0.0
30.0
60.0
90.0
120.0
150.0

IMPACT CASE 31: Planar Solution of Al vs Al @ 4.6 km/sec, T/D = 2

Figure A37 (facing): Mass Positions and Velocity Field at 782.8 μsec

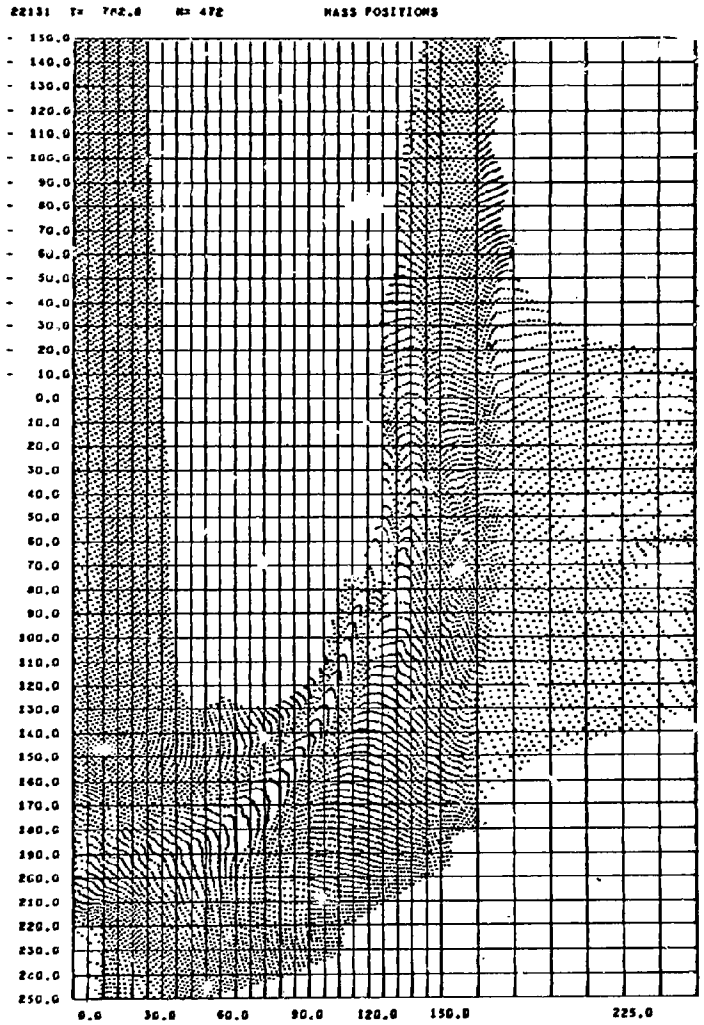
22131 T= 702.8 NX= 472
MASS POSITIONS
0.0
30.0
60.0
90.0
120.0
150.0
225.0

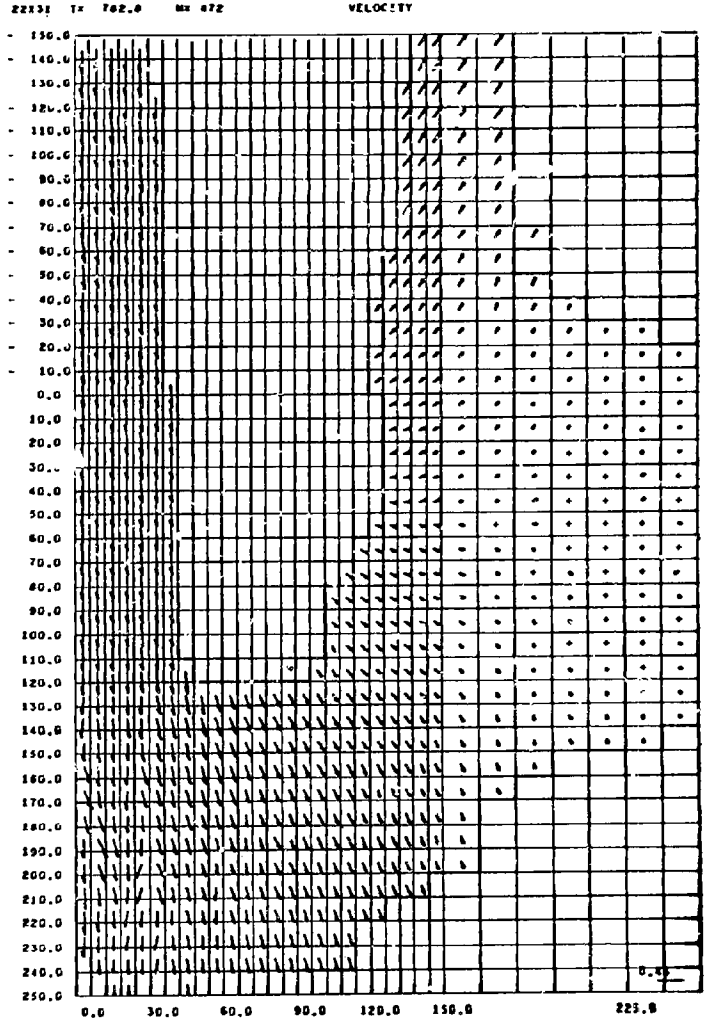
22131 T= 702.8 NX= 472
VELOCITY
0.0
30.0
60.0
90.0
120.0
150.0
225.0

IMPACT CASE 32: Aluminum Plate Projectile vs
Aluminum Plate Target,
30° Oblique Impact at 4.6 km/sec,
(Planar Solution),
Projectile Thickness ("D") = 60 cm,
Target Thickness = 120 cm
(T/D = 2)

Figure A38 (facing): Initial Mass Positions

Analysis of oblique impact of a rod requires use of three spatial dimensions. To reduce such problems to two dimensions, a planar approximation (no z-direction dependence) is used. The solution therefore represents the edge-on impact of an infinitely long plate onto another plate. The plots shown are cross-sections. The projectile center line is at 1030 cm.

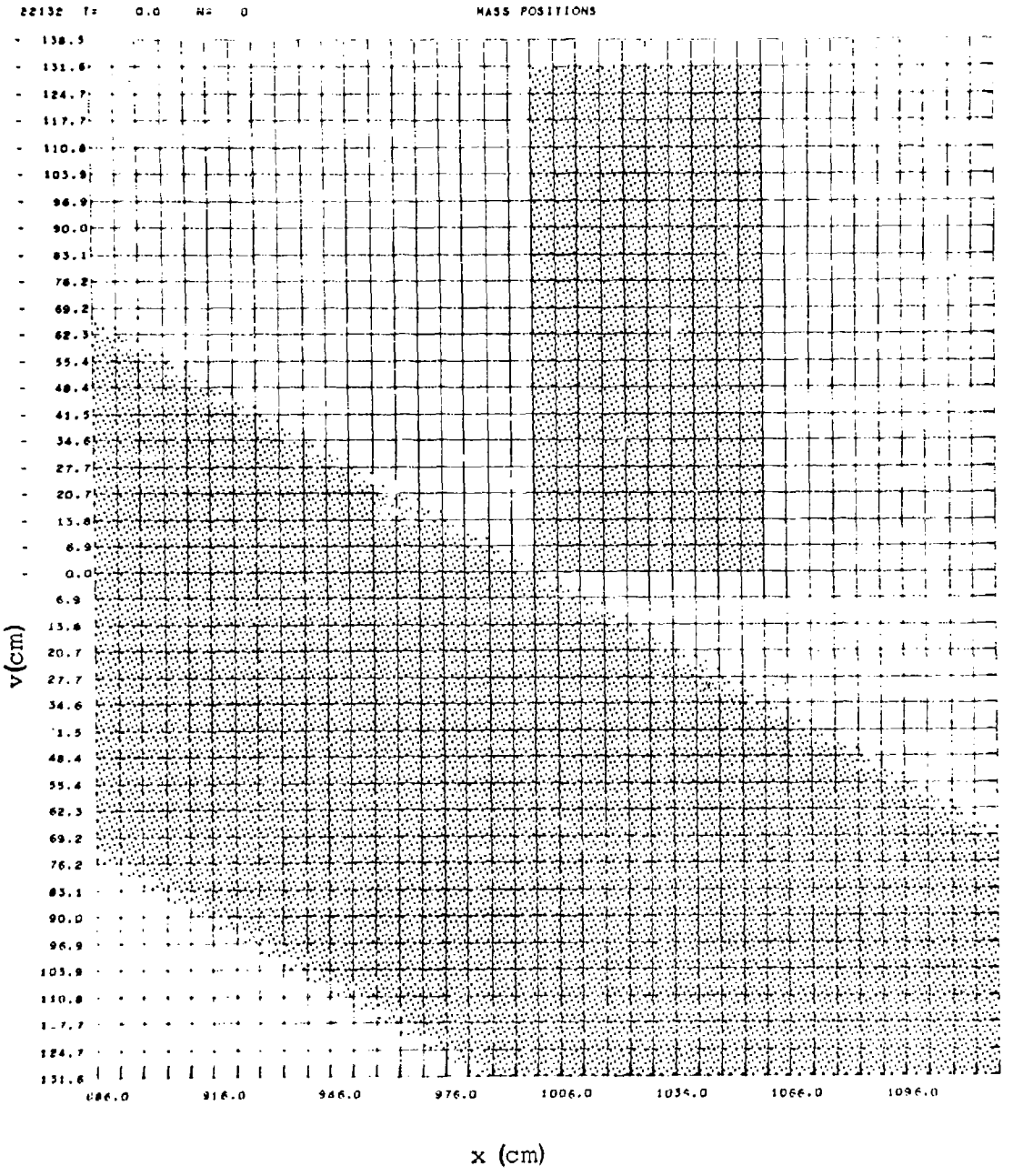
22132 T= 0.0 N= 0
MASS POSITIONS
v(cm)
x (cm)

IMPACT CASE 32: Al vs Al @ 4.6 km/sec, 30° Incidence
(planar solution), T/D = 2

Figure A39 (facing): Mass Positions and Velocity Field at 151.2 μsec

The flow field expands in all directions from the initial impact point. "Downstream", jetting is evident due to the configuration of the free surface.

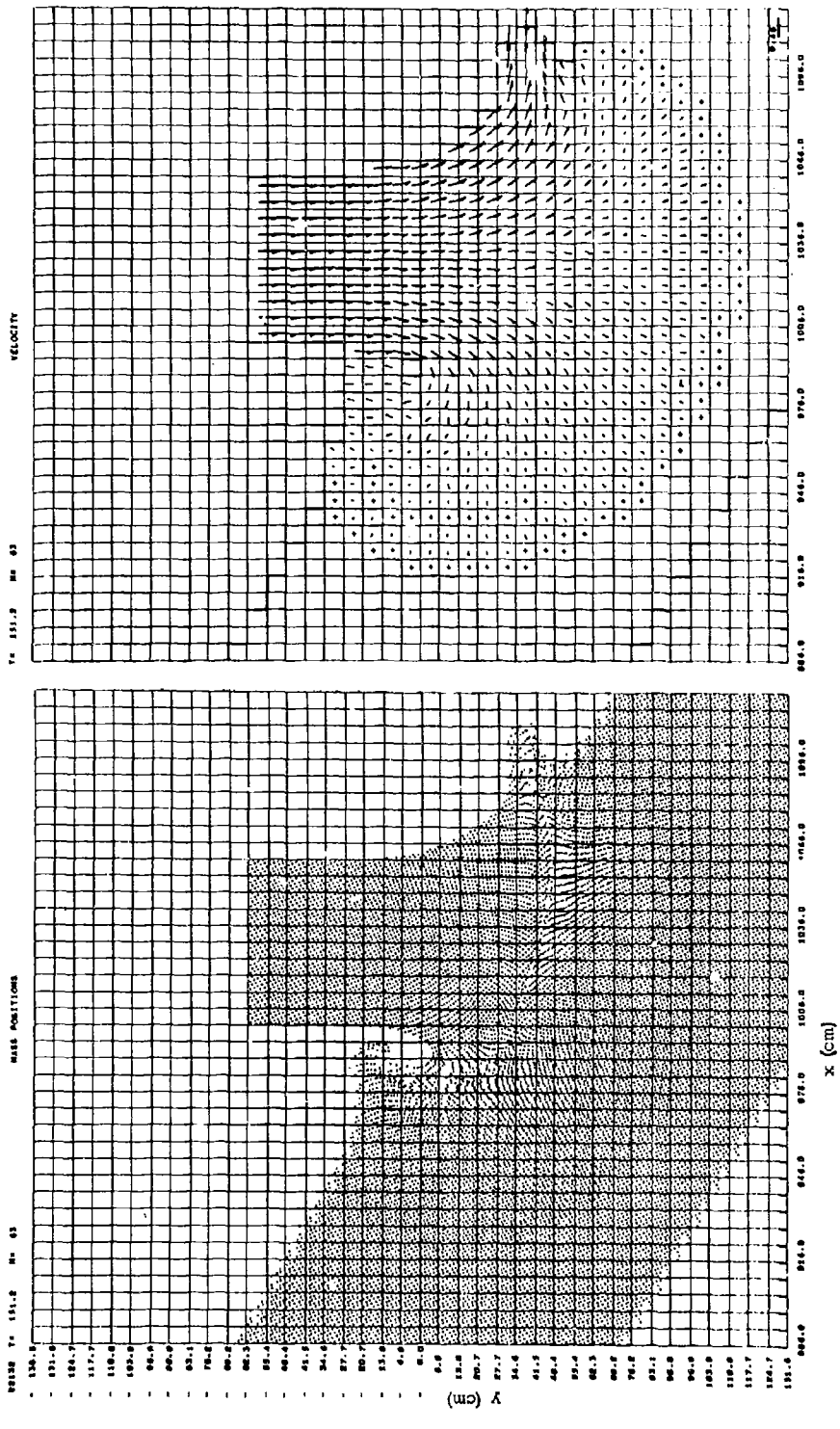
BLOB POSITIONS
VELOCITY
Y (cm)
X (cm)

IMPACT CASE 32: Al vs Al @ 4.6 km/sec, 30° Incidence
(planar solution), T/D = 2

Figure A40 (facing): Mass Positions and Velocity Field at 243.7 μsec

The downstream jet continues to form. Upstream, a weak counterflow develops adjacent to the projectile. Initial deformation of the rear free surface occurs approximately opposite to the impact point (i.e. directly through the plate).

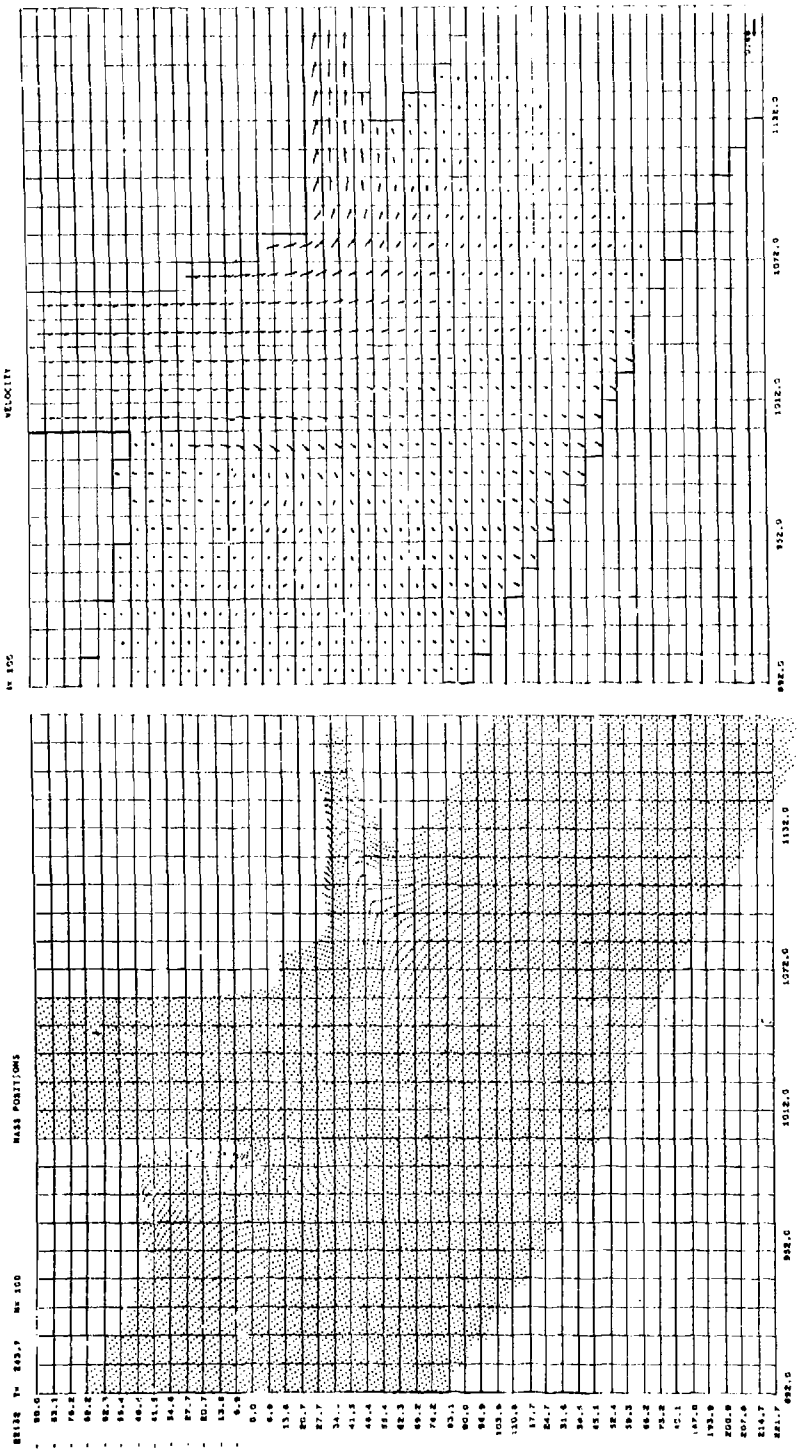
VELOCITY
MASS POSITIONS
1132.0
1072.0
1012.0
952.0
892.0

IMPACT CASE 32: Al vs Al @ 4.6 km/sec, 30° Incidence
(Planar Solution), T/D = 2

Figure A41 (facing): Mass Positions at 393.7 and 601.2 μsec

The flow field characteristics are well-developed in these plots. The leading edge of the projectile is blunted, and transverse flow is occurring at the "stagnation point". The initial downstream jet is just moving out of the field of view. Upstream, the counterflowing mass is moving parallel to the surface of the projectile, leaving an intermediate void near the leading edge.

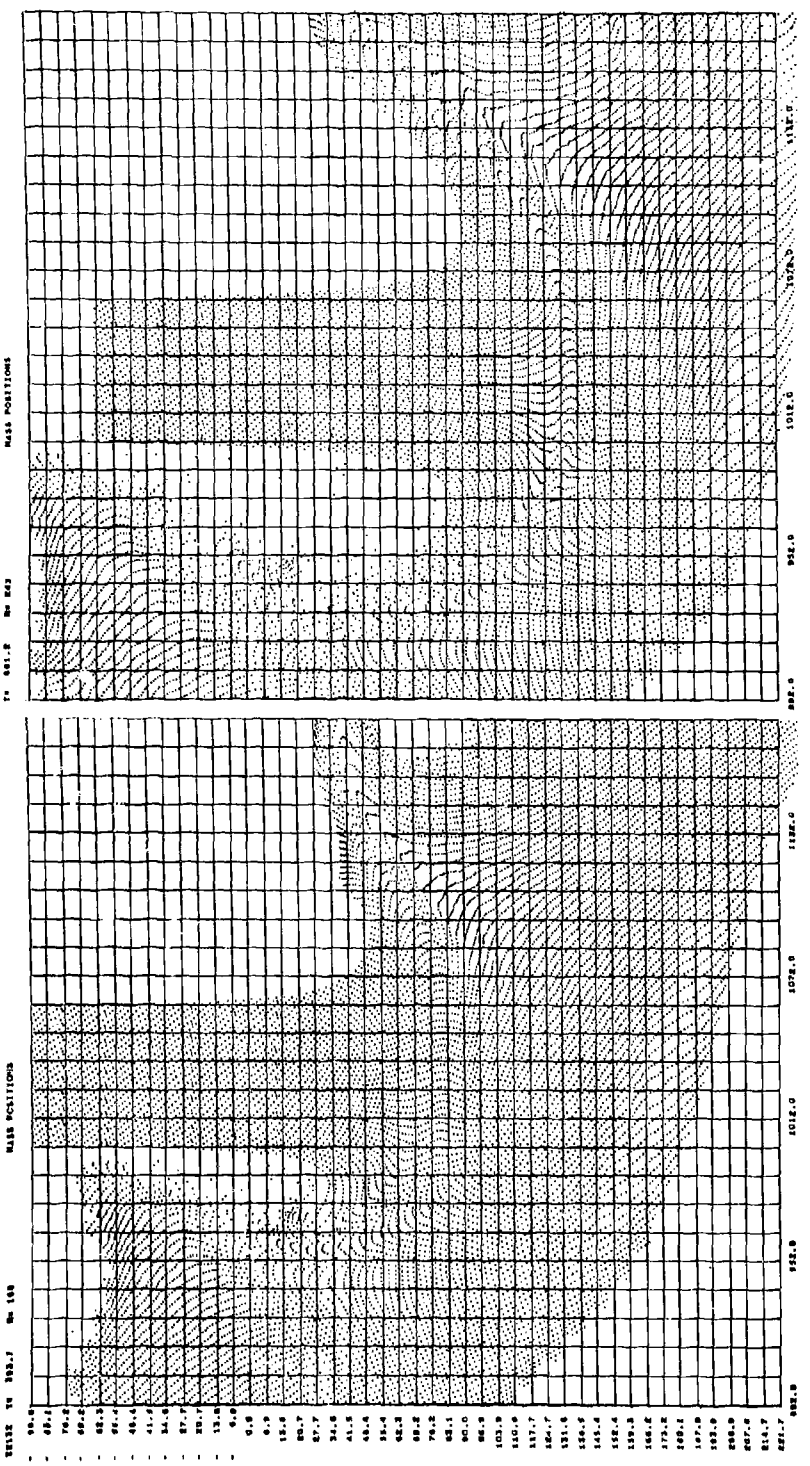

IMPACT CASE 32: Al vs Al @ 4.6 km/sec, 30° Incidence
(Planar Solution), T/D = 2

Figure A42 (facing): Mass Positions and Velocity Field at 724.7 μsec

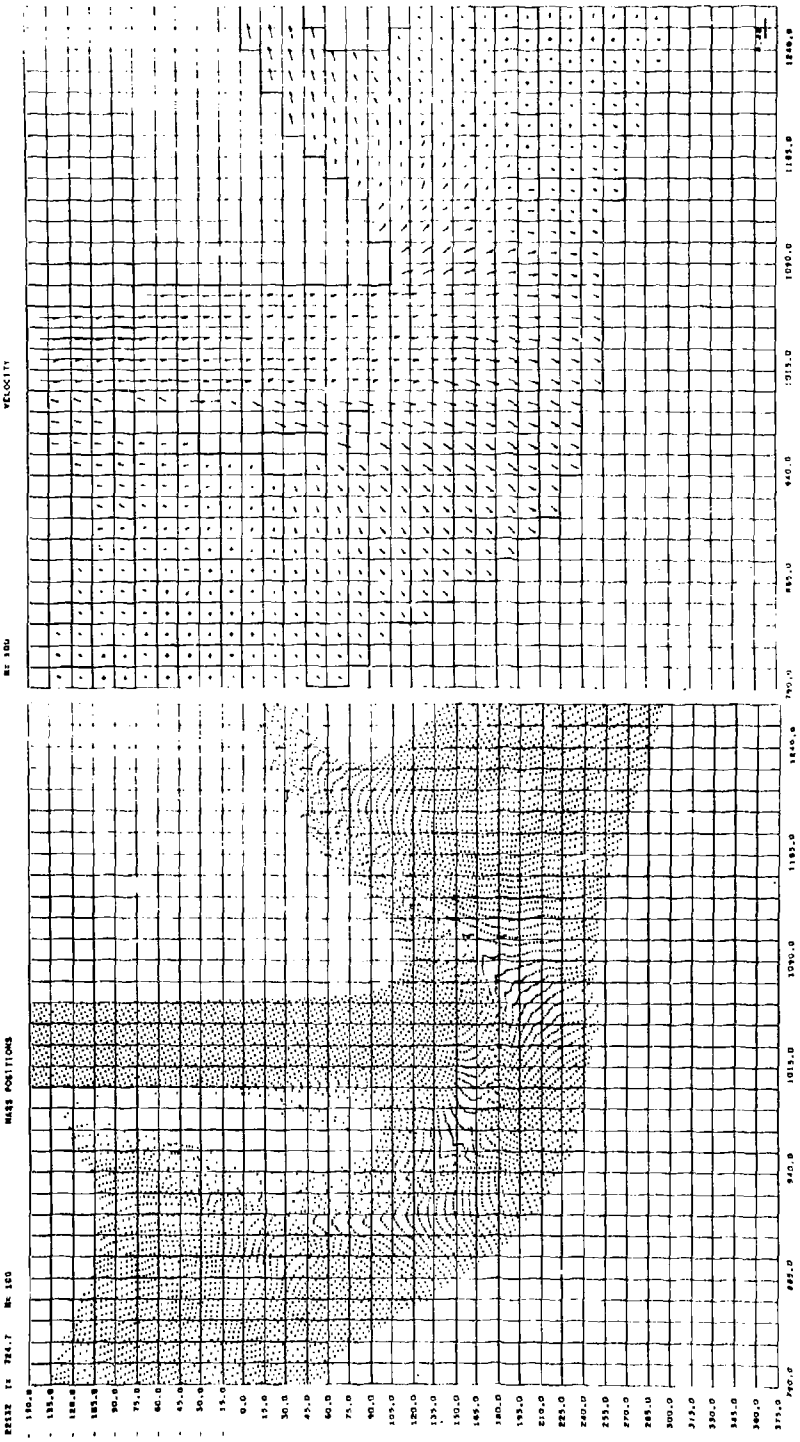
MASS POSITIONS
VELOCITY

IMPACT CASE 32: Al vs Al @ 4.6 km/sec, 30° Incidence
(Planar Solution), T/D = 2

Figure A43 (facing): Mass Positions and Velocity Field at 1017.7 μsec

Perforation is nearly complete, in that the remaining target material ahead of the projectile is moving at nearly the impact velocity.

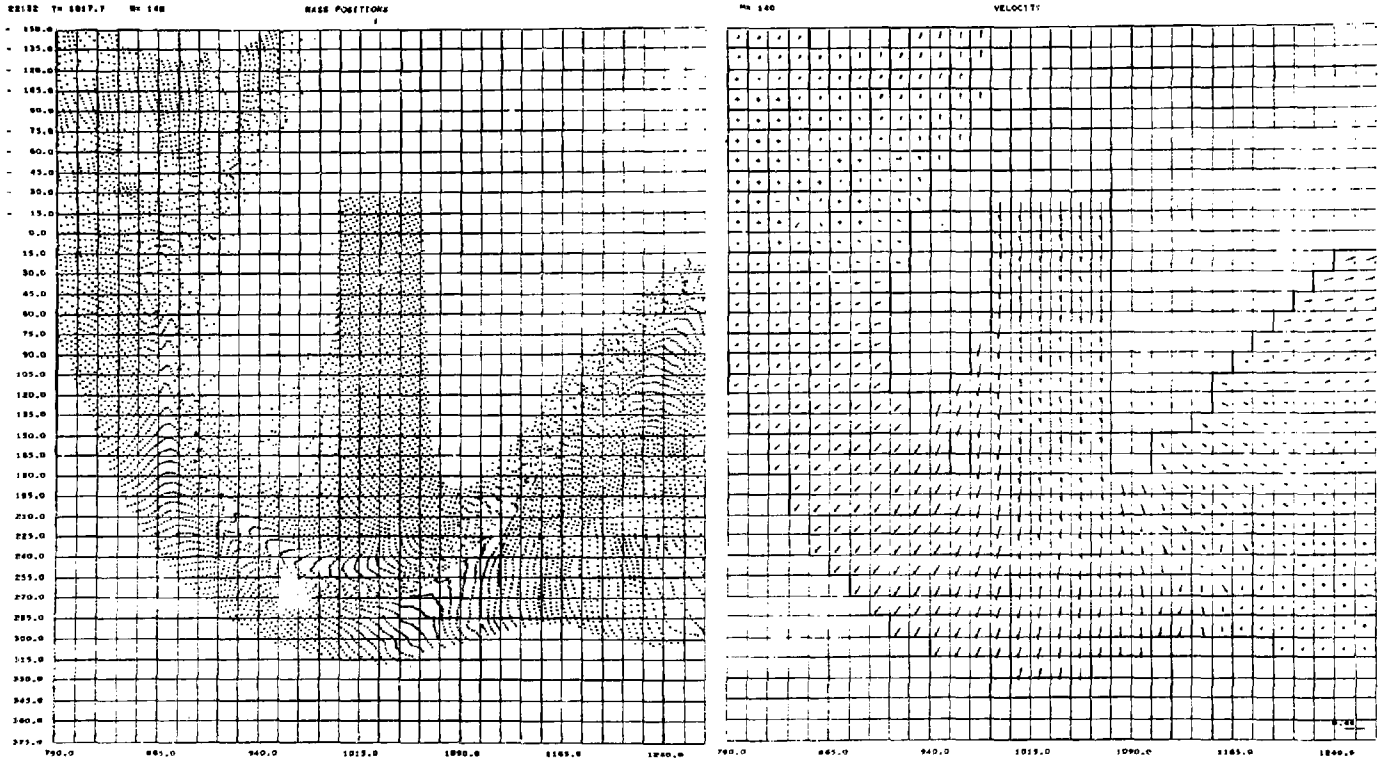
MASS POSITIONS
VELOCITY

IMPACT CASE 33: Aluminum Plate Projectile vs Aluminum Plate Target,
60° Oblique Impact at 4.6 km/sec (Planar Solution),
Projectile Thickness ("D") = 60 cm,
Target Thickness = 120 cm (T/D = 2)

Figure A44 (facing): Mass Positions and Velocity Field at 25 μsec

As in Case 32, the planar approximation is used to represent oblique impact of a rod. In these plots at 25 μsec, the very early interactions of the projectile corner with the target are seen.

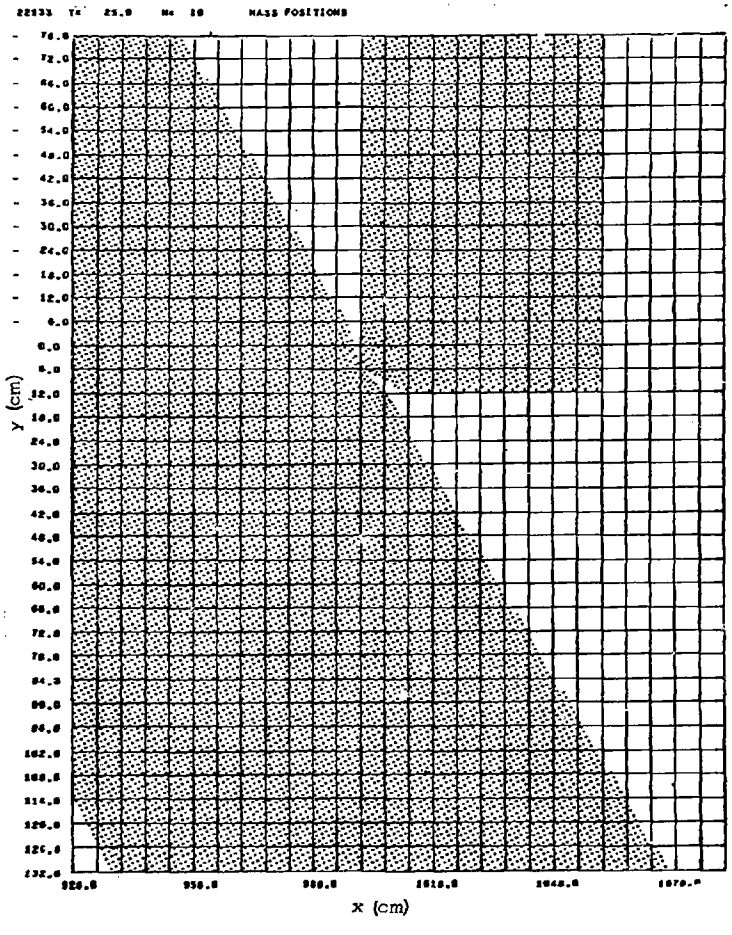
MASS POSITIONS
y (cm)
x (cm)

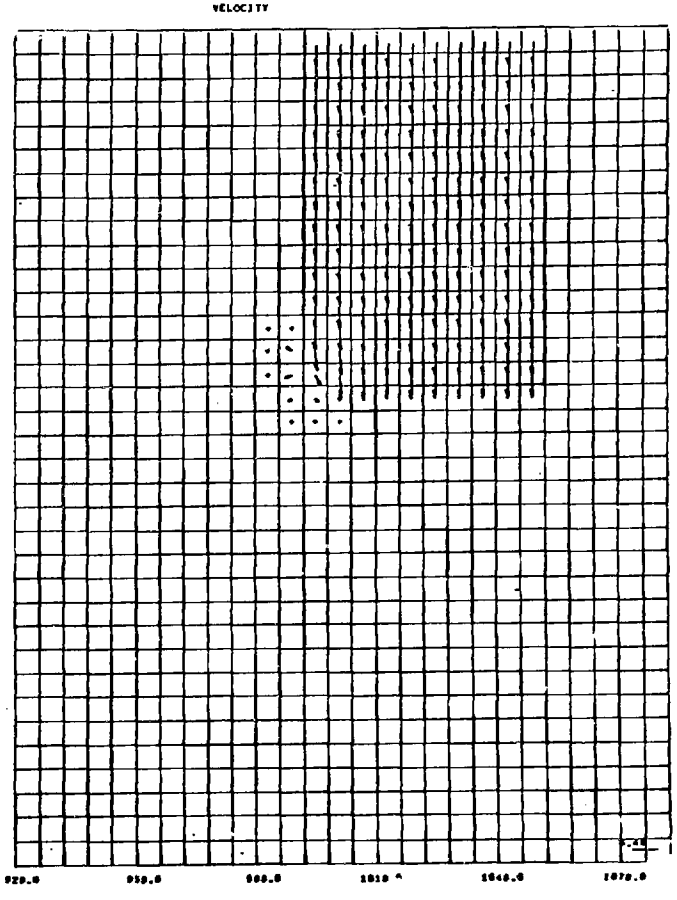
VELOCITY

IMPACT CASE 33: Al vs Al @ 4.6 km/sec, 60° Incidence,
(Planar Solution) T/D = 2

Figure A45 (facing): Mass Positions and Velocity Field at 175 μsec

Strong jetting is occuring roughly parallel to the target surface downstream. Upstream, the target surface is raising slowly. (Note the upstream surface position relative to the initial pcint of contact at y = 0, x = 1000 .)

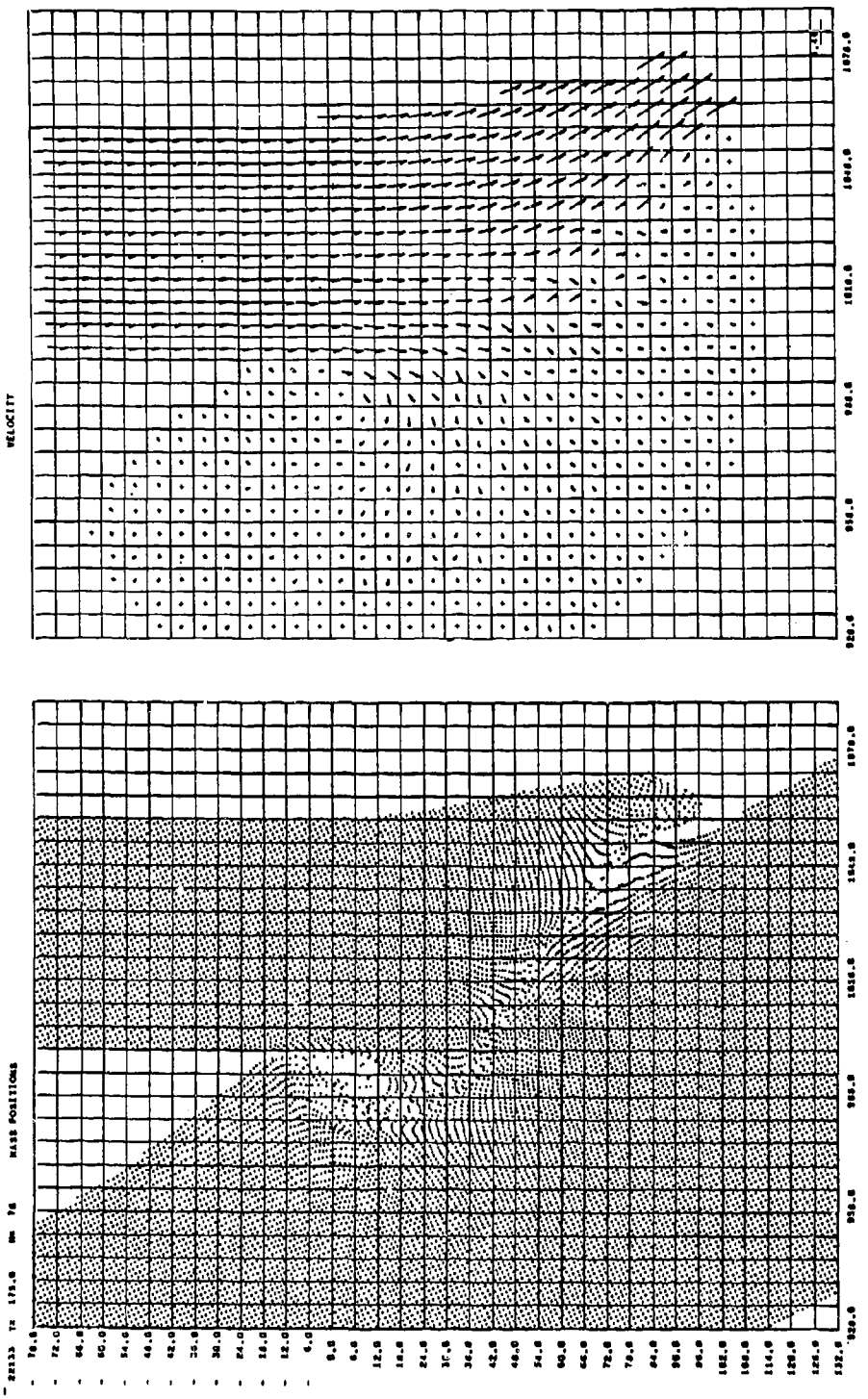
VELOCITY
MASS POSITIONS

IMPACT CASE 33: Al vs Al @ 4.6 km/sec, 60° Incidence
(Planar Solution) $T/D = .2$

Figure A46 (facing): Mass Positions and Velocity Field at 416.3 μsec

Initial deformation of the rear surface occurs only slightly downstream from a position approximately opposite from the initial point of contact at y = 0, x = 1000. Deformation along the line of flight does not occur until much later.

The downstream jetting along the front surface involves flow of a substantial fraction, (perhaps a third) of the incoming projectile mass at this time.

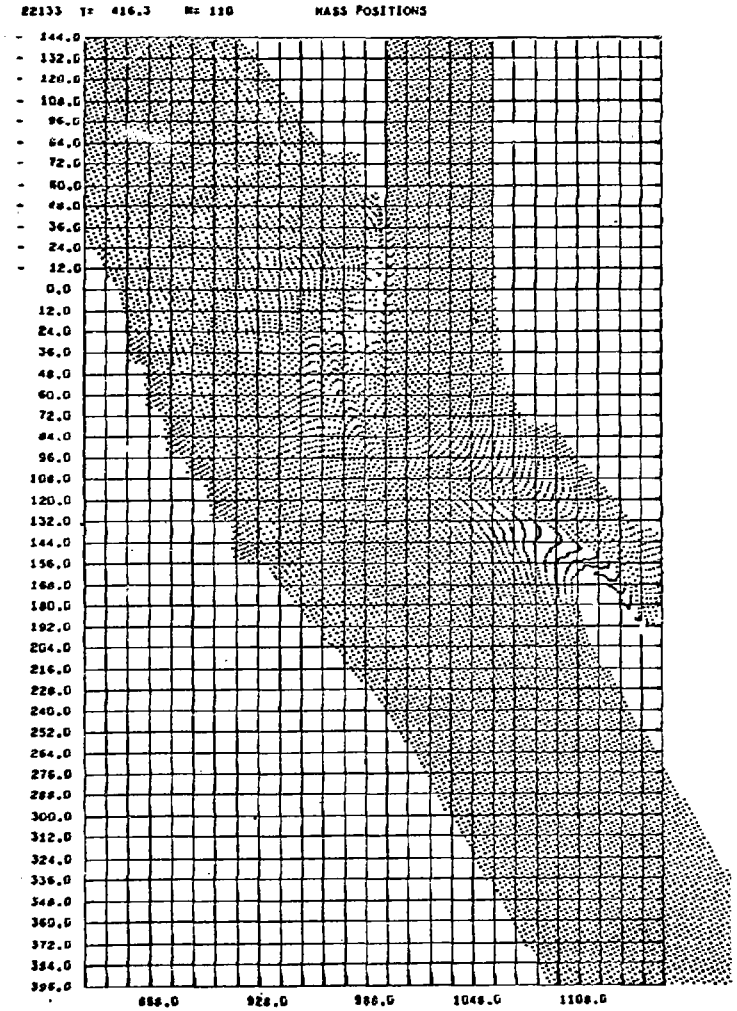
22133 T= 416.3 N= 110
MASS POSITIONS
144.0
132.0
120.0
108.0
96.0
84.0
72.0
60.0
48.0
36.0
24.0
12.0
0.0
12.0
24.0
36.0
48.0
60.0
72.0
84.0
96.0
108.0
120.0
132.0
144.0
156.0
168.0
180.0
192.0
204.0
216.0
228.0
240.0
252.0
264.0
276.0
288.0
300.0
312.0
324.0
336.0
348.0
360.0
372.0
384.0
396.0
868.0
928.0
988.0
1048.0
1108.0

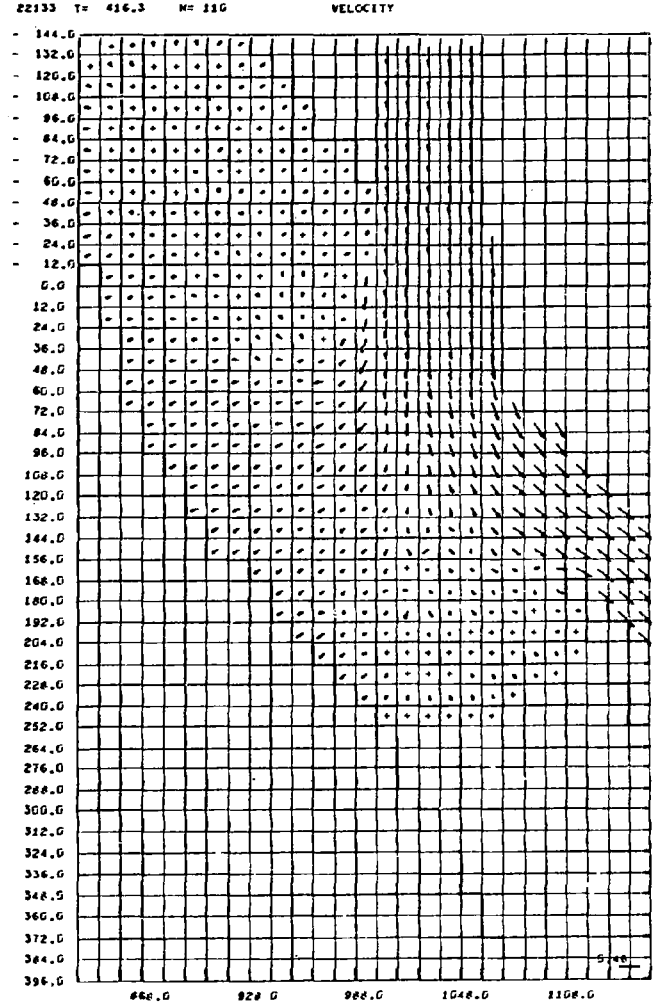
22133 T= 416.3 N= 110
VELOCITY
144.0
132.0
120.0
108.0
96.0
84.0
72.0
60.0
48.0
36.0
24.0
12.0
0.0
12.0
24.0
36.0
48.0
60.0
72.0
84.0
96.0
108.0
120.0
132.0
144.0
156.0
168.0
180.0
192.0
204.0
216.0
228.0
240.0
252.0
264.0
276.0
288.0
300.0
312.0
324.0
336.0
348.0
360.0
372.0
384.0
396.0
868.0
928.0
988.0
1048.0
1108.0

IMPACT CASE 33: Al vs Al @ 4.6 km/sec, 60^{O} Incidence
(Planar Solution), T/D = 2

Figure A47 (facing): Mass Positions at 568.9 and 721.5 μsec

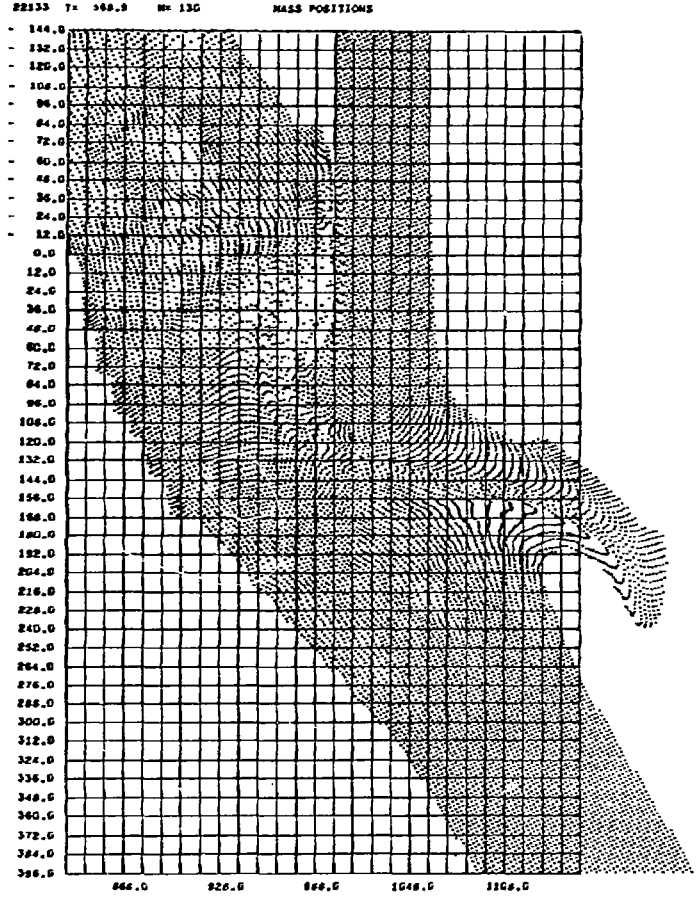
22133 T= 568.8 N= 13G MASS POSITIONS
144.0
132.0
120.0
108.0
96.0
84.0
72.0
60.0
48.0
36.0
24.0
12.0
0.0
12.0
24.0
36.0
48.0
60.0
72.0
84.0
96.0
108.0
120.0
132.0
144.0
156.0
168.0
180.0
192.0
204.0
216.0
228.0
240.0
252.0
264.0
276.0
288.0
300.0
312.0
324.0
336.0
348.0
360.0
372.0
384.0
396.0
868.0
928.0
988.0
1048.0
1108.0

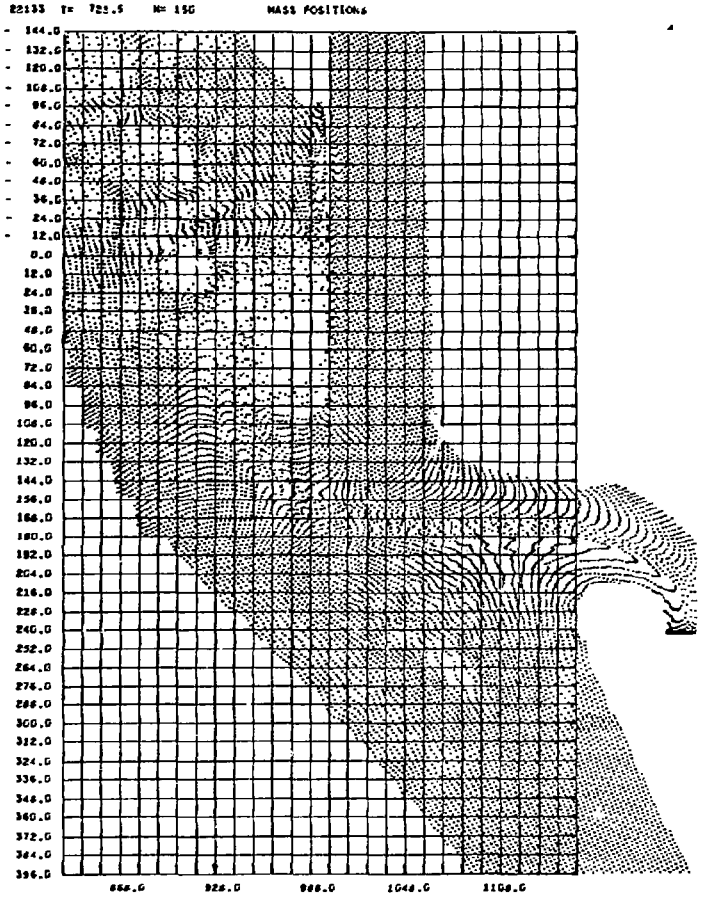
22133 T= 721.5 N= 15G MASS POSITIONS
144.0
132.0
120.0
108.0
96.0
84.0
72.0
60.0
48.0
36.0
24.0
12.0
0.0
12.0
24.0
36.0
48.0
60.0
72.0
84.0
96.0
108.0
120.0
132.0
144.0
156.0
168.0
180.0
192.0
204.0
216.0
228.0
240.0
252.0
264.0
276.0
288.0
300.0
312.0
324.0
336.0
348.0
360.0
372.0
384.0
396.0
868.0
928.0
988.0
1048.0
1108.0

IMPACT CASE 33: Al vs Al @ 4.6 km/sec,
60° Incidence (Planar Solution),
T/D = 2

Figure A48 (facing): Mass Positions and Velocity Field at 1026.7 μsec

These plots show the position of the rear surface of the projectile. (In prior plots, inactive portions of the projectile have been omitted to conserve the field of view.)

Interactions between the rising upstream target surface and the side of the projectile have caused some deflection of the projectile. A weak vortex motion has occurred where target material folded up and back against the projectile and is then accelerated downward again.

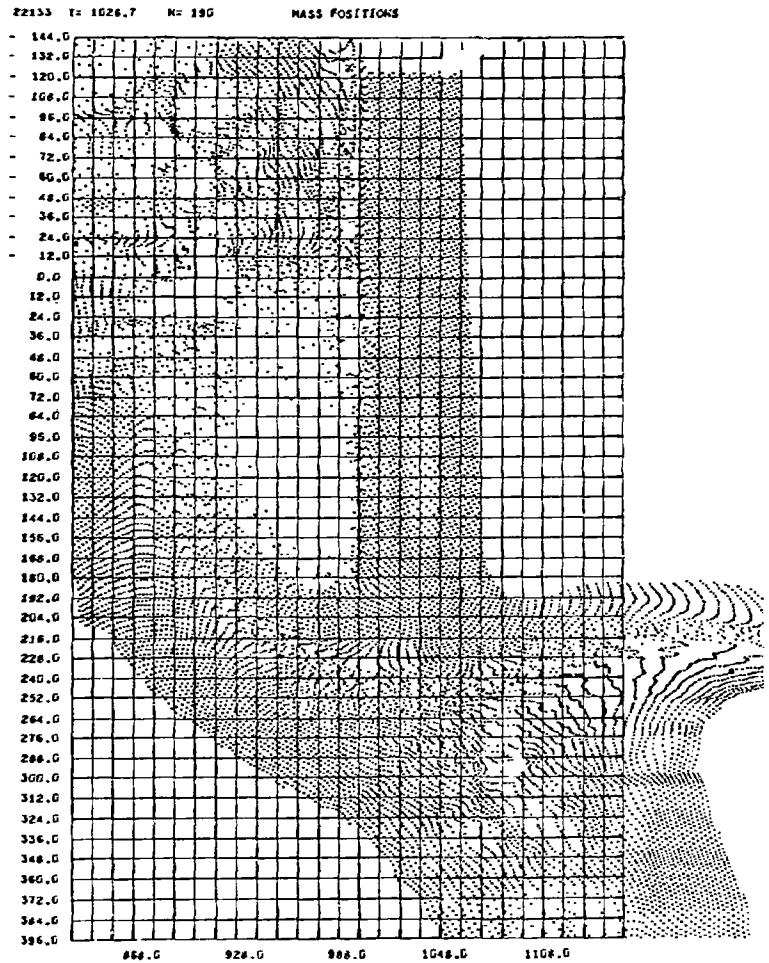
22133 T= 1026.7 N= 190
MASS POSITIONS
144.0
132.0
120.0
108.0
96.0
84.0
72.0
60.0
48.0
36.0
24.0
12.0
0.0
12.0
24.0
36.0
48.0
60.0
72.0
84.0
96.0
108.0
120.0
132.0
144.0
156.0
168.0
180.0
192.0
204.0
216.0
228.0
240.0
252.0
264.0
276.0
288.0
300.0
312.0
324.0
336.0
348.0
360.0
372.0
384.0
396.0
868.0
928.0
988.0
1048.0
1108.0

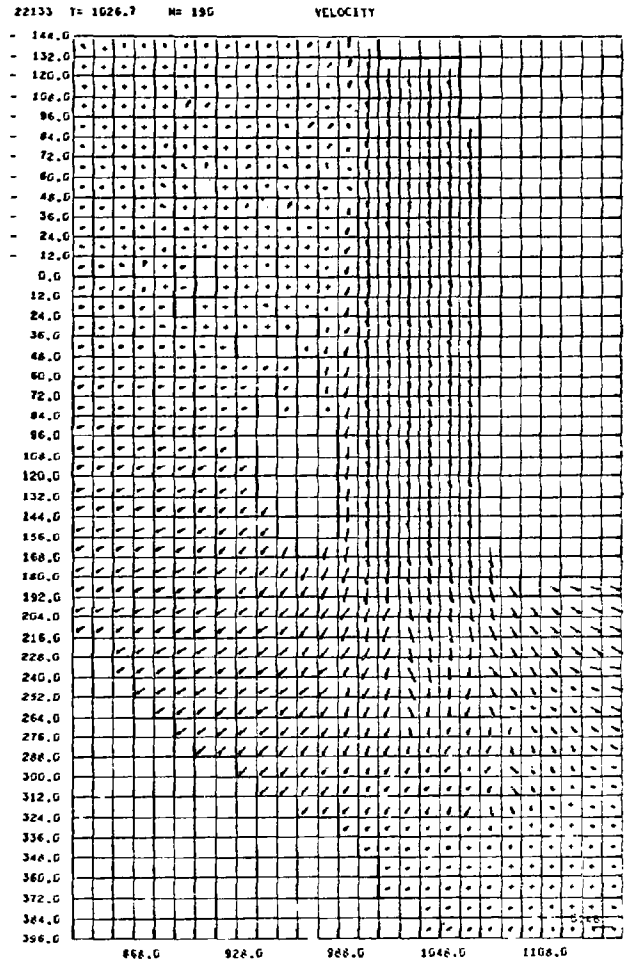
22133 T= 1026.7 N= 190
VELOCITY
144.0
132.0
120.0
108.0
96.0
84.0
72.0
60.0
48.0
36.0
24.0
12.0
0.0
12.0
24.0
36.0
48.0
60.0
72.0
84.0
96.0
108.0
120.0
132.0
144.0
156.0
168.0
180.0
192.0
204.0
216.0
228.0
240.0
252.0
264.0
276.0
288.0
300.0
312.0
324.0
336.0
348.0
360.0
372.0
384.0
396.0
868.0
928.0
988.0
1048.0
1108.0

IMPACT CASE 33: Al vs Al @ 4.6 km/sec,
60° incidence (Planar Solution),
T/D = 2

Figure A49 (facing): Mass Positions and Velocity Field at 1331.9 μsec

Several features are of interest in this plot. It is seen that the open holes (slots) are at the same depth on the upstream and downstream side of the projectile. On the upstream side, the open hole extends well beyond the original rear surface of the target plate. However, an appreciable target mass remains ahead of the projectile. While this residual mass has been accelerated to a significant fraction of the impact velocity, continuing interactions can be expected to cause additional projectile loss during the break-through phase. It is also interesting to note that the projectile mass has been displaced by about one cell width in the downstream direction (to the right).

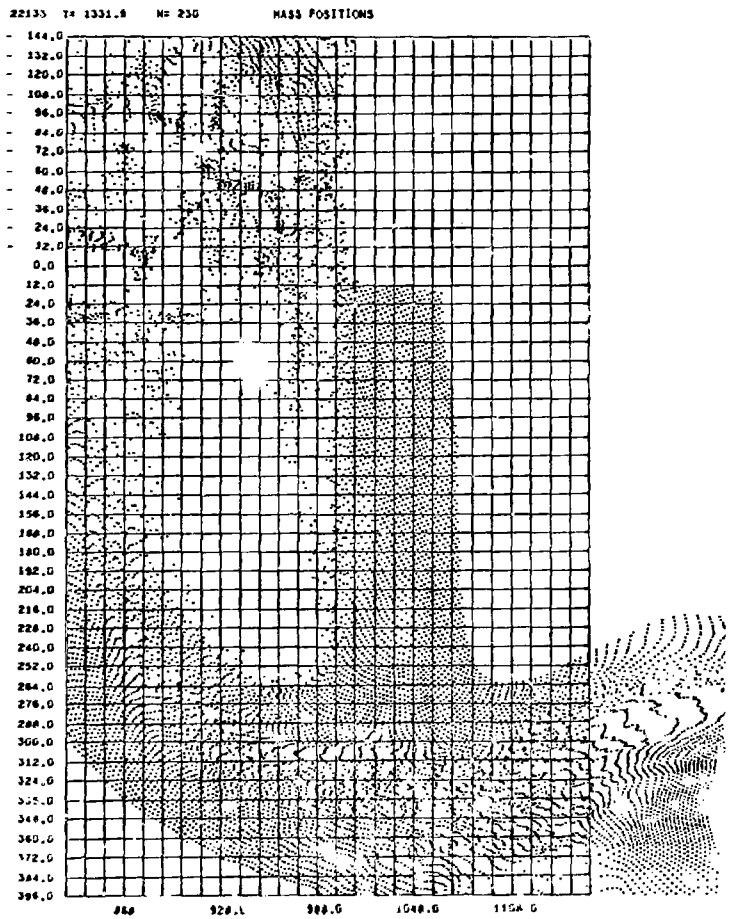
22133 T= 1331.8 N= 230 MASS POSITIONS

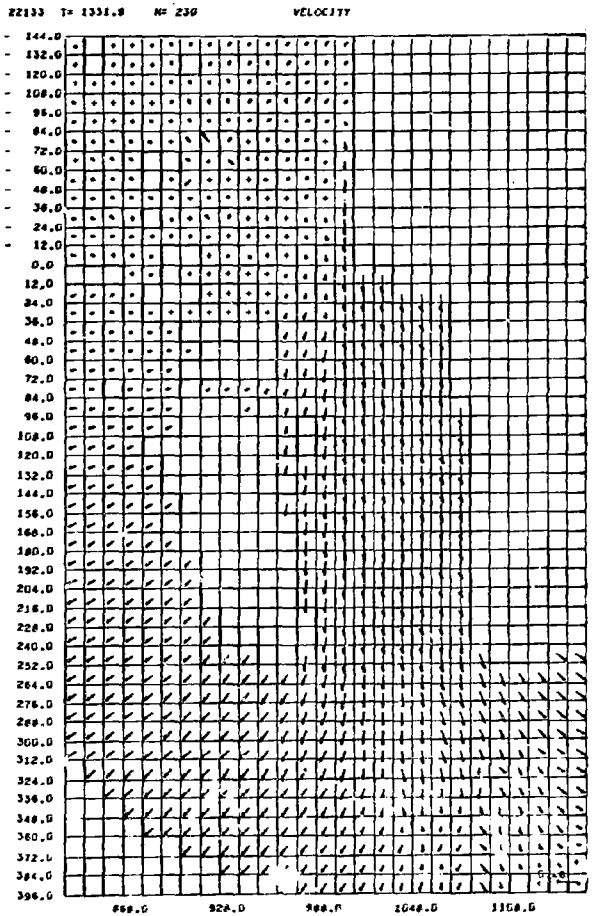
22133 T= 1331.8 N= 230 VELOCITY

UNCLASSIFIED

Security Classification

DOCUMENT CONTROL DATA - R & D

(Security classification of title, body of abstract and indexing annotation must be entered when the overall report is classified)

1. ORIGINATING ACTIVITY (Corporate author)	2a. REPORT SECURITY CLASSIFICATION
Naval Research Laboratory Washington, D.C. 20390	Confidential
	2b. GROUP 4

3. REPORT TITLE

FINAL REPORT - HYPERVELOCITY IMPACT OF RODS ON FINITE TARGETS

4. DESCRIPTIVE NOTES (Type of report and inclusive dates)

Report to NRL by Shock Hydrodynamics, Inc., Sherman Oaks, Calif.

5. AUTHOR(S) (First name, middle initial, last name)

M. Rosenblatt, K.N. Kreyenhagen, and R.L. Bjork of Shock Hydrodynamics, Inc.

6. REPORT DATE	7a. TOTAL NO. OF PAGES	7b. NO. OF REFS
May 1968	160	6

8a. CONTRACT OR GRANT NO.	9a. ORIGINATOR'S REPORT NUMBER(S)
NONR 4221(00)(X) b. PROJECT NO. AF Project 9850 c. MIPR PG-3-15 d.	NRL Report 6743 9b. OTHER REPORT NO(S) (Any other numbers that may be assigned this report) AFATL-TR-68-59

10. DISTRIBUTION STATEMENT In addition to security requirements which apply to this document and must be met, each transmittal outside the agencies of the U.S. Government must have prior approval of the Director, Naval Research Laboratory, Washington, D.C. 20390.

11. SUPPLEMENTARY NOTES	12. SPONSORING MILITARY ACTIVITY
Research and report carried out by Shock Hydrodynamics, Inc.; report compared, printed, and distributed by the Naval Research Laboratory.	Department of the Air Force, Air Force Armament Laboratory, Eglin AFB, Florida 32542

13. ABSTRACT

(Unclassified)

An analytical study has been performed concerning the impact of end-oriented aluminum and iron rods against aluminum plates of various thicknesses at velocities of 4.6 and 6.1 km/sec (15,000 and 20,000 ft/sec). A hydrodynamic model was used in these analyses, utilizing the two-dimensional particle-in-cell code to provide numerical solutions. Plots of these solutions show the development of the shock wave systems in the rods and the target plates, and the resulting plate perforation and loss of rod length. Equations are developed relating the amount of rod loss to the quantities characterizing the impact configuration, e.g., impact velocity, material density, target thickness.

DD FORM 1 NOV 65 1473 (PAGE 1)

S/N 0101-807-6801

UNCLASSIFIED

Security Classification

14. KEY WORDS	LINK A		LINK B		LINK C	
	ROLE	WT	ROLE	WT	ROLE	WT
Hypervelocity rod impact Hypervelocity projectiles Aluminum rod projectiles Iron rod projectiles Ballistic properties of end-oriented rods						

UNCLASSIFIED

Naval Research Laboratory. Report 6743 [CONFIDENTIAL-Gp-4]. FINAL REPORT - HYPERVELOCITY IMPACT OF RODS ON FINITE TARGETS [Unclassified Title], by M. Rosenblatt, K. N. Kreyenhagen, and R.L. Bjork. 160 pp. and figs., May 1968.

An analytical study has been performed concerning the impact of end-oriented aluminum and iron rods against aluminum plates of various thicknesses at velocities of 4.6 and 6.1 km/sec (15,000 and 20,000 ft/sec). A hydrodynamic model was used in these analyses, utilizing the two-dimensional particle-in-cell code to provide numerical solutions. Plots of these solutions show the development of the shock wave systems in the rods and the target plates, and the resulting plate

UNCLASSIFIED (over)

1. Hypervelocity projectiles - materials research
2. Iron - Ballistic prop.
3. Aluminum - Ballistic prop.

I. Rosenblatt, M.

II. Kreyenhagen, K. N.

III. Bjork, R. L.

UNCLASSIFIED

Naval Research Laboratory. Report 6743 [CONFIDENTIAL-Gp-4]. FINAL REPORT - HYPERVELOCITY IMPACT OF RODS ON FINITE TARGETS [Unclassified Title], by M. Rosenblatt, K. N. Kreyenhagen, and R.L. Bjork. 160 pp. and figs., May 1968.

An analytical study has been performed concerning the impact of end-oriented aluminum and iron rods against aluminum plates of various thicknesses at velocities of 4.6 and 6.1 km/sec (15,000 and 20,000 ft/sec). A hydrodynamic model was used in these analyses, utilizing the two-dimensional particle-in-cell code to provide numerical solutions. Plots of these solutions show the development of the shock wave systems in the rods and the target plates, and the resulting plate

UNCLASSIFIED (over)

1. Hypervelocity projectiles - materials research
2. Iron - Ballistic prop.
3. Aluminum - Ballistic prop.

I. Rosenblatt, M.

II. Kreyenhagen, K. N.

III. Bjork, R. L.

UNCLASSIFIED

Naval Research Laboratory. Report 6743 [CONFIDENTIAL-Gp-4]. FINAL REPORT - HYPERVELOCITY IMPACT OF RODS ON FINITE TARGETS [Unclassified Title], by M. Rosenblatt, K. N. Kreyenhagen, and R.L. Bjork. 160 pp. and figs., May 1968.

An analytical study has been performed concerning the impact of end-oriented aluminum and iron rods against aluminum plates of various thicknesses at velocities of 4.6 and 6.1 km/sec (15,000 and 20,000 ft/sec). A hydrodynamic model was used in these analyses, utilizing the two-dimensional particle-in-cell code to provide numerical solutions. Plots of these solutions show the development of the shock wave systems in the rods and the target plates, and the resulting plate

UNCLASSIFIED (over)

1. Hypervelocity projectiles - materials research
2. Iron - Ballistic prop.
3. Aluminum - Ballistic prop.

I. Rosenblatt, M.

II. Kreyenhagen, K. N.

III. Bjork, R. L.

UNCLASSIFIED

Naval Research Laboratory. Report 6743 [CONFIDENTIAL-Gp-4]. FINAL REPORT - HYPERVELOCITY IMPACT OF RODS ON FINITE TARGETS [Unclassified Title], by M. Rosenblatt, K. N. Kreyenhagen, and R.L. Bjork. 160 pp. and figs., May 1968.

An analytical study has been performed concerning the impact of end-oriented aluminum and iron rods against aluminum plates of various thicknesses at velocities of 4.6 and 6.1 km/sec (15,000 and 20,000 ft/sec). A hydrodynamic model was used in these analyses, utilizing the two-dimensional particle-in-cell code to provide numerical solutions. Plots of these solutions show the development of the shock wave systems in the rods and the target plates, and the resulting plate

UNCLASSIFIED (over)

1. Hypervelocity projectiles - materials research
2. Iron - Ballistic prop.
3. Aluminum - Ballistic prop.

I. Rosenblatt, M.

II. Kreyenhagen, K. N.

III. Bjork, R. L.

perforation and loss of rod length. Equations are developed relating the amount of rod loss to the quantities characterizing the impact configuration, e.g., impact velocity, material density, target thickness.

UNCLASSIFIED

perforation and loss of rod length. Equations are developed relating the amount of rod loss to the quantities characterizing the impact configuration, e.g., impact velocity, material density, target thickness.

UNCLASSIFIED

UNCLASSIFIED

perforation and loss of rod length. Equations are developed relating the amount of rod loss to the quantities characterizing the impact configuration, e.g., impact velocity, material density, target thickness.

UNCLASSIFIED